Proposal for a B-Physics Experiment at TEV I
The μBCD

(October 8, 1990)

H. Castro, B. Gomez, F. Rivera, J.-C. Sanabria, *Universidad de los Andes*
J.F. Arens, G. Jernigan, *U.C. Berkeley, Space Sciences Lab*
P. Yager, *U.C. Davis*
J.M. Butler, L.A. Garren, S. Kwan, P. Lebrun, J. Morfin, T. Nash, L. Stutte, *Fermilab*
P. Avery, J. Yelton, *U. Florida*
M. Adams, D. McLeod, C. Halliwell, *U. Illinois, Chicago*
R. Burnstein, H. Cease, H. Rubin, *Illinois Institute of Technology*
E.R. McCliment, Y. Onel, *U. Iowa*
D. London, *U. Montreal*
M.S. Alam, A. Deogirikar, W. Gibson, *S.U.N.Y. Albany*
C.L. Britton, K. Castleberry, C. Nowlin, C. Sohns, *Oak Ridge National Lab*
P. Gutierrez, G.R. Kalbfleisch, D.H. Kaplan, P. Skubic, J. Snow, *U. Oklahoma*
L.D. Gladney, N.S. Lockyer,[1] R. Van Berg, *U. Pennsylvania*
D.J. Judd, D.E. Wagoner, K. Paick, L. Turnbull, *Prairie View A&M U.*
J.G. Heinrich, C. Lu, K.T. McDonald, *Princeton U.*
A.M. Lopez, J.C. Palathingal, A. Mendez, J. Millan, R. Palomera-Garcia, *Universidad de Puerto Rico*
B. Hoeneisen, C. Marin, C. Jimenez, *Universidad San Francisco de Quito*
M. Sheaff, *U. Wisconsin*
A.J. Slaughter, E. Wolin, *Yale University*

[1] Spokesperson

Executive Summary

B-physics has been shown to be an exciting component of the Tevatron collider program by the recent success of CDF in reconstructing the decays $B \rightarrow J/\psi K^+$ and $J/\psi K^{*0}$. This will lead to measurements by CDF of decay modes and lifetimes of all four b-quark mesons, B_u, B_d, B_s, and B_c, as well as of b-baryons, and to studies of the low-x gluon distribution of the proton via the differential B-production cross section. Also accessible at the Tevatron is the important topic of B_s mixing, which previews the challenge of CP violation. Optimum pursuit of this physics requires an emphasis on particle identification and high-rate data acquisition that is not part of the present collider program.

We propose that B_s mixing be the physics goal of a new program at the TEV I, with options for upgrades to the sensitivity needed for CP violation.

The R&D program of T-784 would be extended to include a demonstration experiment at C0 with detector elements that could be inserted inside the CTC of CDF, inside D0, or later augmented into a new, full-scale B-physics experiment. Our cost estimate for this is \$9M.

The demonstration experiment in 1995 would involve vertexing, tracking, hadron ID, and high-rate data acquisition, but would operate at a luminosity of 2.5×10^{28} cm^{-2}sec^{-1} with no trigger (equivalent to an e^+e^- collider at 10^{33} luminosity). No new civil construction is required. Measurement of B_s mixing with this detector will require luminosity of order 10^{31} cm^{-2}sec^{-1}.

The Phase-I R&D program is a continuation of the work already started via T-784, but includes two important additions. Before informed decisions can be made among the several suggestions for second-generation vertex detectors, significant Laboratory involvement is required in the R&D effort. We therefore propose that the Laboratory, in conjunction with the proponents of this experiment and other interested parties, form a silicon-vertex-detector development group with sufficient resources to explore a wide range of technical issues in a unified manner.

We also propose to add a program of R&D into particle identification to the existing T-784 program of vertexing, tracking, and data acquisition. The immediate emphasis will be on fast, compact RICH counters, that would permit B_s mixing to be explored at the Tevatron. Precision time-of-flight counters, and thin-sampling TRD's will also be developed.

Contents

List of Tables

List of Figures

1 Introduction

Several developments during the 1980's indicate that B-meson physics will be a rich topic for study at Fermilab in the 1990's:

- The B-meson lifetime was first measured by the MAC[1] and Mark II[2] groups to be 1.2 picoseconds, which is longer than that for D mesons. Thus with the use of a silicon vertex detector, perfected during the early 1980's, charged secondaries from B-meson decay can be isolated from the primary interaction vertex. This will permit B physics to be done at a hadron collider, but with the important restriction that complete reconstruction will typically be possible only for all-charged decay modes.

- The cross section for $b\bar{b}$ pairs in hadron-hadron interactions is enhanced by order-α_S^3 QCD corrections[3] and is approximately 50 μbarn at the Tevatron. This is nearly 10^5 times larger than the cross section for $b\bar{b}$ production for an e^+e^- collider operating at the $\Upsilon(4s)$ resonance.

- The B_d^0-$\bar{B}_d^0$ mixing parameter, $x_d = \Delta M/\Gamma$, has been measured at Argus[4] (and subsequently at CLEO[5]) to be about 0.7. This demonstrates that the neutral B-meson system, like the neutral Kaon system, is rich in quantum-mechanical phenomena.

- It is expected that CP violation in the decays of neutral B mesons to CP eigenstates will have an especially clean interpretation. Such decays, when dominated by a single weak amplitude, exhibit CP violation via interference due to mixing, which results in an effect directly dependent on a phase of a CKM-matrix element without strong-interaction ambiguities. However, it is probable that discovery of this type of CP violation will require a sample of 10^8 reconstructible B decays. Samples of this size are within reach of experiments at the Tevatron, if sufficient emphasis is given to the particular challenges of B-physics.

To exploit this opportunity the present BCD collaboration was formed following two Letters of Intent in 1987 for dedicated B-physics experiments at the Tevatron Collider.[6, 7] During the 1987 Beauty Workshop at Fermilab the scenario emerged that an optimal detector for TEV I (that is also appropriate for the SSC) would be based around a central dipole magnet augmented by forward detector arms.[8] This plan was enlarged upon in 1988 in another Letter on Intent.[9] To begin work on several of the critical technologies for such an experiment an R&D Proposal was made to Fermilab in early 1989,[10] and approved as T-784. See the Appendices for the status of this effort. Members of the BCD collaboration are also involved in several Generic and Subsystem R&D projects sponsored by the SSC Laboratory.[11, 12, 13, 14, 15, 16, 17, 18, 19, 20]

A long-range vision of B-physics was presented to the SSC in May 1990 as an Expression of Interest.[21, 22] Action on this is deferred while the needed technical, personnel, and financial resources mature, returning the focus of B-physics in the 1990's to Fermilab. Here the prospects for a dedicated B-physics experiment at the TEV Collider are also not immediate, so we performed a survey of options within the existing and upgraded collider programs.[23]

The Bottom Collider Detector (BCD) as proposed to the SSC[21] is a large, dedicated experiment for B physics that is well suited both to the more forward kinematics of the SSC and, in a reduced configuration, to the TEV I. A fairly detailed cost estimate for Fermilab configurations[22] indicates a price of $\sim$ \$150M for a detector with full coverage. We have also explored a 'mini-BCD' that is based on a dipole analysis magnet like the full BCD, but cannot be upgraded into the latter.[23] The cost for the mini-BCD is perhaps \$40-50M if both forward arms were instrumented.

In reviewing options that are more compatible with the existing Fermilab collider program we believe that both CDF and D0 could be made into rather good B-physics detectors. These collaborations have a strong interest in improving their capability for B physics but do not yet have the internal consensus needed to give this significant priority relative to top-quark searches.

We propose to extend the R&D program of T-784 to include a demonstration experiment at C0 with detector elements that could be inserted inside the CTC of CDF, inside D0, or later augmented into a new, full-scale B-physics experiment. A sketch of this 'μBCD' is shown in Fig. 1.

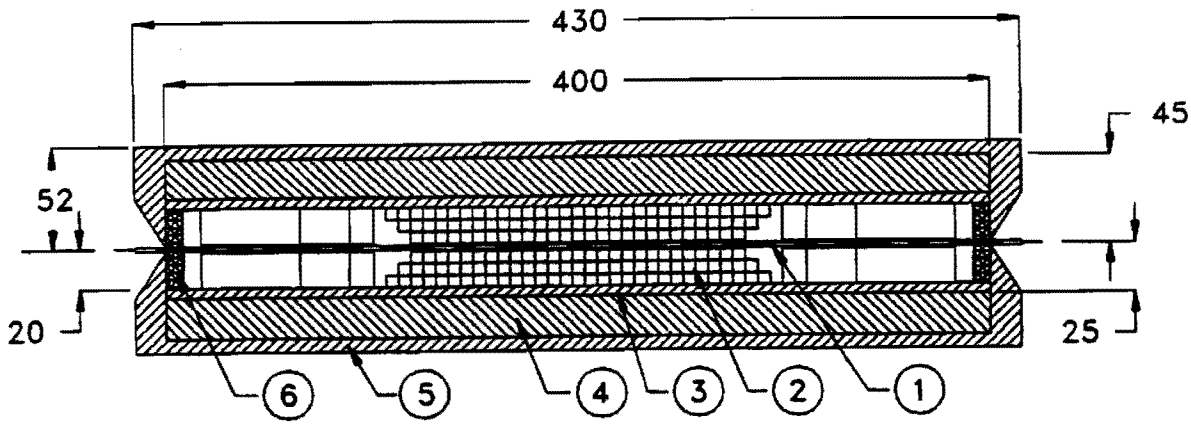

Figure 1: View of the μBCD for C0. **1**: 1-cm-radius 400-μm-thick Be beam pipe, **2**: silicon vertex detector/tracker, **3**: low-pressure RICH counter with solid photocathode, **4**: 1.5-Tesla conventional solenoid magnet coil, **5**: 10-ton iron flux return, **6**: luminosity monitor. All dimensions are in centimeters.

We propose to accomplish this goal via a three-phase program. Personnel and funding realities are such that a strong university commitment (*i.e.*, without distractions in unrelated experiments) to such a long-term goal cannot be maintained without intermediate steps that produce physics. We also believe that this goal cannot be achieved without strong Fermilab commitment and leadership. The steps proposed below are, we believe, a viable path for both university and Fermilab groups to realize one of the most scientifically important opportunities at the Tevatron.

- **Phase I**: Continue and extend the T-784 R&D program (1991-1992).

  1. Vertex Detector.
     - Mechanical issues:
       Complete present studies of assembly, stability, and cooling.
       Form a collider vertex detector development group at Fermilab.
       Initiate a second-generation mechanical model.
       Initiate ANSYS mechanical-engineering analysis
       Prepare a partially instrumented detector for beam tests in 1993.
     - Continue development of the BVX VLSI readout chip.
     - Continue detailed simulation of vertex detector performance.
  2. Particle Identification: RICH Counters, Time of Flight, and TRD's.
     - Prototype of a low-pressure RICH counter for beam tests in 1991.
     - 1-m^2 RICH detector for beam tests in 1993.
     - Continue bench tests, initiate beam tests of precision time-of-flight counters.
     - Begin development of thin-sampling TRD modules for beam tests in 1992.
  3. Extend simulations to combine tracking and particle identification.

- **Phase II**: Interim experiments (1993-1997, \$9M-\$25M).

  1. μBCD, a demonstration experiment in C0 (\$9M).
     - Collider run in 1995 with 2.5×10^{28} $cm^{-2}sec^{-1}$ luminosity.
     - B-production rate equivalent to an e^+e^- collider at 10^{33} $cm^{-2}sec^{-1}$.
     - No trigger, but high-speed data-acquisition system to write > 1000 events/sec.
     - Full-acceptance vertex detector
     - Thin RICH counter with liquid radiator.
     - Conventional solenoid field
  2. Extended μBCD with tracking, lepton identification, and full luminosity (\$14M).
  3. Alternatively, μBCD could be incorporated into CDF or D0.

- **Phase III**: Dedicated, optimized B-physics experiment (1998 on, \$150M)

The Phase-I R&D program is a continuation of the work already started via T-784, but includes two important additions. Before informed decisions can be made among the several suggestions for second-generation vertex detectors, significant Laboratory involvement is required in the R&D effort. We therefore propose that the Laboratory, in conjunction with the proponents of this experiment and other interested parties, form a silicon-vertex-detector development group with sufficient resources to explore a wide range of technical issues in a unified manner.

We also propose to add a program of R&D into particle identification to the existing T-784 program of vertexing, tracking, and data acquisition. The immediate emphasis will be on fast, compact RICH counters, that would permit B_s mixing to be explored at the Tevatron. Precision time-of-flight counters, and thin-sampling TRD's will also be developed.

2 B Physics at the Tevatron Collider

2.1 Physics Goals

The physics goals of a B-physics program at a hadron collider are fourfold:[24]

- **Investigate the production and decay of B_u, B_d, B_s, and B_c mesons as well as b-baryons via full reconstruction of all-charged final states.**

  The recent success of CDF in detecting $B^+ \to J/\psi K^+$ and $B_d^0 \to J/\psi K^{*0}$ demonstrates the accessibility of this physics. First evidence for the B_s and B_c mesons should emerge from the next run of CDF, along with measurements of b-hadron lifetimes, differential production cross sections, and the gluon structure function at low Feynman x. However, the dominant b-quark decay chain is $b \to c \to s$ leading to Kaons in the final state; hence π/K identification is essential for a broad study of b-hadrons.

- **Study B_d and B_s mixing.**

  For this the particle/antiparticle character of the B must be known both at production and decay, as well as a measurement of the proper time of the B when it decays. Good accuracy in the proper time requires a full reconstruction of the B, while particle/antiparticle tagging requires that both B's in the event be observed in 'self-tagging' decays modes. In particular, the readily detected modes involving J/ψ's such as $B_d \to J/\psi K_S^0$ and $B_s \to J/\psi\phi$ are not useful in this context (although $B_d \to J/\psi K^{*0}$ will be).

  B_s mixing is accessible at TEV I, but requires an emphasis on 3-dimensional vertex reconstruction, hadron identification, and high-rate data acquisition that is not part of the present collider program.

- **Search for CP violation in self-tagging modes.**

  CP violation in modes such as $B_d \to D^-\pi+$ or $K^+\pi^-$ could be detected by measurement of an asymmetry in the B and $\bar{B}$ decay rates without need for tagging the second B in the event. Recent theoretical estimates of the size of such a CP-violating asymmetry are, however, somewhat small.

- **Search for CP violation in the decays of neutral B mesons to CP eigenstates.**

  The interpretation of such a signal of CP violation is free from strong-interaction corrections to a first approximation, and permits a direct measurement of phase angles of CKM-matrix elements. Prominent signals of CP violation in the mass matrix as well as in the decay amplitude are expected. In this sense the B-meson system is a much cleaner laboratory for the study of CP violation that is the K-meson system.

  The decay $B_d \to J/\psi K_S^0$ is likely the optimal mode in which to observe CP violation. Independent information could be extracted from the decays $B_d \to \pi^+\pi^-$ and $B_s \to \rho K_S^0$. Tagging of the other B in the event is required.

  Only in rather optimistic scenarios is CP violation accessible at TEV I, and it is unlikely to be observed in experiments that give major priority to top-quark physics.

2.2 Detector Requirements

The general requirements of a detector for B physics at TEV I are:

- **Angular coverage for charged particles extending out to** $|\eta| \sim 4$, where $\eta = -\ln\tan\theta/2$ is the pseudorapidity. The relevant transverse momenta of the decay products are less than 5 Gev/$c \sim M_B$. This is illustrated in Fig. 2 which show the η and P_t spectra for B-decay products according to an ISAJET simulation.

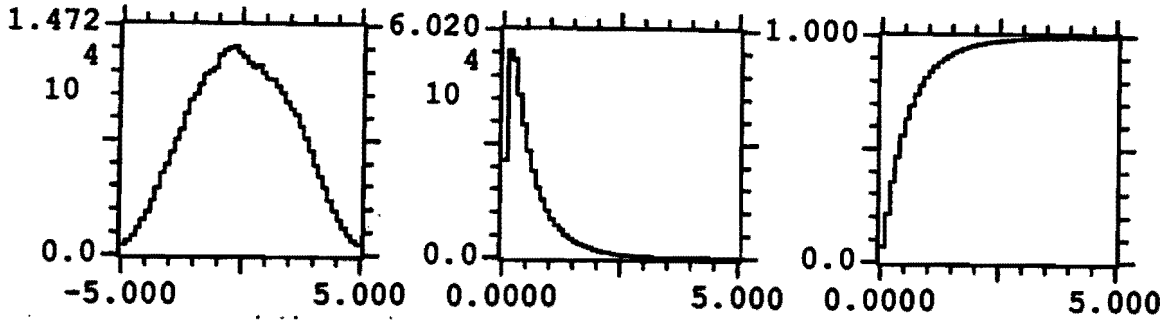

Figure 2: a) the distribution in pseudorapidity η of charged decay products from a large class of B decays, according to an ISAJET simulation of $\bar{p}p$ collisions at $\sqrt{s} = 1800$ GeV. b) the transverse-momentum spectrum of the B-decay products. c) the integrated transverse-momentum spectrum.

- **A silicon vertex detector.** This must locate the secondary vertex of the B's ($c\tau \approx 360\ \mu$m) to isolate the B-decay products from the high-multiplicity primary event. The broad range of angles of the B-decay products leads to the need for a complicated configuration of the vertex detector. If we only desired to observe tracks at small angles to the beams we would use an array of 'disks' as sketched in Fig. 3a, while for large angles a 'barrel' array (Fig. 3b) would be ideal. However, we cannot build a large-solid-angle vertex detector out of separate disk and barrel modules for two reasons:

  1. The finite length of the luminous region blurs the correlation between a silicon detector's position and its angle from the primary vertex, as shown in Fig. 4. Hence the barrel detectors must extend over a length roughly that of the luminous region.
  2. The vertex resolution of both disk and barrel detectors is determined by the radius at which the first measurement is made, as discussed in the following paragraph. (This result contrasts with the use of the detectors for momentum measurement, where the total path length observed is the critical parameter.) Hence the disk

detectors cannot be backed off to make room for the enlarged barrel detector without sacrificing vertex resolution.

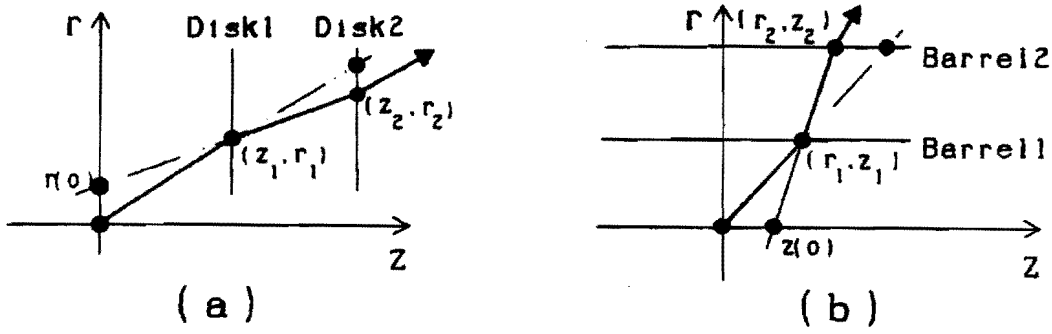

Figure 3: **a)** A simple vertex detector consisting of two 'disk' detectors. The measurement of coordinate r_2 in the second detector is subject to an uncertainty caused by multiple scattering in the first detector. Both detectors have the same intrinsic measurement uncertainty. The intercept at $z = 0$ of the straight-line fit from the two data points is a measure of how well the track fits to the primary vertex. **b)** A vertex detector consisting of two 'barrel' detectors.

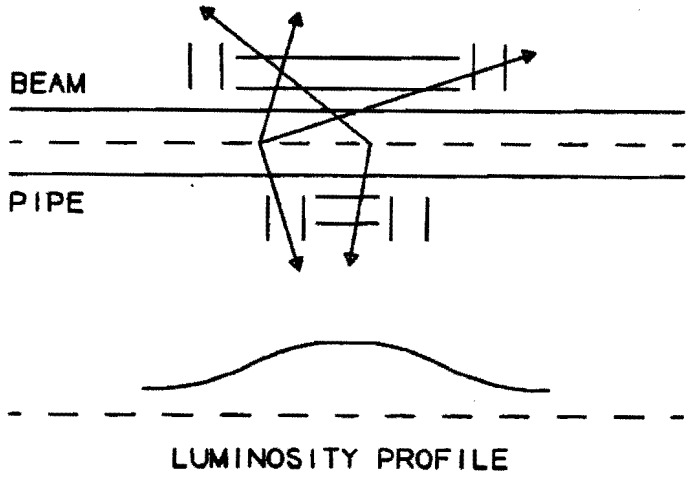

Figure 4: A vertex detector with separate disk and barrel silicon does not give optimal angular coverage if the luminous region has a finite extent.

We illustrate the claim in the preceding paragraph with a simplified calculation of vertex resolution. Suppose the vertex detector consists of only two disks, at z_1 and z_2. From measurements of coordinates r_1 and r_2 we extrapolate a straight-line fit

back to $z = 0$ and use $r(0)$ as the measure of fit to the primary vertex. Each of r_1 and r_2 are subject to a measurement uncertainty σ_{meas}, and r_2 is subject to an additional uncertainty due to the multiple scattering caused by detector 1. Since $r_2 = r_1 + (z_2 - z_1)\tan\theta$, the effect of multiple scattering is

$$\sigma_{\text{M.S.}} = \frac{(z_2 - z_1)\sigma_\theta}{\cos^2\theta} \approx \frac{(z_2 - z_1)0.015\sqrt{T}}{P[\text{GeV}/c]\cos^{5/2}\theta} \approx 10[\mu\text{m}]\frac{(z_2 - z_1)[\text{cm}]}{P[\text{GeV}/c]\cos^{5/2}\theta},$$

for a silicon wafer of thickness $T = 300$ μm. The intercept of the straight-line fit is

$$r(0) = \frac{r_1(z_2 - z) + r_2(z - z_1)}{z_2 - z_1},$$

so the uncertainty in this is

$$\sigma_{r(0)} = \frac{\sqrt{z_2^2\sigma_{r_1}^2 + z_1^2\sigma_{r_2}^2}}{z_2 - z_1} = \frac{\sqrt{(z_2^2 + z_1^2)\sigma_{\text{meas}}^2 + z_1^2\sigma_{\text{M.S.}}^2}}{z_2 - z_1}.$$

Now $z_1 = r_1/\tan\theta$, and typically $z_2 = 2z_1$, so we have

$$\sigma_{r(0)} \approx \sqrt{5\sigma_{\text{meas}}^2 + \left(\frac{10[\mu\text{m}]r_1[\text{cm}]}{P_t[\text{GeV}/c]\cos^{3/2}\theta}\right)^2}.$$

We expect σ_{meas} to be about 5-10 μm, so for P_t of order 1 GeV/c we would like r_1 only 1 cm or so. Then we could achieve $\sigma_{r(0)} \approx$ 20-30 μm $\approx c\tau_B/15$.

A very similar argument can be made for vertexing in a barrel detector, in which detector elements at radii r_1 and r_2 measure coordinates z_1 and z_2. The uncertainty in the extrapolated value $z(0)$ has the same form as that just found for $\sigma_{r(0)}$ but with the $\cos^{3/2}\theta$ changed to $\sin^{3/2}\theta$. Hence both disk and barrel detectors must begin at very small radii.

We conclude that it is vital to build a vertex detector with interpenetrating regions of disks and barrels if both large- and small-angle tracks are to be analyzed.

- **Momentum measurement** of charged particles. In collider experiments to date this function has been performed in a separate tracking system using gas-filled chambers. These devices are as large as possible since momentum resolution varies as $1/Bl^2$. To have a more compact detector the silicon vertex detector could also serve as the tracker. With spatial resolution 10-20 times better than a gas tracking system the task of pattern recognition can be performed with fewer layers of silicon detectors.

  We estimate the momentum resolution that could be obtained in a silicon tracking system with the following expression;[28]

$$\left(\frac{\sigma_{P_\perp}}{P_\perp}\right)^2 = \frac{720}{n+5}\left(\frac{\sigma_{x_\perp}P_\perp}{3\times10^{-4}BL^2}\right)^2 + 1.43\left(\frac{0.015}{3\times10^{-4}\beta BL}\right)^2\sum_{i=1}^{n}t_i(1 + (1/9)\log_{10}t_i),$$

where $P_\perp$ is the momentum component perpendicular to the magnetic field (not necessarily to the beam), $\sigma_{x_\perp}$ is the measurement error in cm, B is the magnetic field

strength in kG, L is the path length in cm over which the measurement is made, n is the number of measurements, and t_i is the thickness in radiation lengths of the material associated with measurement i. This expression is strictly valid for the case of uniform sampling along L, which is entirely within field B. The dependence of the momentum resolution on spatial resolution and momentum has the familiar form

$$\left(\frac{\sigma_{P_\perp}}{P_\perp}\right)^2 = (AP_\perp)^2 + B^2.$$

As an example, consider a 5-layer silicon tracker that occupies 18 cm radially inside a 15-kG solenoidal magnetic field, for which $P_\perp = P_t$. We suppose that the resolution of a silicon detector is 7 μm, and that it is 300 μm thick which implies a radiation length of $t_i = 0.003$. Then the momentum-resolution coefficients are $A = 0.4\%/\mathrm{GeV}/c$ and $B = 2.4\%$. Hence the momentum resolution would be multiple-scattering dominated for $P_t < 6$ GeV/c. This example underestimates the effect of multiple scattering in a vertex detector with interpenetrating disks and barrels.

Increasing the magnetic-field strength to 30 kG would reduce the momentum resolution to 1.2%. The consequent mass resolution for B mesons would be $\approx 1\%$ which might not be sufficient to distinguish B_d from B_s mesons. However, we see from Tables 3 and 4 of Ref. [21] that the prominent decay modes of the B_s all have different particle content from the prominent decays of the B_d. If particle identification is available a mass resolution of 1-2% will suffice to identify B_s mesons.

A silicon tracker will require more channels ($\sim$ 3M) than a silicon vertex detector ($\sim$ 1M).

- **Identification of electrons, muons, pions, and Kaons.** Lepton identification is needed for analysis of $B \to J/\psi X$ decays, and for triggering on $B \to l^+l^-$ or lX. Identification of pions and Kaons is needed for reconstruction of B decays involving the dominant decay chain $b \to c \to s$, and for tagging the particle/antiparticle character of the B's via $B \to K^\pm X$. Identification of neutrals is not particularly useful at a hadron collider, as these cannot be associated directly with a secondary vertex. Of course, if muon identification is to be effective, there must be an absorber thick enough to suppress hadron punchthrough.

- **An experimental trigger** including:

  1. **'No trigger'** at all. Since one event in 1000 at TEV I contains a B a large sample of B's can be collected with just a minimum-bias trigger. This trigger is very competitive with an e^+e^- collider where the cross section for B-$\bar{B}$ events is only 1 nb. Thus if 1000 events/sec can be recorded at TEV I, this gives a B sample equivalent to an e^+e^- collider with a luminosity of 10^{33} cm^{-2}sec^{-1}.
  2. A **lepton-pair trigger** for $B \to J/\psi X$. Even at a luminosity of 10^{32} cm^{-2}sec^{-1} there would be only about 10 Hz of such triggers assuming 100% acceptance. Figure 5a shows the transverse-momentum spectrum of the lepton with the lower P_t from $B \to J/\psi \to l^+l^-$; Fig. 5c shows that for the lepton with the higher P_t .

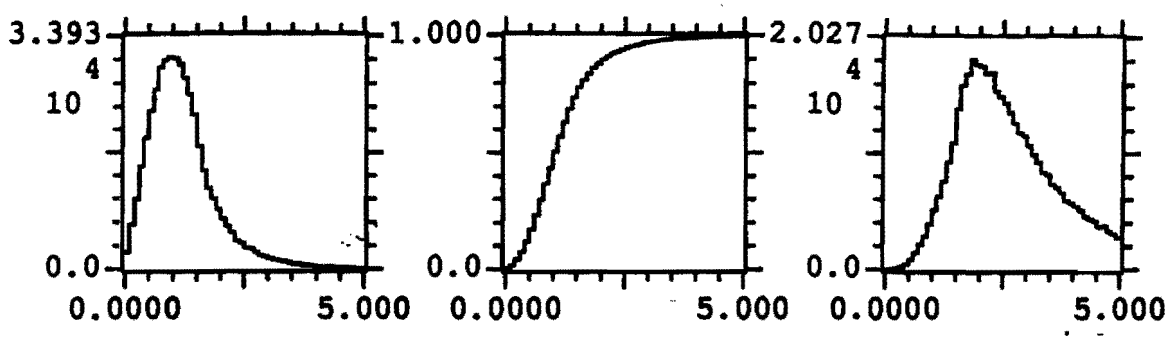

Figure 5: a) The P_t spectrum for the lower-P_t lepton from $B \to J/\psi \to l^+l^-$. b) The integral spectrum of a). c) The P_t spectrum for the higher-P_t lepton.

About 50% of all $B \to J/\psi X$ decays have one lepton with transverse momentum less than 1 GeV/c.

3. **Single-lepton triggers.** To provide a large data sample the lepton trigger must extend to very low-transverse momentum. Figure 6a and b shows the transverse-momentum spectrum for 'primary' leptons from $B \to l^{\pm}X$. For 50% acceptance we would need to trigger on $P_t > 1$ GeV/c. There are significant backgrounds in both the electron and muon triggers at such low P_t .

   Figures 6c and d show the P_t spectra for 'secondary' leptons from $B \to DX$ with $D \to l^{\pm}Y$. The secondary leptons from B decay outnumber the primary leptons by 1.6:1, but have a softer P_t spectrum.

4. A **secondary-vertex trigger.** Such a trigger could enrich the sample of B events with little loss of efficiency. The performance of this trigger is rather speculative at present. Our simulation[45] of vertex finding in a magnetic field indicates that a momentum measurement is needed for an efficient vertex algorithm for tracks with multiple scattering. This adds to the complexity of an online vertex trigger.

A very productive B-physics program can begin with triggers 1 and 2, while collecting data with which to explore triggers 3 and 4.

- **A high-rate data-acquisition system.** This is essential for any physics other than $B \to J/\psi X$ with a lepton-pair trigger. By high rate we mean a system that can process of order 10^5 events/sec in an online software trigger processor, and record $\sim$ 1000 events/sec to tape. In practice the online computing power can be added incrementally, but the ability to move large amounts of data off the detector into a processor farm must be provided for *ab initio*.

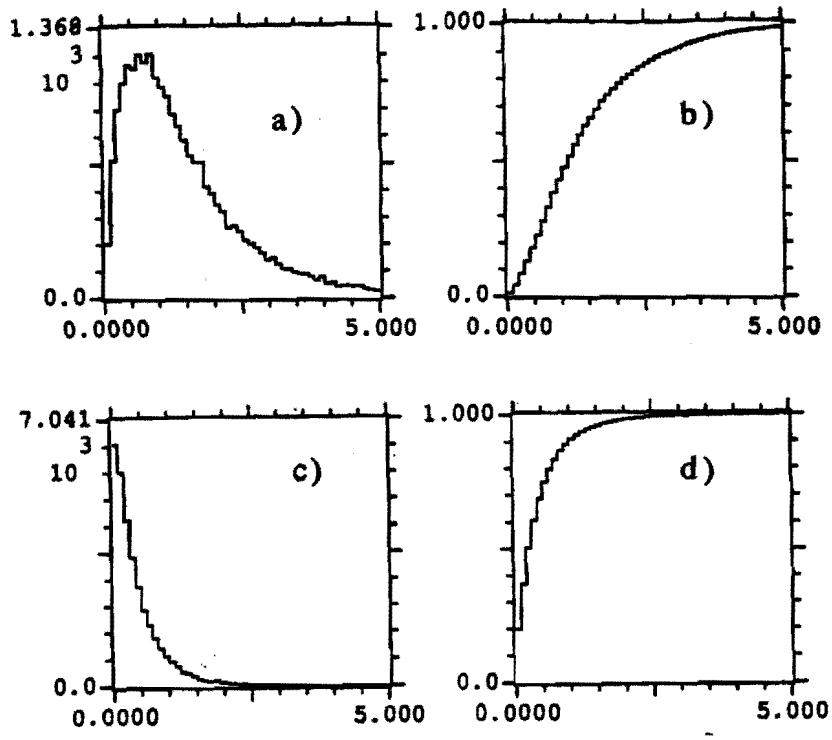

Figure 6: a) The P_t spectrum for single leptons from $B \rightarrow l^{\pm}X$. b) The integral spectrum of a). c) The P_t spectrum for leptons from $B \rightarrow DX$ with $D \rightarrow l^{\pm}Y$. d) The integral spectrum of c).

3 The μBCD

The goals and detector requirements for a B-physics program, outlined in the previous section, lead to a design for an experiment with maximal capability that we call the Bottom Collider Detector (BCD).[21] Figure 7 shows a quarter section of a configuration that includes a Forward arm suitable for the SSC. At Fermilab there is the opportunity to begin work now on an experimental configuration that is considerably less ambitious than the full BCD, but allows us to explore the major technical issues while performing significant new B-physics measurements. We therefore propose to extend the R&D program of T-784 to include a configuration of vertexing, tracking, and particle identification that could be tested in a physics run at C0 before being integrated with CDF or D0, or being expanded into a standalone experiment that we call μBCD.

The initial form of the μBCD has been shown in Fig. 1, and consists of:

1. **A silicon tracker/vertex detector** consisting of four barrel layers of silicon strip detectors in the central region along with interpenetrating disk detectors that continue into the forward regions. The outer radius is 20 cm and the total length is 330 cm, which permits tracking over the full radial extent of the detector for $|\eta| < 2.8$. To cover such a large pseudorapidity range in a solenoidal geometry, the silicon detector

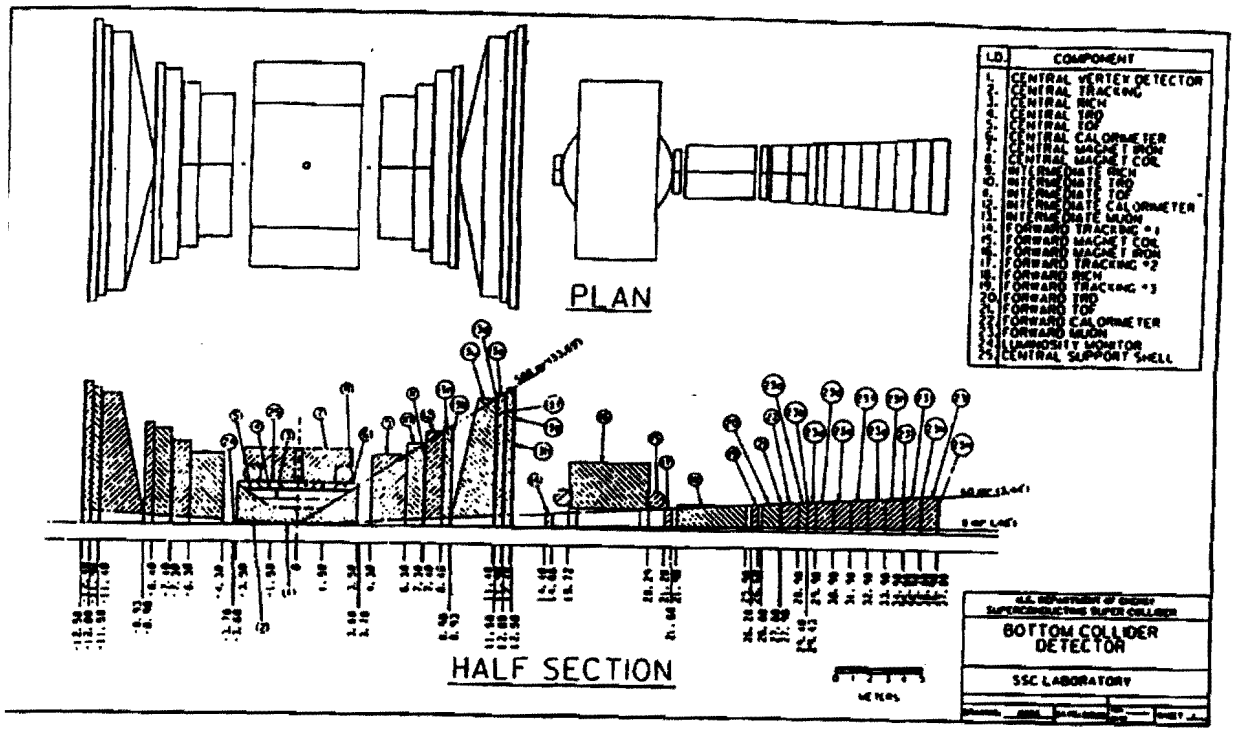

Figure 7: Plan and section views of the BCD as proposed for the SSC.[21] Central Detector: **1**: silicon vertex detector, **2**: straw-tube tracking system, **3**: RICH counter, **4**: transition radiation detector, **5**: time-of-flight system, **6**: electromagnetic calorimeter, **7**: magnet yoke, **8**: superconducting coil. Intermediate Detector: **9**: RICH counter, **10**: TRD, **11**: time-of-flight, **12** E-M calorimeter, **13**: Muon system. Forward Detector: **14, 17, 19**: tracking, **15**: superconducting coil, **16**: magnet yoke, **18**: RICH counter, **20**: TRD, **21**: time-of-flight, **22**: E-M calorimeter, **23** muon system, **24**: luminosity monitor, **25**: central support shell.

must perform the function of tracking as well as vertex finding. There are 1.5-2M strips which will be read out via 12,000 of the 128-channel BVX VLSI chips now under development at Fermilab.

2. A **ring-imaging-Čerenkov (RICH) counter** operating at low pressure with a solid photo-cathode.[26] This would have a 5-mm-thick liquid C_8F_{14} radiator at 21-cm radius, and 4-cm drift path to a mirror at 25-cm radius which reflects the Čerenkov photons back to the photodetector at 20-cm radius just inside the radiator. There will be 200k channels of 5 mm × 5 mm pads read out in 1,600 groups of 128 by the same BVX chip as used in the vertex detector. π/K separation could be achieved over the momentum range $0.3 < P < 4$ GeV/c.

3. A **conventional solenoid magnet** 25 cm in radius, 20 cm thick, and 5 m long with field of 15 kG. The flux return would weigh only 10 tons and would fit between the

Main Ring beampipe and that of the Tevatron.

4. A **high-speed data-acquisition system** based on the barrel-switch event builder now under development at Fermilab. The initial version would be able to take 10^4 events/sec off the detector.

5. An **online processor farm** for software triggering. The system would be able to record 1000 events/sec to tape.

The μBCD would operate initially with a luminosity of only 2.5×10^{28} cm^{-2}sec^{-1}, corresponding to 1000 interactions/sec. All of these would be written to tape, yielding 1 B-$\bar{B}$ event/sec. In a run of 100 days some 10^7 B-$\bar{B}$ events would be recorded. Supposing the reconstruction efficiency is as low as 1% we would have 10 reconstructed events in any B-decay mode with a branching fraction of 10^{-4}.

Extensive exploration of trigger schemes would be made. If a trigger rejection of 10 could be obtained in a future prompt trigger, and an additional factor of 10 obtained in software triggers, then the experiment could operate at a luminosity of 10^{30} cm^{-2}sec^{-1} to obtain 1000 reconstructed events per mode of 10^{-4} branch. This would be sufficient to study B_s mixing, which is the next major milestone in B physics. Such success would point the way toward the techniques needed to observe CP violation.

The μBCD could be upgraded in two stages by the addition of electron, and muon detection. Figure 8 shows a configuration in which the conventional solenoid magnet has been replace by a superconducting coil capable of 3-Tesla field, and the magnet is surrounded by an electromagnetic calorimeter. This would have $\sim$ 8000 towers each with three longitudinal samples.

Figure 9 shows the possible addition of a muon detector, consisting of a steel absorber about 2.2-m thick to range out muons of less than 3 GeV energy. The steel would weigh about 1500 tons. The penetrating muons would be identified in Iarocci-tube detectors.

A cost estimate for the μBCD is

Silicon vertex detector	\$5M
RICH counter	\$2M
Conventional solenoid magnet	\$0.5M
Event-builder switch for 10^4 events/sec	\$0.5M
Online processor farm and tape drives for $\mathcal{L} = 10^{29}$ cm^{-2}sec^{-1}	\$1M
Total for Stage 1 μBCD	**\$9M**

The upgrades might cost

Superconducting solenoid magnet	\$2M
E-M calorimeter	\$3M
Muon steel and detector	\$2M
Event-builder switch for 10^5 events/sec	\$2M
Online processor farm for $\mathcal{L} = 10^{32}$ cm^{-2}sec^{-1}	\$5M
Additional for Stage 2 μBCD	**\$14M**

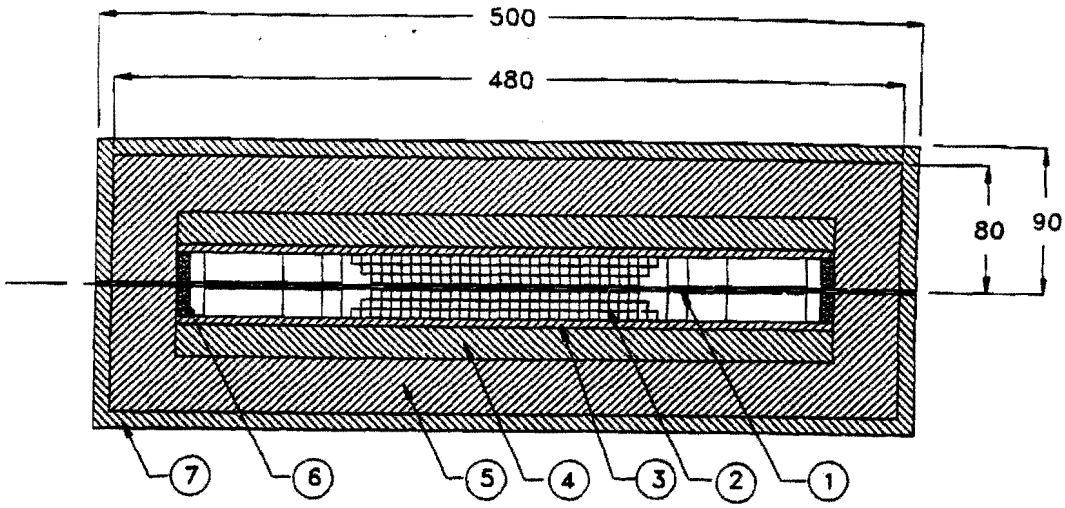

Figure 8: View of an upgraded μBCD with an electromagnetic calorimeter. 1: beampipe, 2: silicon vertex detector, 3: RICH counter, 4: 3-T superconducting solenoid magnet, 5: E-M calorimeter, 6: luminosity monitor 7: 26-ton flux return.

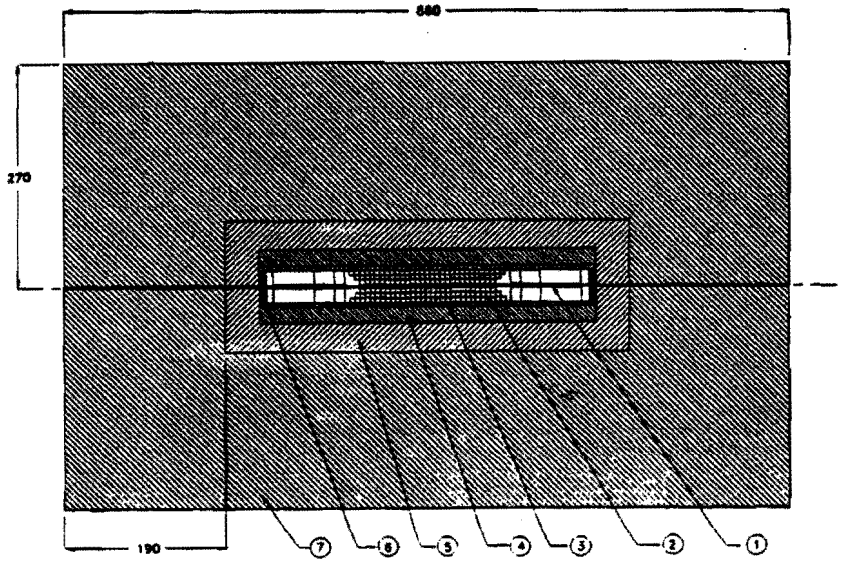

Figure 9: View of an upgraded μBCD with the addition of a muon detector. 1: beampipe, 2: silicon vertex detector, 3: RICH counter, 4: 3-T superconducting solenoid magnet, 5: E-M calorimeter, 6: luminosity monitor, 7: 1500-ton muon detector/flux return.

3.1 Rate Estimates

We now estimate how many B decays into various modes might be reconstructed in one year of high-luminosity running at the TEV I. The following cuts are applied to the B-decay products:

1. $P_t > 0.3$ GeV/c for pions and Kaons.
2. $P < 4$ for Kaons, to permit identification in the RICH counter.
3. $P_t > 1$ GeV/c for electrons.
4. $P > 3$ GeV/c for muons, so they penetrate the muon steel.

The geometric acceptance for several B decays to all-charged final states has been estimated using an ISAJET/GEANT simulation subject to these cuts. The results are in Table 1.

We need three further ingredients for the rate estimates. First, we suppose that a $b\bar{b}$ pair materializes only into mesons, and in the ratios

$$B_u : B_d : B_s = \frac{1-\epsilon}{2} : \frac{1-\epsilon}{2} : \epsilon.$$

We estimate that $\epsilon = 0.25$, and hence

$$B_u : B_d : B_s = 0.375 : 0.375 : 0.25.$$

We also need an estimate of the efficiency of the tracking and vertexing of the B decay, which we take to be 0.33. This is a plausible upper limit as found in simulations described in the BCD Reply to the SSC PAC.[22]

Finally, we need estimates of the branching ratios of the B's to the modes of interest, as well as for the secondary decays. We take branching ratios for B decay from the model calculations of Bauer, Stech, and Wirbel.[27] That paper does not directly predict branching ratios for the B_s. In the spectator model we expect that B.R.$(B_s \to D_s^- \pi^+)$ = B.R.$(B_d \to D^- \pi^+)$, B.R.$(B_s \to \rho^0 K_S^0)$ = B.R.$(B_d \to \rho^0 \pi^0)$, and B.R.$(B_s \to K^+ K^-)$ = B.R.$(B_d \to K^- \pi^-) \approx \lambda^2$B.R.$(B_d \to \pi^+ \pi^-)$, which leads to the values in Table 1. According to Ref. [27], B.R.$(B_s \to \rho^0 K_S^0)$ will be suppressed by strong-interaction effects and will be comparable to that for $B_s \to K^+ K^-$, although the latter is doubly-CKM-suppressed. For $B_s \to K^- K^-$ we are ignoring the possibility of an important contribution from penguin graphs.

The secondary decays that occur in the modes listed in Table 1 are:

Decay Mode	Branching Ratio
$K_S^0 \to \pi^+\pi^-$	0.69
$\rho^0 \to \pi^+\pi^-$	1.00
$K^{*0} \to K^+\pi^-$	0.67
$\phi \to K^+K^-$	0.50
$D^+ \to K^-\pi^+\pi^+$	0.08
$D^0 \to K^-\pi^+$	0.04
$D_s^+ \to \phi\pi^+$	0.03
$D_s^+ \to \phi\pi^+\pi^+\pi^-$	0.04
$J/\psi \to e^+e^-$	0.07

A sample rate calculation follows:

- Luminosity ..... 5×10^{31} cm^{-2}sec^{-1}
- Standard running year of 10^7 sec $\Rightarrow$ ..... 500 pb^{-1}
- $\sigma_{b\bar{b}} = 40$ μb $\Rightarrow$ ..... 2×10^{10} B-$\bar{B}$ pairs
- 3/4 $B^{\pm}$ per B-$\bar{B}$ pair $\Rightarrow$ ..... 1.5×10^{10} $B^{\pm}$
  3/4 B_d^0 or $\bar{B}_d^0$ per B-$\bar{B}$ pair $\Rightarrow$ ..... 1.5×10^{10} B_d^0
  1/2 B_s^0 or $\bar{B}_s^0$ per B-$\bar{B}$ pair $\Rightarrow$ ..... 10^{10} B_s^0
- B.R. for $B^+ \to \bar{D}^0\pi^+$; $\bar{D}^0 \to K^+\pi^-$: $(0.004)(0.04) = 1.6 \times 10^{-4}$
  $\Rightarrow$ ..... 2.4×10^6 $B^+ \to K^+\pi^-\pi^+$
- Geometric acceptance ($\epsilon_{\rm geom}$ in Table 1) = 0.39;
  Vertexing and tracking efficiency = 0.33;
  $\Rightarrow$ Overall efficiency = 0.13 $\Rightarrow$ ..... 310,000 reconstructed $B^+ \to K^+\pi^-\pi^+$

In a test run of Stage-1 μBCD of 100 days at a luminosity of 2.5×10^{28} cm^{-2}sec^{-1}the rates would be 20,000 times smaller. However, at this low luminosity we could trigger on every event, so the rates listed in the Table could be achieved.

In studies of B_s mixing or CP violation we must have a tag as to the particle/antiparticle character of the second B in the event. We consider three tags:

1. The **Kaon tag** based on the sign of the Kaon from the cascade decay $b \to c \to s$. About 60 % of all B decays include a charged Kaon, although of these some 30% have the 'wrong' sign and could lead to a mistag. See section 4.1 of the BCD Reply to the SSC PAC.

2. The **muon tag** based on the sign of the muon from decays $B \to \mu X$ (10% branching fraction) of the second B. The muon must, of course, satisfy the 3-GeV range cut.

3. The **electron tag** based on the sign of the electron from decays $B \to eX$ (10% branching fraction) of the second B. The efficiency of the electron tag is a rapid function of the minimum-P_t cut for electrons, as can be seen from Figs. 6a and b.

In the tags considered here, one other charged particle from the second B besides the tagging particle must be reconstructed. The geometric acceptances for such tagging decays have been estimated using the decay $B_d \to D^{*-}l^+\nu$ with $D^{*-} \to \bar{D}^0\pi^-$ and $\bar{D}^0 \to K^+\pi^-$. See Table 2.

We see that the acceptance for the muon tag equals that for the electron tag with a minimum-transverse-momentum cut of 1.6 GeV/c on the electron.

As discussed above, the lepton tags could be the basis for triggers for the experiment. However, the Kaon tag is not itself a trigger. Only if a general trigger such as a secondary-vertex requirement becomes available can the Kaon tag be used for modes other than $B \to J/\psi X$.

Table 3 estimates the rates of tagged and reconstructed events for the modes presented above in Table 1. For the modes $B \to J/\psi X$ we can use the lepton-pair trigger on this B and use any or all tags on the second B. In this case the Kaon tag will yield the largest

Table 1: Rate estimates for reconstructed B decays in the μBCD at TEV I, assuming 100% trigger efficiency. The geometric acceptance $\epsilon_{\rm geom}$ has been estimated with an ISAJET/GEANT simulation. B.R.(B) is the branching ratio for the two-body B decay, estimated according to Bauer *et al.*[27] B.R.(Tot) is the product of B.R.(B) and the secondary branching ratios. The efficiency used is the product of the geometric acceptance and a factor 0.33 for the efficiency of tracking and vertexing. The reconstructed-event samples are for an integrated luminosity of 500 pb^{-1}, collectable in 1 year of running at a luminosity of 5×10^{31} cm^{-2}sec^{-1}. In a test run of 100 days at a luminosity of 2.5×10^{28} cm^{-2}sec^{-1} the rates would be 1/20,000 of those listed.

Decay Mode	All-Charged Daughters	$\epsilon_{\rm geom}$	B.R.(B)	B.R.(Tot)	Recon. Decays
$B^+ \to J/\psi K^+$	$e^+e^-K^+$	0.231	6×10^{-4}	4.2×10^{-5}	48,500
$B^+ \to \bar{D}^0\pi^+$	$K^+\pi^-\pi^+$	0.390	0.004	1.6×10^{-4}	310,000
$B^+ \to D_s^+\bar{D}^0$	$K^+K^-\pi^+K^+\pi^-$	0.246	0.008	4.8×10^{-6}	5,900
$B_d^0 \to J/\psi K_S^0$	$e^+e^-\pi^+\pi^-$	0.206	3×10^{-4}	1.4×10^{-5}	14,400
$B_d^0 \to D^-\pi^+$	$K^+\pi^-\pi^-\pi^+$	0.293	0.006	4.8×10^{-4}	703,000
$B_d^0 \to \pi^+\pi^-$	$\pi^+\pi^-$	0.709	2×10^{-5}	2×10^{-5}	71,000
$B_s^0 \to J/\psi\phi$	$e^+e^-K^+K^-$	0.256	3×10^{-4}	10^{-5}	8,500
$B_s^0 \to D_s^-\pi^+$	$K^+K^-\pi^-\pi^+$	0.380	0.005	1.5×10^{-4}	190,000
$B_s^0 \to D_s^-\pi^+$	$K^+K^-\pi^-\pi^+\pi^-\pi^+$	0.123	0.005	2×10^{-4}	82,000
$B_s^0 \to D_s^-\pi^+\pi^+\pi^-$	$K^+K^-\pi^-\pi^+\pi^-\pi^+\pi^+\pi^-$	0.049	0.01	4×10^{-4}	65,000
$B_s^0 \to \bar{D}^0K^{*0}$	$K^+\pi^-K^+\pi^-$	0.220	0.005	1.3×10^{-4}	95,000
$B_s^0 \to \rho^0K_S^0$	$\pi^+\pi^-\pi^+\pi^-$	0.292	10^{-6}	7×10^{-7}	680
$B_s^0 \to K^+K^-$	K^+K^-	0.080	8×10^{-7}	8×10^{-7}	210

number of tagged events. For other B modes we suppose that the single-lepton trigger must be used, and so present rates only for an associated lepton tag.

The rates in Table 3 are for a run of 500 pb^{-1}. For a test run of 100 days at a luminosity of 2.5×10^{28} cm^{-2}sec^{-1} the rates would be 1/20,000 of those in the Table.

Table 2: Acceptance for the tagging decay $B_d^0 \to D^{*-} e^+ \nu$, estimated with an ISAJET simulation. For each tag, one other charged particle must be accepted besides the tagging particle.

Tag Type	$P_{t,e,\min}$ (GeV/c)	Geometric Acceptance
K	–	0.476
μ	–	0.302
e	1.00	0.467
e	1.25	0.389
e	1.50	0.318
e	1.75	0.258
e	2.00	0.207
e	2.25	0.166
e	2.50	0.134

Table 3: Rate estimates for tagged and reconstructed B decays in the μBCD at TEV I. The combined geometric acceptance for the all-charged decay of the first B and the tagging decay of the second B is listed as $\epsilon_{\rm geom}$. B.R.(Tot) is the product of B.R.(B) as given in Table 1 and the secondary branching ratios. The efficiency used is the product of the geometric acceptance $\epsilon_{\rm geom}$, of a factor $(0.33)^2 = 0.11$ for the combined efficiency of tracking and vertexing of both B's, and of a factor 0.6 for Kaon tags or 0.1 for electron tags corresponding to the fraction of all events for which these tags apply. The reconstructed-event samples are for an integrated luminosity of 500 pb^{-1}, collectable in 1 year of running at a luminosity of 5×10^{31} cm^{-2}sec^{-1}.

Decay Mode	All-Charged Daughters	Tag Type	$\epsilon_{\rm geom}$	B.R.(Tot)	Recon. Decays
$B^+ \to J/\psi K^+$	$e^+e^-K^+$	K	0.133	4.2×10^{-5}	5,600
$B^+ \to J/\psi K^+$	$\mu^+\mu^-K^+$	K	0.037	4.2×10^{-5}	1,500
$B^+ \to \bar{D}^0\pi^+$	$K^+\pi^-\pi^+$	e	0.205	1.6×10^{-4}	5,400
$B^+ \to D_s^+\bar{D}^0$	$K^+K^-\pi^+K^+\pi^-$	e	0.130	4.8×10^{-6}	100
$B_d^0 \to J/\psi K_S^0$	$e^+e^-\pi^+\pi^-$	K	0.113	1.4×10^{-5}	1,600
$B_d^0 \to J/\psi K_S^0$	$\mu^+\mu^-\pi^+\pi^-$	K	0.040	1.4×10^{-5}	600
$B_d^0 \to J/\psi K_S^0$	$e^+e^-\pi^+\pi^-$	e	0.108	1.4×10^{-5}	250
$B_d^0 \to J/\psi K_S^0$	$\mu^+\mu^-\pi^+\pi^-$	e	0.045	1.4×10^{-5}	100
$B_d^0 \to J/\psi K_S^0$	$e^+e^-\pi^+\pi^-$	μ	0.070	1.4×10^{-5}	160
$B_d^0 \to J/\psi K_S^0$	$\mu^+\mu^-\pi^+\pi^-$	μ	0.029	1.4×10^{-5}	70
$B_d^0 \to D^-\pi^+$	$K^+\pi^-\pi^-\pi^-$	e	0.155	4.8×10^{-4}	12,300
$B_d^0 \to \pi^+\pi^-$	$\pi^+\pi^-$	e	0.369	2×10^{-5}	1,200
$B_d^0 \to \pi^+\pi^-$	$\pi^+\pi^-$	μ	0.240	2×10^{-5}	800
$B_s^0 \to J/\psi\phi$	$e^+e^-K^+K^-$	K	0.142	10^{-5}	940
$B_s^0 \to J/\psi\phi$	$\mu+\mu^-K^+K^-$	K	0.037	10^{-5}	250
$B_s^0 \to D_s^-\pi^+$	$K^+K^-\pi^-\pi^+$	e	0.201	1.5×10^{-4}	3,300
$B_s^0 \to D_s^-\pi^+$	$K^+K^-\pi^-\pi^+\pi^-\pi^+$	e	0.068	2×10^{-4}	1,500
$B_s^0 \to D_s^-\pi^+\pi^+\pi^-$	$K^+K^-\pi^-\pi^+\pi^-\pi^+\pi^+\pi^-$	e	0.029	4×10^{-4}	1,300
$B_s^0 \to \bar{D}^0K^{*0}$	$K^+\pi^-K^+\pi^-$	e	0.131	1.3×10^{-4}	1,900
$B_s^0 \to \rho^0K_S^0$	$\pi^+\pi^-\pi^+\pi^-$	e	0.150	7×10^{-7}	12
$B_s^0 \to K^+K^-$	K^+K^-	e	0.042	8×10^{-7}	22

3.2 B_s-$\bar{B}_s$ Mixing

The study of B_s-$\bar{B}_s$ mixing is more accessible than CP violation at the TEV I, but previews many of the challenges of the latter. This is because both phenomena require a tag as to the particle/antiparticle character of the second B in the event to determine the initial state of the fully reconstructed B. We propose that the study of B_s-$\bar{B}_s$ mixing be the major goal of the next generation of B-physics experiments at the TEV I.

Mixing in the neutral B_q-meson system (for $q = d, s$) is characterized by the parameter x_q with $x = \Delta M_{B_q}/\Gamma_{B_q}$. If we start with N B_q-mesons at $t = 0$, at time t we have

$$N_{B_q(\bar{B}_q)} = (N/2)e^{-t}(1 \pm \cos x_q t), \tag{1}$$

where in this section we measure the proper time t in units of the B lifetime (assumed equal for the two mass eigenstates). As noted earlier, B_d mixing has already been observed by ARGUS[4] and CLEO,[5] whose results yield the combined value $x_d = 0.72 \pm 0.10$.

The study of B_s-$\bar{B}_s$ mixing is interesting for several reasons:

1. To measure the CP asymmetry in $B_s \to \rho^0 K^0_S$, the mixing parameter x_s that appears in factor $\sin x_s t$ associated with the CP asymmetry (see Eq. (16) of the following subsection) must be determined accurately.

2. If $x_s \leq 3$ then new physics must be introduced into the Standard Model.

3. A measurement of x_s/x_d gives a better determination of $|V_{td}|$ than a measurement of x_d alone because some of the strong-interaction uncertainty in the interpretation of x_q cancels in the ratio. Note that $|V_{td}|$ is important for overconstraining the unitarity of the CKM matrix since it is one of the sides of the unitarity triangle (see Fig. 11). In this respect it is as important as measuring the internal angles of the unitarity triangle from CP asymmetries.

3.2.1 Theoretical Review

Mixing in the neutral B_q systems arises from the box diagram shown in Fig. 10, which is dominated by the top quark and which is the same for B_d and B_s except for $d \leftrightarrow s$ interchange.

The mixing parameter x_q introduced above can be calculated as[28, 29]

$$x_q = \left(\frac{G_F^2}{6\pi^2} M_W^2 g(m_t^2/M_W^2)\right)\left(\tau_q M_q \eta_q f_q^2 B_{bq} |V_{tq}|^2\right). \tag{2}$$

The first group of factors is independent of the B-meson type, and g is a function of the t-quark mass m_t:

$$\frac{g(y_t)}{y_t} = \frac{1}{4} + \frac{9}{4(1-y_t)} - \frac{3}{2}\frac{1}{(1-y_t)^2} - \frac{3}{2}\frac{y_t^2 \ln y_t}{(1-y_t)^3},$$

where $y_t = m_t^2/M_W^2$. In the second group of factors τ_q and M_q are the lifetime and mass of the B_q mesons, respectively, η_q is the QCD correction to the box diagram (= 0.85 for the B_d

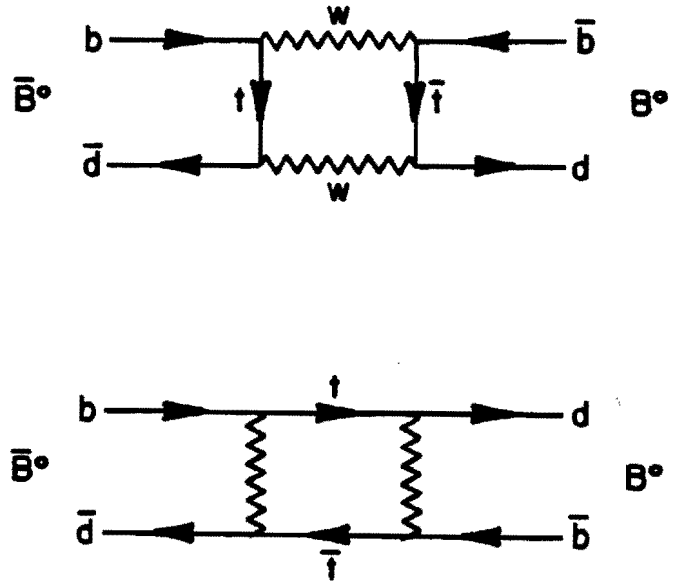

Figure 10: The box diagrams with top-quark exchange that dominate B_q mixing.

system), and $f_q^2 B_{bq}$ is a second strong-interaction correction (f_q is called the pseudoscalar decay constant and B_{bq} is called simply the B parameter). In the Standard Model the mixing diagram is calculated at the quark level, whereas the mixing is experimentally measured via the decays of B mesons. One must include a correction factor $f_q^2 B_{bq}$ that represents the ratio of the observable value for x_q to that calculated using $\bar{b}q$ quarks.

The value of f_q can be calculated via lattice-gauge models, yielding[30]

$$\begin{aligned} f_d &= 0.105 \pm 0.017 \pm 0.030 \text{ GeV}, \\ f_s &= 0.155 \pm 0.031 \pm 0.048 \text{ GeV}, \\ f_s/f_d &= 1.47 \pm 0.07 \pm 0.30. \end{aligned}$$

The factor f_s is expected to be larger than f_d due to the difference in the d and s quark masses. The ratio f_s/f_d is better calculated than either f_d or f_s. The B parameters are also calculated in the lattice-gauge models, and found to be very close to 1.

With the good approximations that $\tau_s \approx \tau_d$, $M_s \approx M_d$, and $\eta_s \approx \eta_d$ we can write

$$\frac{x_s}{x_d} = \left|\frac{V_{ts}}{V_{td}}\right|^2 \frac{f_s^2 B_{bs}}{f_d^2 B_{bd}}.$$

We can use this relation to extract the value of $|V_{td}|$ once x_s/x_d has been measured. We could also use it to estimate the value of x_s, but this is better done as follows.

We estimate the allowed range of x_s directly from the Standard Model calculation (2):

$$x_s = 1.2 \times 10^5 g(m_t) |V_{ts}|^2 f_s^2 B_{bs} ,$$

assuming that the B lifetime $\tau_s = \tau_d = 1.18$ psec, and that $\eta_s = \eta_d = 0.85$. Now $|V_{ts}| = |V_{cb}| = 0.046 \pm 0.010$, so that $0.0010 \leq |V_{ts}|^2 \leq 0.0032$ at 90% confidence level, with a central value of $|V_{ts}|^2 = 0.0021$. Also, $0.75 \leq g(m_t) \leq 3.1$ for 78 GeV $\leq m_t \leq$ 200 GeV. If we take $m_t = 140$ GeV as the most probable value, then $g = 1.06$ is the likely value. We also take $(0.1\text{GeV})^2 < f_s^2 B_{b_s} < (0.2\text{GeV})^2$, with a central value of $(0.15\ \text{GeV})^2$. Then we find a central value of $x_s = 6$ and a range

$$3 < x_s < 12$$

if we suppose that only one of the three uncertain factors in x_s moves to its limit. If two of the three factors are at their limits would could have $1.5 < x_s < 25$.

We close our theoretical review with some remarks on B_s-decay modes suitable for study of B_s mixing. The particle-antiparticle nature of the b quark inside the B meson must be determined both at $t = 0$ and at decay in order to observe the mixing phenomena. Hence the B meson being studied must decay to a 'self-tagging' mode.

From Table 4 of Ref. [21] the four most prominent decays of the B_s meson are to $D_s^- \pi^+$, $D_s^+ D_s^-$, $\bar{D}^0 K^0$, and $J/\psi\phi$, where each final-state could involve the spin-1 (or spin-0) partners of the stated mesons, and also could incorporate the hadronization of $q\bar{q}$ pairs. Of these, the modes $D_s^+ D_s^-$ and $J/\psi\phi$ will not be useful as they are not self-tagging. The loss of utility of the $J/\psi\phi$ mode eliminates a straightforward trigger for B_s-mixing studies. However, the presence of extra pions, or spin-1 particles in the remaining useful modes in no way decreases their utility. The total branching fraction of all-charged decay modes suitable for B_s-mixing studies will be quite large – at least several per cent.

3.2.2 Sensitivity of the μBCD to B_s Mixing

Equation (1) above expresses the number of B and $\bar{B}$ mesons at time t supposing we have N B_s mesons at $t = 0$. At a hadron collider we actually start with an equal number of B and $\bar{B}$ mesons at $t = 0$ (tagged by observation of the second B in the event), and so collect four decay distributions, labelled by the particle/antiparticle character at creation and decay. By taking the appropriate sum and difference of these four distributions we can isolate the distribution

$$D(t) = Ne^{-t} \cos xt,$$

while the number of B's left at time t is, of course, Ne^{-t}.

The value of x can be determined if the oscillations of $D(t)$ are well resolved. First we consider the statistical power required to determine x, supposing that the time resolution is perfect. A simple criterion is that the size of the oscillations must be clearly non-zero; we require that the first few quarter cycles each to have 25 events to maintain a 5-σ distinction. In, say, the 8th quarter cycle there are $\sim (N\pi/2x)e^{-4\pi/x}$ events, so we need $N \gtrsim 50xe^{4\pi/x}/\pi$. Then about 600 events would be needed to measure the value of x_s to 5-σ accuracy for any x from 8 to 25; larger numbers of events are required for larger x.

However, if the time resolution σ_t (on the value of the proper time t) deteriorates to a quarter cycle, the oscillation will become unrecognizable. Thus we desire a resolution $\sigma_t < \pi/2x$, and hence $\sigma_t < 1/16$ to resolve x up to 25. The achieved value of σ_t depends on the quality of the vertex detector. To a good approximation $\sigma_t \approx \sigma_z/c\tau$ where σ_z is the spatial resolution of the vertex detector, and τ is the B lifetime. Since $c\tau = 360$ μm for B's,

and $\sigma_z \sim 20$ μm is typically obtained with silicon vertex detectors, we expect that mixing parameters of $x \lesssim 25$ should indeed be resolvable. Extreme care in the construction of the vertex detector will be required to resolve larger values of x_s.

The argument of the preceding paragraph can be cast in a more formal manner. If the resolution on the proper time t is σ_t then the apparent distribution (1) of particles and antiparticles becomes

$$\begin{aligned} N_{B(\bar{B})} &= \frac{N}{2\sqrt{2\pi}\sigma_t}\int dt' e^{-(t-t')^2/2\sigma_t^2} e^{-t'}(1 \pm \cos xt') \\ &= \frac{N}{2} e^{-t} e^{\sigma_t^2/2}\left(1 \pm e^{-x^2\sigma_t^2/2}\cos x(t-\sigma_t^2)\right). \end{aligned}$$

If we form the difference $D(t)$ as before, the coefficient N is replaced by $N\exp[-(x^2-1)\sigma_t^2/2]$. Hence where $50xe^{4\pi/x}/\pi$ events would suffice to measure x_s to 5-σ assuming perfect time resolution, we need

$$\frac{50}{\pi} x e^{4\pi/x} e^{(x^2-1)\sigma_t^2/2}$$

events if the time resolution is σ_t. Again we infer that we need $\sigma_t < 1/x$ or there will be a deterioration in the statistical power of the data. As an example, if $\sigma_t = 1/16$ and $x_s = 25$ then we would need 2400 events, compared to the 600 required if $\sigma_t = 0$.

To form the distribution $D(t)$ used in the mixing analysis each decay must be tagged as to whether the B started as a particle or antiparticle. For the tag we look at the other B in the event. If we are to maintain a reasonable tagging efficiency, we must identify decays of the other B that contain neutrals. To have confidence that we are associating tracks with a B decay and not the primary hadronic interaction, the tracks of the second B must come from a secondary vertex. Neutral tracks are not useful for this. Hence we will have only a partial reconstruction of the second B in general. Without a mass constraint we cannot be sure that all charged tracks from the second B have been found, and so we will not be able, in general, to tell whether the second B was a B_u, B_d, or B_s.

If the second B is neutral, it may have oscillated before we detect it. Thus the tag cannot be perfect. Indeed, a neutral B with mixing parameter x decays in the opposite particle/antiparticle state to that in which it was created with probability $x^2/2(1+x^2)$. For a B_d with $x_d = 0.7$ the probability of a mistag is 1/6, but for a B_s with $x_s > 8$ it is essentially 1/2. The B_s oscillates so rapidly that is is useless as a tag.

If a fraction p of our events are mistagged, the distribution $D(t)$ describing the oscillation becomes $(1-2p)Ne^{-t}\cos xt$, and the error on x extracted from analysis of D grows by a factor $1/\sqrt{1-2p}$. It will now require $1/(1-2p)$ as many events to achieve a given statistical significance. This dilution of the tag is largely unavoidable at a hadron collider.

In summary, the number of tagged events required to measure the mixing parameter x to 5-σ when the resolution on proper time is σ_t and the mistagging probability is p is

$$\frac{50}{\pi(1-2p)} x e^{4\pi/x} e^{(x^2-1)\sigma_t^2/2}.$$

We estimate the dilution factor by recalling our hypothesis as to the relative product of the various B's, assumed uncorrelated with the type of the other B,

$$B_u : B_d : B_s = \frac{1-\epsilon}{2} : \frac{1-\epsilon}{2} : \epsilon.$$

We can then write

$$1-2p=\frac{1-\epsilon}{2}+\frac{1-\epsilon}{2}\frac{1}{1+x_d^2}+\epsilon\frac{1}{1+x^2}\approx 0.6,$$

using $\epsilon = 0.25$, $x_d = 0.7$, and $x_s > 8$. Our earlier requirement of 2400 perfectly tagged B_s decays for $x_s = 25$ and $\sigma_t = 1/16$ now becomes 4000 decays with a diluted tag.

In Table 3 we estimated the yield of tagged, reconstructed B_s decays to be 8,000 in 4 modes useful for an oscillation study, using all electron trigger/tag. If the muon trigger/tag is available the tagged B_s decays would increase by a factor of 1.6 (see Table 2) to 13,000. Other modes can be added as well, raising the yield to at least 25,000, or 6 times that needed to demonstrate the oscillation signal for $x_s < 25$. Equivalently, the μBCD could resolve B_s mixing for $x_s < 25$ in a year of running at a luminosity of only 10^{31} cm^{-2}sec^{-1}. A year of running at 5×10^{31} cm^{-2}sec^{-1} would allow measurement of x_s up to 35.

3.3 *CP* Violation

3.3.1 Theoretical Review

Study of CP violation in the B-meson system is the long-range goal of any B-physics program. A review of CP violation has been given by us in sec. 2.4.1 of Ref. [21] The main features are:

1. CP violation in the B system is not primarily due to the magnitude of CP violation in the mass eigenstates, $\epsilon_B \ll \epsilon_K$. However, the ratio of amplitudes of $|B^0\rangle$ and $|\bar{B}^0\rangle$ in the mass eigenstates is given by a pure phase. This phase is that of V_{td}, due to the dominance of the top-quark in the box diagram that governs B^0-$\bar{B}^0$ mixing.[31]

2. CP violation can be due to interference of two decay amplitudes with different weak phases. When comparing rates for $B^0 \to f$ and $\bar{B}^0 \to f$, the phase in the mass eigenstates can enter due to B^0-$\bar{B}^0$ mixing.[32]

3. If the final state f is a CP eigenstate then strong-interaction effects cancel, and the CP violation can be entirely due to the phase in the mass eigenstates.[33] Hence a direct measurement of the phase of a CKM-matrix element is possible.

4. There can be a large weak phase in the decay amplitudes also, that of V_{ub}. (This phase can only enter in higher order in K decays.) As a consequence there are four classes of neutral-B decays to CP eigenstates, yielding three different measures of phases in the CKM matrix.[28]

CP violation is manifested in a nonzero value of the asymmetry

$$A_f(t)=\frac{\Gamma(B^0(t)\to f)-\Gamma(\bar{B}^0(t)\to \bar{f})}{\Gamma(B^0(t)\to f)+\Gamma(\bar{B}^0(t)\to \bar{f})}\,. \tag{3}$$

If we consider a nonleptonic final state f that is a CP eigenstate this asymmetry can be calculated from

$$\Gamma(\overset{(-)}{B}{}^0_q(t)\to \overset{(-)}{f}) \;=\left|\langle f|B^0_q\rangle\right|^2 e^{-t/\tau}\left[1\mp \mathrm{Im}\,\alpha_f \sin x_q\tfrac{t}{\tau}\right] \tag{4}$$

Now Eq. (3) assumes the elegantly simple form

$$A_f(t) = -\,\mathrm{Im}\,\alpha_f \sin x_q \frac{t}{\tau}\ . \tag{5}$$

In this

$$\alpha_f = \frac{q}{p}\rho_f\ . \tag{6}$$

The complex numbers p and q describe the B-$\bar{B}$ mixing in the expression for the time dependence of B-meson states:

$$\begin{aligned} |B^0(t)\rangle &= \ \ f_+(t)|B^0\rangle + \tfrac{q}{p} f_-(t)|\bar{B}^0\rangle\ , \\ |\bar{B}^0(t)\rangle &= \tfrac{p}{q} f_-(t)|B^0\rangle + \ \ f_+(t)|\bar{B}^0\rangle\ . \end{aligned} \tag{7}$$

Here, $|B^0\rangle$ represents a pure B^0 state at $t = 0$. We have

$$\begin{aligned} f_+(t) &= \ \ e^{-iMt}e^{-\Gamma t/2}\cos(\Delta M t/2)\ , \\ f_-(t) &= ie^{-iMt}e^{-\Gamma t/2}\sin(\Delta M t/2)\ . \end{aligned} \tag{8}$$

and

$$\frac{q}{p} = \sqrt{\frac{M_{12}^* - \frac{i}{2}\Gamma_{12}^*}{M_{12} - \frac{i}{2}\Gamma_{12}}} \approx \sqrt{\frac{M_{12}^*}{M_{12}}} = \text{a pure phase.} \tag{9}$$

M_{12} is calculable from the Standard Model box diagram for B_q^0-$\bar{B}_q^0$ mixing ($q = d, s$), which is dominated by t-quark exchange. We express the result in terms of the Cabibbo-Kobayashi-Maskawa (CKM) matrix elements, here parametrized as[34]

$$V_{CKM} = \begin{pmatrix} V_{ud} & V_{us} & V_{ub} \\ V_{cd} & V_{cs} & V_{cb} \\ V_{td} & V_{ts} & V_{tb} \end{pmatrix} \approx \begin{pmatrix} 1 - \frac{\lambda^2}{2} & \lambda & A\lambda^3\rho e^{-i\delta} \\ -\lambda & 1 - \frac{\lambda^2}{2} & A\lambda^2 \\ A\lambda^3(1 - \rho e^{i\delta}) & -A\lambda^2 & 1 \end{pmatrix}. \tag{10}$$

In this parametrization the CKM matrix elements are expanded in powers of λ, the Cabibbo angle ($\lambda = 0.22$).[2]

We can then write

$$M_{12} \sim f(M_t)\left(V_{tb}V_{tq}^*\right)^2\ , \tag{11}$$

and therefore the phase information from the mixing is

$$\frac{q}{p} = \begin{cases} (V_{tb}^*/V_{tb})(V_{td}/V_{td}^*) = (V_{td}/V_{td}^*) \equiv e^{-2i\phi}\ , & (B_d), \\ (V_{tb}^*/V_{tb})(V_{ts}/V_{ts}^*) \simeq 1\ , & (B_s). \end{cases} \tag{12}$$

In Eq. (12), ϕ is the phase of V_{td}.

The parameter ρ_f in Eq. (6) is the ratio of decay amplitudes

$$\rho_f = \frac{\langle f|\bar{B}^0\rangle}{\langle f|B^0\rangle}\ , \qquad \bar{\rho}_f = \frac{\langle \bar{f}|B^0\rangle}{\langle \bar{f}|\bar{B}^0\rangle}\ . \tag{13}$$

[2] In the exact form for V_{CKM} other terms have phases as well, but they are of higher order in λ. Large phases appear only in V_{ub} and V_{td}.

When only one amplitude contributes to $B^0 \to f$ (and its CP-conjugate to $\bar{B}^0 \to \bar{f}$) then

$$\left|\langle f|B^0\rangle\right| = \left|\langle \bar{f}|\bar{B}^0\rangle\right|, \qquad \left|\langle \bar{f}|B^0\rangle\right| = \left|\langle f|\bar{B}^0\rangle\right|, \tag{14}$$

i.e., $|\rho_f| = |\bar{\rho}_f|$ and ρ_f is also a pure phase.

The phase information in the decay depends on whether the b-quark decays into a c- or a u-quark:

$$\rho_f = \begin{cases} (V_{ub}/V_{ub}^*) \equiv e^{-2i\delta}\ , & b \to u, \\ (V_{cb}/V_{cb}^*) = 1\ , & b \to c. \end{cases} \tag{15}$$

As before, δ is the phase of V_{ub}.

Since both q/p and ρ are pure phases, then α is also, and Eq. (6) for the CP-violating asymmetry can be written

$$A_f(t) = \sin 2\varphi \sin x_q \frac{t}{\tau}, \tag{16}$$

where we define $\alpha \equiv e^{-2i\varphi}$. Referring to Eqs. (12) and (15) it can be immediately seen that there are four classes of decays measuring different combinations of phases in the CKM matrix. These are summarized in Table 4.

Table 4: The four classes of CP violation in the decay of neutral B mesons to CP eigenstates.

Class i	Parent B	Quark Decay	Typical Mode	Phase φ_i	$\sin 2\varphi_i$
1	B_d	$b \to c$	$B_d \to J/\psi K_S$	ϕ	$\mathrm{Im}(V_{td}^*/V_{td})$
2	B_d	$b \to u$	$B_d \to \pi^+\pi^-$	$\delta + \phi$	$\mathrm{Im}(V_{ub}^*/V_{ub})(V_{td}^*/V_{td})$
3	B_s	$b \to u$	$B_s \to \rho K_S$	δ	$\mathrm{Im}(V_{ub}^*/V_{ub})$
4	B_s	$b \to c$	$B_s \to J/\psi\phi$	0	0

The CP violation in class-1 decays originates in the mass matrix, that of class-3 decays is from the decay amplitude, while that of class-2 decays is due to both effects. In addition to measuring the decay asymmetries in classes 1-3, it will be an important test of the Standard Model to search for CP violation in class-4 decays. A nonzero measurement of a CP asymmetry in this class would be a clear signal of physics beyond the Standard Model.

The CKM phases that govern the three classes of nonzero asymmetries are often demonstrated using the unitarity triangle,[35] shown in Fig. 11. The unitarity of V_{CKM} implies

$$V_{td} + \lambda V_{ts} + V_{ub}^* \approx 0. \tag{17}$$

Hence, if these three complex matrix elements are regarded as vectors, they form a closed triangle. The goal is then to measure the three interior angles φ_1, φ_2, φ_3, and to see if the triangle closes, *i.e.*, *to see if the angles add up to* 180°. These three angles are exactly the three CKM phases that appear in the above classification of CP asymmetries: $\varphi_1 = \phi$, $\varphi_2 = \delta + \phi$, and $\varphi_3 = \delta$.

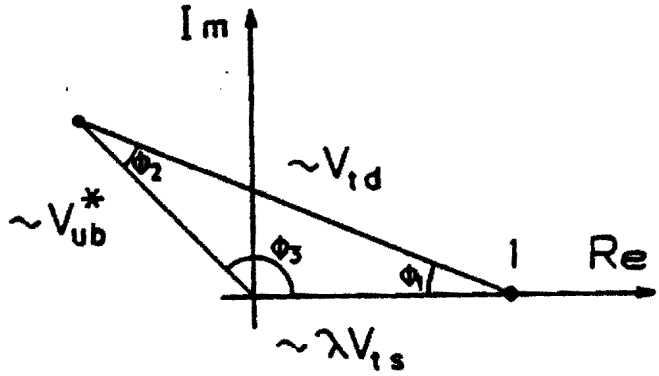

Figure 11: The unitarity triangle.

The allowed regions for the φ_i, based on present knowledge of the CKM matrix, are shown in Fig. 12.[21]

As a brief digression, it is interesting to examine why CP-violation measurements in the Kaon system do not directly access the phases of the CKM matrix. Many of the needed ingredients are present: $\pi\pi$ is a CP eigenstate, $|q/p|_K \simeq 1$, and a single weak amplitude dominates the decay. However, the CKM structure of the amplitude (and of K^0-$\bar{K}^0$ mixing) involves only the *uc-ds* submatrix to a first approximation, and the elements V_{ub} and V_{tb} that have nontrivial phases enter only as small correction. The Kaon system does not 'know' enough about the third quark generation to be an ideal laboratory for CP violation.

3.3.2 Sensitivity of the μBCD to CKM Phases

The principal result of the preceding subsection is that the time-resolved CP-violating asymmetry in the decay of neutral B mesons to CP eigenstates can be written

$$A(t) = \frac{\Gamma(B_q^0(t) \to f) - \Gamma(\bar{B}_q^0(t) \to \bar{f})}{\Gamma(B_q^0(t) \to f) + \Gamma(\bar{B}_q^0(t) \to \bar{f})} = \sin 2\varphi \sin x_q t/\tau, \tag{18}$$

where φ is a phase directly related to CKM-matrix elements, and x_q is the mixing parameter of the B_q mesons. Strictly, this relation holds only when the decay is dominated by a single weak amplitude, and the interference required to produce an asymmetry arises from the mixing.

To extract the amplitude, $\sin 2\varphi$, of the time-resolved asymmetry $A(t)$ we must note a 'dilution factor' not present in a time-independent asymmetry. For a small mixing parameter x_q, only the first wiggle in Eq. (4) will be significant (due to the relatively rapid decay), and the time-resolved asymmetry measurement reduces to integrating over this wiggle, which becomes equivalent to a time-integrated measurement. That is, the effective asymmetry is

$$A \to \frac{x_q}{1 + x_q^2} \sin 2\varphi, \qquad \text{small } x_q,$$

obtained by integrating over Eq. (4) before forming the asymmetry A.

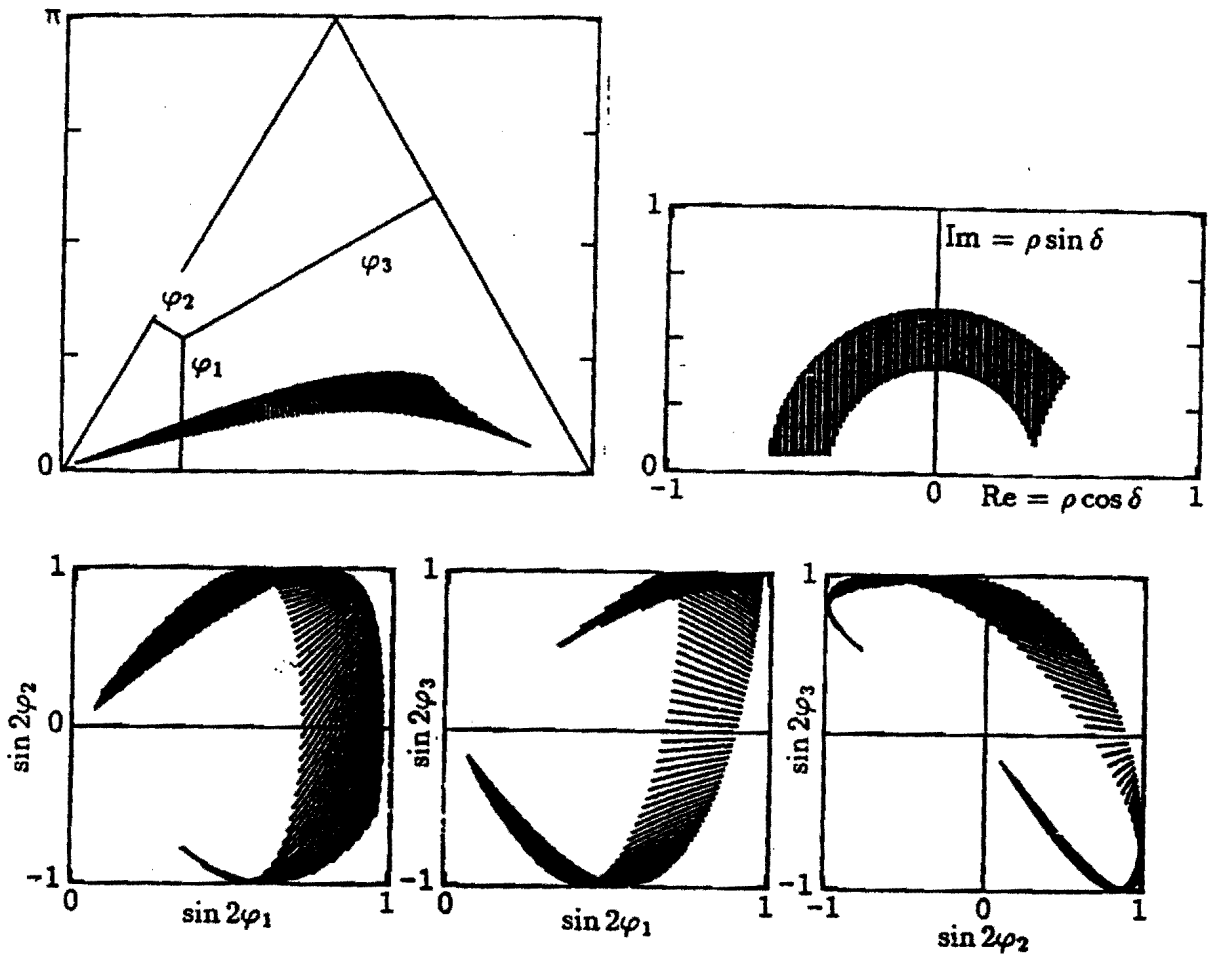

Figure 12: Allowed regions of the φ_i at 90% confidence, based on present knowledge of the CKM matrix. In the triangle plot, $\varphi_1 + \varphi_2 + \varphi_3 = \pi$. The top-quark mass was taken to be 150 GeV/c^2.

For large x_q, however, $\sin x_q t/\tau$ oscillates before the B's decay, and the asymmetry measurement can be thought of as comparing alternate half cycles. In this case the effective size of the asymmetry is only reduced by the average amplitude of a half cycle of a sine wave:

$$A \to \frac{2}{\pi} \sin 2\varphi, \qquad \text{large } x_q.$$

A complete analysis shows that we can write

$$A = D(x_q) \sin 2\varphi \qquad \text{with} \qquad D = \frac{x_q}{1 + x_q^2} \coth(\pi/2x_q).$$

(The dilution factor D is the Laplace transform of $|\sin x_q t/\tau|$, which arises because the effective signal is $e^{-t/\tau} |\sin x_q t/\tau|$ compared to the exponential-decay 'background.')

Although the dilution D due to mixing is annoying, without mixing the richness of CP violation in the B system would be greatly reduced.

Assuming our vertex detector has sufficient accuracy to resolve the mixing oscillations, the statistical significance in standard deviations of a measurement of $\sin 2\varphi$ via the effective asymmetry $A = D \sin 2\varphi$ is

$$S = \frac{\sin 2\varphi}{\sigma_{\sin 2\varphi}} = \sqrt{N}\frac{A}{\sqrt{1-A^2}} = \sqrt{N}\frac{D \sin 2\varphi}{\sqrt{1 - D \sin^2 2\varphi}},$$

where N is the total number of (true) reconstructed, tagged decays. The minimum value of $\sin 2\varphi$ that could be resolved to three standard deviations with N events is then

$$\sin 2\varphi_{\min,3\sigma} = \frac{3}{D\sqrt{N+9}}.$$

To perform the asymmetry measurement we must tag the other B in the event to determine the initial particle/antiparticle character of the B that decays to the CP eigenstate. At a hadron collider we will likely have only a partial reconstruction of the second B, and will not distinguish B_u, B_d, and B_s. Because of the mixing of the neutral B's there will be a probability $p \approx 0.2$ of a mistag, which dilutes the significance of the asymmetry measurement. The Kaon tag is subject to an additional mistagging probability due to 'wrong-sign' Kaons from D-meson decay. We have estimated elsewhere,[22] that the total mistagging probability is $p \approx 0.3$ for the Kaon tag.

We also consider the effect of backgrounds in our sample of CP-eigenstate decays, supposing that for each true reconstruction of $B \to f$ there are b false reconstructions that exhibit zero asymmetry. Then $1/b$ is the signal-to-noise for reconstruction of this decay mode.

Taking into the account these two effects, the apparent rate for B ($\bar{B}$) decay will be

$$\Gamma(\overset{(-)}{B}{}^0_q(t) \to \overset{(-)}{f}) = \left|\langle f | B^0_q \rangle\right|^2 e^{-t/\tau}\left[1 + b \mp (1-2p)\,\mathrm{Im}\,\alpha_f \sin x_q \frac{t}{\tau}\right],$$

and the true CP-violating asymmetry A_{CP} will be related to the asymmetry $A_{\rm obs}$ observed in the laboratory by

$$A_{CP} = \frac{1+b}{1-2p} A_{\rm obs}.$$

As a consequence, the statistical power of a sample of N true events is reduced, and we now have (assuming that b and p are well known)

$$\sin 2\varphi_{\min,3\sigma} = \frac{3(1+b)}{D(1-2p)\sqrt{N(1+b)+9}}.$$

The expectations for rates of four decays to CP eigenstates have been summarized above in Table 3. While the decays $B_d \to J/\psi K^0_S$ and $B_s \to J/\psi\phi$ will be relatively background free, this is not the case for $B_d \to \pi^+\pi^-$ and $B_s \to \rho K^0_S$ for which we suppose the background-to-signal ratio is $b \approx 1$. Then we estimate the sensitivity of the μBCD to the CKM phases as given in Table 5.

Table 5: The minimum values of $\sin 2\varphi_i$ resolvable to three standard deviations by the μBCD in 10^7 sec of running at luminosity of 5×10^{31} cm^{-2}sec^{-1}. The factor $1-2p$ is the analyzing power of the tag which has a probability p for a wrong tag. b is the background to signal for the final-state reconstruction. The dilution factor D due to mixing is given by $x_q \coth(\pi/2x_q)/(1+x_q^2)$.

Angle	Mode	Tag	Tagged Events	$1-2p$	b	x_q	D	$\sin 2\varphi_{\min,3\sigma}$
φ_1	$B_d^0 \to J/\psi K_S^0$	e,μ	580	0.60	0.1	0.7	0.47	0.46
φ_1	$B_d^0 \to J/\psi K_S^0$	K	2,200	0.40	0.1	0.7	0.47	0.36
φ_2	$B_d^0 \to \pi^+\pi^-$	e,μ	2,000	0.60	1.0	0.7	0.47	0.45
φ_3	$B_s^0 \to \rho^0 K_S^0$	e,μ	20	0.60	1.0	~ 10	0.64	1.00
φ_4	$B_s^0 \to J/\psi\phi$	K	1,300	0.40	~ 0.1	~ 10	0.64	0.23

The values of φ_1 and φ_2 that could be explored by the μBCD have some overlap with the current allowed regions (shown in Fig. 12). In 10 years of running a large fraction of the allowed region could be explored. However, the results in Table 5 represent a maximum of optimism as to the detector performance, and the experiment may well achieve less sensitivity. We feel it unwise to place the main emphasis of the B-physics program on the search for CP violation at the expense of the much more accessible physics of B_s mixing.

The sensitivity of the μBCD is, we believe, somewhat better than could be achieved in any upgrade of CDF and D0 (other than converting them to μBCD).

4 Detector Subsystems: Progress Reports and Future Directions

The BCD Collaboration has been investigating the physics potential, conceptual design, and related technical issues of a dedicated B-physics program initiated at Fermilab and culminating at the SSC. In the following Appendices we summarize our work to date on the technical issues, draw conclusions, and specify the direction of future work. Given limited resources, we have concentrated our efforts on the key areas which are unique to B physics: the silicon vertex detector, hadronic particle identification, and tracking. The work has been supported through a variety of R&D projects including Fermilab T-784, and the SSC Generic and Subsystem R&D programs.[10, 11, 12, 13, 14, 15, 16, 17, 18, 20]

5 Appendix A: Silicon Vertex Detector

The silicon vertex detector for a hadron collider is, by necessity, ambitious and complex. The basic design criteria have already been discussed in the introduction. Considerations

of full acceptance (roughly ± 4 units of pseudorapidity), low mass, and the finite size of the interaction region lead to a device 3-4 m long, 10-20 cm in radius, and containing 1-2 square meters of double-sided AC-coupled silicon detectors. A spatial accuracy of 5-7 μm for angles of incidence up to 60° on the detector requires detectors of strip pitch 25-50 μm and digitization of the signals, which can only be accomplished in a cost-effective manner with on-detector VLSI chips with ambitious specifications. This detector will have in excess of 1 million channels distributed over $\sim$ 1000 wafers.

There have been several iterations of the vertex detector concept, starting with a design which placed the silicon detectors inside of the vacuum pipe, which was largely the work of P. Karchin.[6] This arrangement was superceded by the proposal of Kalbfleisch and McDonald[37] and further refined by Karchin, Kalbfleisch, and McDonald into the present model of discs and barrels located outside the vacuum pipe.

The structure of the current vertex detector conceptual design is shown in Fig. 13 and consists of self-supporting silicon modules housed in one rigid external beryllium tube. All modules have the same mechanical structure. In the central region both the barrel and disk areas are active: in the forward region only the disk sections are instrumented. This design contains no ladders for support of the silicon detectors or readout chips. It relies on the structural integrity of the silicon wafers for internal alignment and uses the tube to align individual modules with respect to each other. The placement of the preamplifier chips directly on the silicon detector and the strip directions are indicated in Figs. 14 and 15. The stripe orientation was chosen for ease of preamplifier placement.

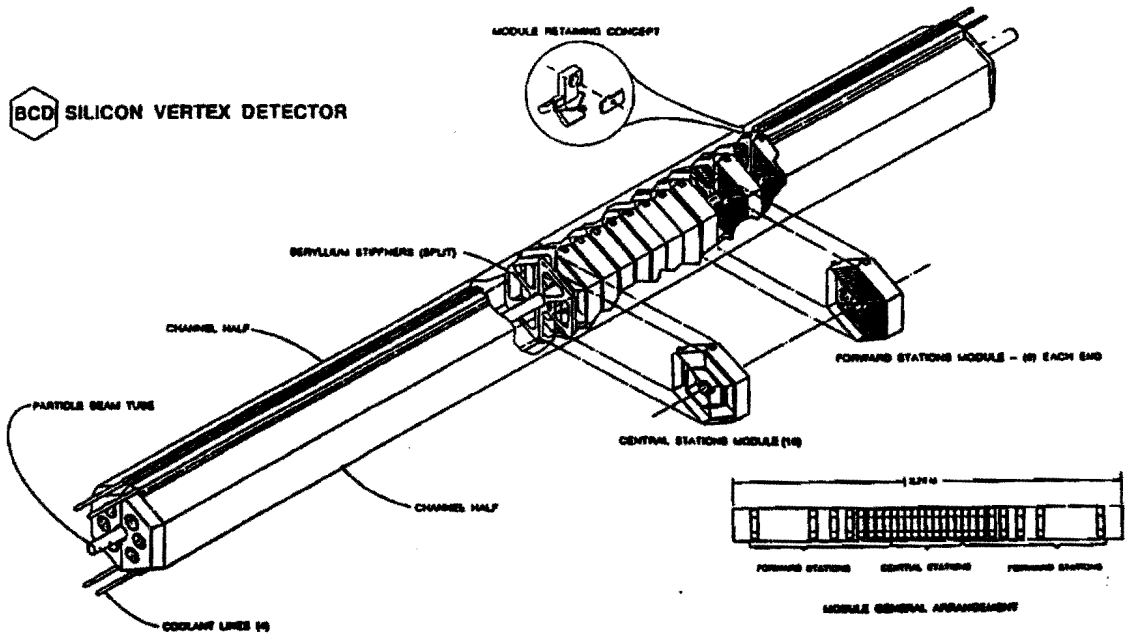

Figure 13: The BCD vertex detector with a cutout of the 'gutter' to show the self-supporting silicon modules inside.

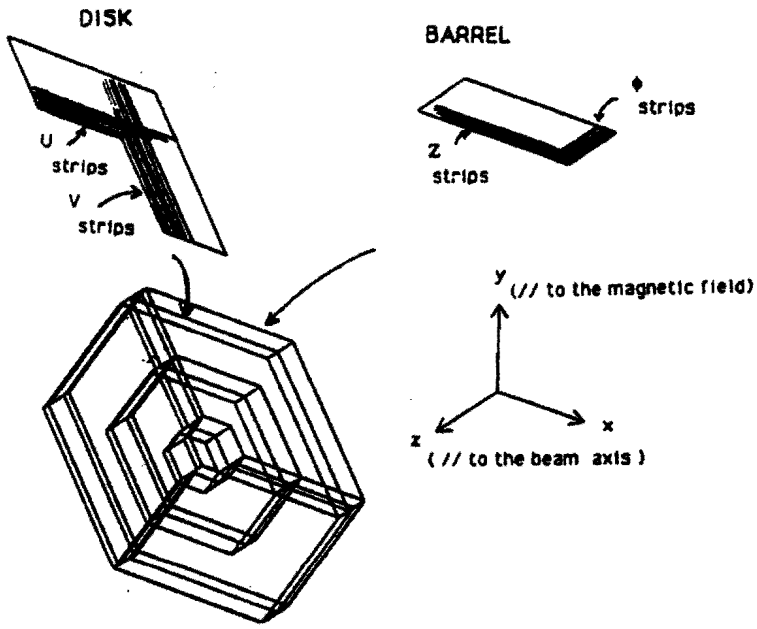

Figure 14: A representation of a single module of the Central portion of the vertex detector shown in Fig. 13. Disk and barrel silicon detectors are glued together into a hexagonal structure. The disks are mounted in a helicoidal pattern to allow a net longitudinal air flow through the detector for cooling. The stripes on the disk detectors are aligned along u and v axes which permits the readout chips to be placed at the outer edges only. The inner radius of the silicon is 1.5 cm, and the outer is 10 cm. Each module is 4.8 cm long.

The BCD vertex detector design contains three features not present in other existing or proposed collider vertex detectors.

1. The device is very long, roughly 3 meters along the beam axis. This length is necessary to provide vertex coverage over $\pm\eta = 4$.

2. The central rapidity region is a complex self-supporting structure composed of silicon barrels and disks extending over roughly $\pm 2\sigma_z$, where σ_z is the r.m.s. length of the luminous interaction region. This design permits vertex capability for tracks of all angles. A shorter interaction region would reduce the length of the detector and would therefore simplify the design. One consequence of the long design is that an equally long support structure is needed. This structure must bear the load of all the modules and yet be composed of a thin, low-Z material to minimize multiple-scattering effects. The proposed structure is a beryllium cylindrical tube, 10-20 cm in radius and is called a **gutter**.

3. The vertex detector will contain more than 1 million readout channels, each dissipating at least 1 mWatt of power into the structure. The detailed design of the gutter is

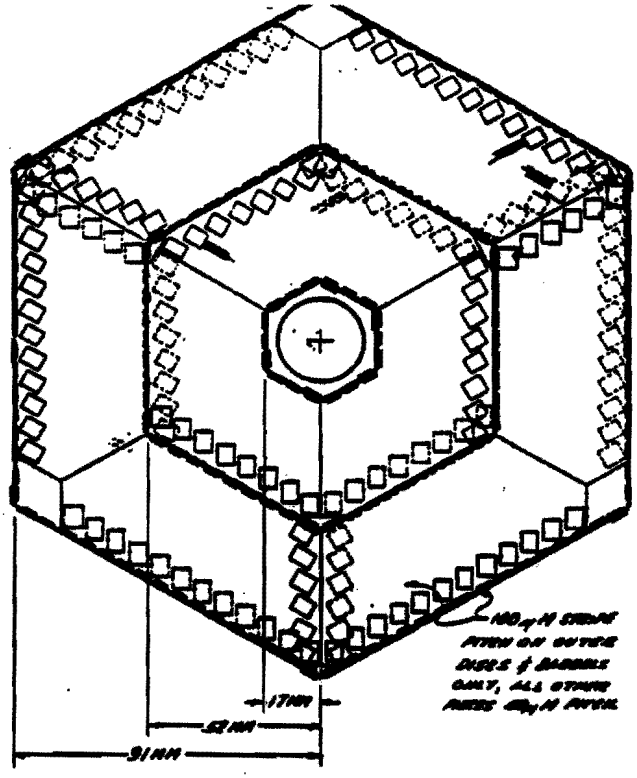

Figure 15: An end view of a BCD silicon vertex detector module. The preamplifier locations and strip orientation are indicated. The dashed lines refer to the ohmic side of the wafer and the solid lines refer to the diode side.

primarily concerned with heat removal using axial air flow while maintaining structural rigidity.

The scope of this detector is well beyond that of devices presently being built by CDF and groups at CERN which contain $\sim 10^4$ channels. The CCD detector of SLD has large numbers of channels, but its readout is much too slow to be relevant for the hadron-collider environment.

As soon as the conceptual design allowed we started four projects to clarify the technical problems:

1. Mechanical construction: stability, alignment, heat dissipation, and cables.

   We consider the mechanical design the most challenging and difficult part of the vertex-detector R&D. Work on this critical topic has been undertaken at Fermilab by H. Jöstlein, C. Lindenmeyer, and coworkers.

2. The silicon detectors themselves: AC coupling, double sided readout.

   To help prepare for the effective use of new silicon detectors and readout chips, a program of evaluation of existing silicon strip detectors and chips has been carried out in the M-Test beam, headed by P. Karchin of Yale and P. Skubic of U. Oklahoma.

3. Electronics: specification of requirements, design and construction of a new chip (BVX).

To reduce the mechanical complexities, the electronic readout design **must minimize both power dissipated and size and weight of the vertex-detector cable plant.** A VLSI design with substantial on-board digital processing can reduce the number of cables needed to read out the vertex detector.

The 2.5-MHz crossing frequency of the Tevatron upgrade renders more difficult the task of designing low-noise preamplifiers with low power consumption. Further, there is insufficient time between bunch crossing to have separate time frames for the operation of the analog and the digital circuitry. No existing readout chip combines these two functions with simultaneous operation.

We have embarked on an R&D program led by R. Yarema[36] of Fermilab to produce a new generation of readout chip, called the BVX chip. This chip could also be used in the readout of RICH counters, TRD's, or other devices not requiring a nsec timing capability, and will be the basis of a detector-wide integrated approach to the front-end electronics.

4. Pixel detectors.

   A successful pixel detector would enormously help the design and performance of the silicon vertex detector. We did not feel it prudent to incorporate pixel detectors into the initial baseline conceptual design. However, we have enthusiastically supported their development. A silicon pixel detector was tested in the M-Test beamline as part of T-784 by T. Collins of Hughes Aircraft, and E. Arens and G. Jernigan of U.C. Berkeley Space Sciences Lab and there are plans to continue this work in 1991.

5. Detailed Monte Carlo simulation of the benchmark design.

   Simulations of the vertex detector system performance were begun by P. Karchin of Yale, L. Roberts of Fermilab (now SSCL), continued by K. McDonald of Princeton, and greatly extended by P. Lebrun of Fermilab.

5.1 Vertex-Detector Mechanical and Thermal Studies

The crucial requirement of the vertex-detector design is to **maintain the alignment to several microns over long times** within a module, once equilibrium temperature is reached. It was decided very early in the design stage that a mechanical/thermal model should be constructed. We describe the work over the last two years, led by H. Jöstlein of Fermilab. The majority of the work was done during the last two summers by two high-School science teachers, and by undergraduate students.

During the first year a full-scale brass model of the gutter was constructed, and alignment and cooling tests were performed. The following year we made improvements by adding dummy modules inside of the gutter to impede air flow. The following three subsections summarize this set of results. In parallel with the gutter tests, C. Lindenmeyer and H. Cease have been investigating the design and construction of the silicon modules. The last section outlines our plans for future work.

5.1.1 The Brass Gutter Model

The two halves of the support tube, called *gutters* because of the resemblance to rain troughs or gutters, were constructed of 10-mil-thick brass, since brass has approximately the same mechanical characteristics as beryllium. (The elastic modulus of brass is 16×10^6 lbs/in^2 while that of beryllium is higher, 42×10^6 lbs/in^2. The thermal expansion coefficients are 20.5×10^{-6}/°C and 11.3×10^{-6}/°C for brass and beryllium, respectively.) Webbings, also made of 10-mil brass, are soldered to the inside to add stiffness to the overall structure and to support the modules. Water channels are soldered to the outside of the gutter for cooling studies. The arrangement of the reinforcing webs is shown in Fig. 16.

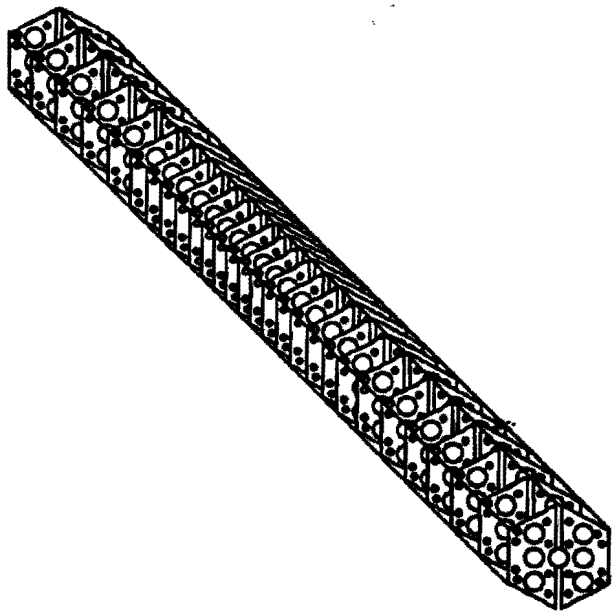

Figure 16: The reinforcing web arrangement shows the approximate spacing along the gutter and the holes that allow axial gas flow.

The end view and support stand of the two halves of the gutter is shown in Fig. 17.

Eight heating strips were placed inside the gutter to simulate the 1-kW heat load from 1 million 1-mW preamplifiers. Cooling was accomplished with fans, blowing air in from the end of the gutter, and with water flowing in the brass channels on the surface of the gutter. The air- and water-cooling configuration is shown in Fig. 18.

5.1.2 Mechanical and Thermal Study of the Gutter (1989)

The goal of the initial studies was to establish the stiffness and thermal stability of the two-gutter assembly, and the heat-removal capability of the cooling system.[38] Considerable effort was devoted to understanding the sources of experimental error in the measurements.

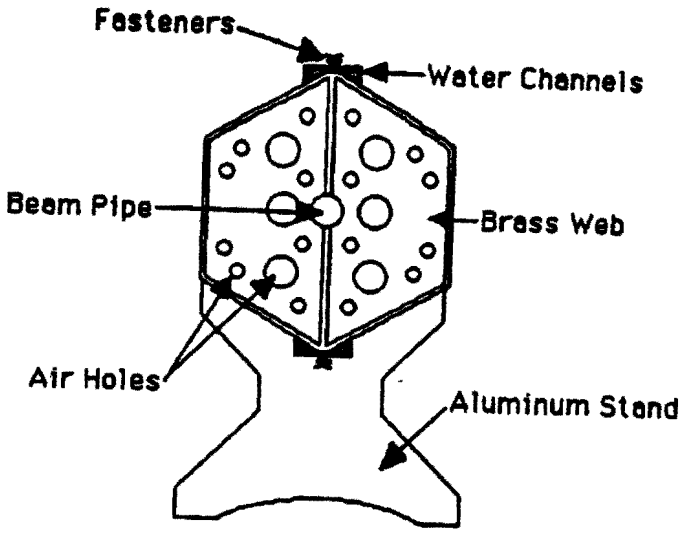

Figure 17: End view of the brass model of the gutter.

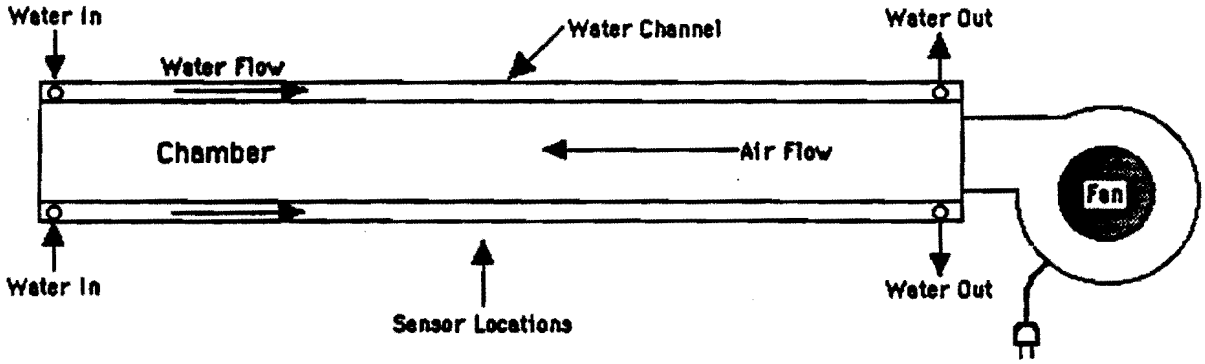

Figure 18: Air- and water-cooling configuration.

The gutter assembly was in the shape of a hexagonal prism, 120 inches long, and 9 inches in 'diameter.' The stiffness of the brass gutter assembly was such that is required an 800-gm weight applied at its midpoint to deflect the structure by 1 mil. The eventual Be gutter will have a modulus of elasticity, and hence stiffness, 2.5 times that of brass.

To study the thermal stability of the gutter it was cooled below ambient temperature by as much as 8°F and its position measured relative to a base at room temperature. Once the gutter was properly supported so that it was free to expand and contract, its motion was strictly consistent with the thermal-expansion coefficient of brass: 1 mil/°F over the 9-inch transverse width of the gutter. Recall that the thermal-expansion coefficient of brass is twice that of beryllium (and eight times that of silicon). Hence if we desire 5-μm mechanical stability, the beryllium-gutter temperature must be maintained constant to within 0.4°F.

In the third study, 1000 Watts of power were applied to the gutter via the heating strips. The consequent thermal expansion of the gutter was held to 1-2 mils by the combined cooling of 120 g/s air flow and 50 g/s water flow. Further studies showed that most of the cooling effect was due to the air flow and not the water; the heat transfer to the water needs to be improved. In this test no detector modules were mounted inside the gutter, and hence the impedance to the air flow was much less than will be the case in the full detector assembly.

5.1.3 Studies of Local Heating at the Amplifiers

The global heating studies of the gutter, described above, were followed by studies of the local heating of amplifiers on silicon detector modules.[39] Here the question was how hot would the amplifiers get under a nominal heat load, when cooled by an air flow. To answer this a model of a silicon detector module (Fig. 14) was constructed with resistors to simulate the local heat loads of the VLSI readout chips. Three such models were placed in the gutter and cooled with an air flow. During this study information was also obtained as to the resistance of the detector modules to the air flow.

A complete module is expected to dissipate 150 Watts if each silicon strip channel consumes 1 mW. In the test, only 1/3 of one module was powered, to total load of 50 Watts. The air flow rate with the same fan as before, was now only 76 g/s, due to the air resistance of the three modules placed in the gutter. Temperature sensors were mounted on several of the powered resistors, and temperature rises of about 10°F were observed.

These results are encouraging in that if a nominal air flow of about 100 g/s can be delivered into the detector, the temperature rise at the amplifiers will be acceptably small – 10°F.

The air resistance per module was observed to be such that the pressure drop was 0.6 inches of water across the module. Hence a full detector of some 20 modules would require a pressure head of 12 inches of water = 0.03 atmospheres.

5.1.4 Further Tests (1990)

Additional tests were performed during 1990.[40] They were studies of the thermal expansion of the gutter with 2000-Watts power dissipation, of the effects of mechanical impulses on the gutter, of vibration of the gutter with and without detector modules installed, and air-flow measurements with the detector modules in the gutter. Limits to the instrumentation

were uncovered, in particular the large temperature sensitivity of the proximity sensors. Preliminary conclusions are:

- The proximity-sensor-readout electronics are sensitive to temperature. In some cases we found 30% of the apparent motion was due to temperature effects in the electronics. The instrumentation must be improved for further progress.
- The behavior of the gutter with 2000 Watts agrees in an understandable way with the results at 1000 Watts.
- There are known defects in the mechanical assembly of the first gutter that limit its utility in further studies.
- With brass mockups of the detector modules installed, there is significant vibration at the center of the gutter when the fan is on. Typical values are 0.03 mils peak-to-peak. However, the 3-point kinematical mount shields the module from the vibrations on the gutter. Typical values of vibration of the detector modules are less than 0.01 mils.
- With 3 detector modules installed, and 2000 Watts applied to the whole gutter assembly via heating strips, the air-temperature difference between the inlet and outlet of the gutter was found to be 45°F. This is much higher than desired, but is consistent with the reduced mass-flow rate (86 g/s) of the cooling air due to the resistance of the modules. It was not possible with the available fans to increase the mass-flow rate. When the needed flow-rate becomes available, we calculate that the resulting forces on the detector modules are still within acceptable limits; possible effects of vibrations must be explored.

5.1.5 Module Construction

The design for an individual silicon module is shown in Fig. 14. The silicon wafers themselves are the structural elements. These wafers are glued together with a small triangular pyrex support at the silicon-silicon joint for added strength with little additional material. The VLSI readout chips are glued directly to the silicon wafers. The R&D issues associated with the design are:

1. Accurate and feasible assembly techniques.
2. Mechanical rigidity.
3. Compatibility of the adhesive with electrical performance.
4. Local heating of the chips.
5. Cabling.

The first (uninstrumented) silicon module will be assembled this Fall as soon as the pyrex prisms arrive. The silicon wafers have been cut. The assembly will test the constructibility and mechanical rigidity of the module. The cooling and mechanical tests of the silicon module will require more precise alignment sensors than were used in the gutter studies.

A evaluation of commercially available glues was started last Summer by H. Cease, an undergraduate student from IIT, and C. Lindenmeyer of Fermilab. An acceptable adhesive must be strong, have good creep properties, be insensitive to radiation, and be soluble in some solution in case we need to dismantle the module for repair. Most importantly, the adhesive must not adversely affect the electrical performance of the silicon strip detectors.

Three adhesives were tested: Locktite 324, NOA 81 (a UV-curing prepolymer acrylic), and Masterbond UV15-7 (a UV-curing epoxy). All three adhesives are soluable in trichloroethylene and methylene chloride.

A 'T'-shape was formed with two pieces of silicon glued at right angles using the pyrex support at the joint. A small weight was applied to the silicon and a proximity sensor was used to determine the deflection at various temperatures. All samples survived a 65-gram weight at 160°F for 3 hours without detectable motion. However, the NOA81 and Masterbond adhesives failed with an 85-gram weight after 30 minutes. All samples survived the 85-gram weight at 0°F for 3 hours.

In addition, 'creep' tests were performed over a period of a week and no creep was observed. Finally, we have arranged for an exposure of a glue joint at Argonne National Laboratory to a neutron flux of 10^{14} $cm^{-1}sec^{-2}$. These results are expected within the next few months.

We will repeat the creep and adhesive tests with the full module.

Given the successful results of the glueing studies, we are ready to study the effect of local heating of the silicon detector by the readout preamplifier. The increased heating tends to decrease the signal/noise performance of the readout chip and may cause the glue to soften. It may also affect the performance of the readout chip itself. Increased cooling or an alternate method of mounting the readout chips may be necessary.

On another front, C. Lindenmeyer has been studying possible assembly procedures for the modules that will not be excessively labor intensive and that can attain the required accuracy.[41] He has developed assembly plans using special fixtures and a 3-axis coordinate-measuring machine. Once the lessons from the hand assembly of the first module have been assimilated, further progress will require access to such a machine.

5.1.6 Future Gutter and Module Studies

The building and testing of this model has been labor intensive; large amounts of data have been recorded and analysed. The construction and study of this model has been very instructive. However, **this model has been pushed to its limits.** A new model is necessary, built to more exacting specifications. The proximity sensors must be replaced by ones with greater accuracy; the present set is limited to about 0.5-mil accuracy. The gutter must be redesigned and constructed of beryllium since the brass flexes during heating and cooling. A suspension-type support structure of the gutter assembly is needed if we are to advance beyond the problems associated with mounting it directly on a steel table. The air-flow system is inadequate and needs at minimum a new pump. The liquid-cooling system was not optimized and more channels, perhaps of different shapes, should be used on a new model. In addition, the model will have to be located in an environmentally controlled room as our results indicate we are sensitive to temperature shifts.

The next step would be a system test of a full-length gutter loaded with all the silicon

modules, of which a number of wafers would be instrumented. Besides the usual mechanical and thermal studies, the assembly would be placed in the test beam and the performance studied.

Finally, our understanding of many of the issues has progressed to the point where we would like to initiate a simulation of the model to proceed in parallel with the laboratory studies. This simulation should use a finite-element analysis program such as ANSYS, and should incorporate both a stress-analysis and heat-flow study.

5.2 The BVX Readout Chip

The initial work on readout issues generated the specifications for the BVX chip, taking into account the broader issues of the B-physics goals and overall approach to triggering. It has taken a year to fine-tune the specifications of the BVX chip, and some topics are still not completely resolved. For example, a fast out that provided trigger information was considered too difficult at this early stage, but is something that we will undoubtedly wish to consider later since a vertex trigger would be extremely useful to a B-physics experiment.

The R&D program has begun to test hardware solutions to subsets of the full specifications via so-called tiny chips, submitted to the MOSIS VLSI-chip facility. A short summary of this work is presented following a list of the BVX specifications.

5.2.1 BVX Specifications

We list the technical specifications of the BVX for the interested reader. No attempt is made to put them in the context of existing chips, but in general the parameters are slightly beyond those achieved in existing chips while being within reach of new efforts, especially as silicon technologies with smaller feature sizes become available. A simplified BVX block diagram is given in Fig. 19.

1. Detectors will be double-sided AC coupled. For a switched-capacitor circuit this implies double-correlated sampling to correct for integrator charge-injection effects, offsets, and input-drift effects. Circuitry must be designed for positive and negative signals.

2. 128 channels/chip including an amplifier and digital section that run simultaneously (in contrast to the separate data-acquisition and data-readout cycles of the SVX chip).

3. Digitized signal and address outputs.

4. On-board A/D conversion with 7 bit accuracy and a conversion time of 1-2 μs.

5. A direct analog output for diagnostic purposes.

6. Input-amplifier total response and reset time of 400 ns, corresponding to a 2.5-MHz interaction rate.

7. Input-amplifier noise = 600 e_{rms} at C_{in} = 5 pf. This is determined by a 200-μm-thick fully depleted silicon detector and a signal of 5000 electrons per strip from a 55°-angle-of-incidence track.

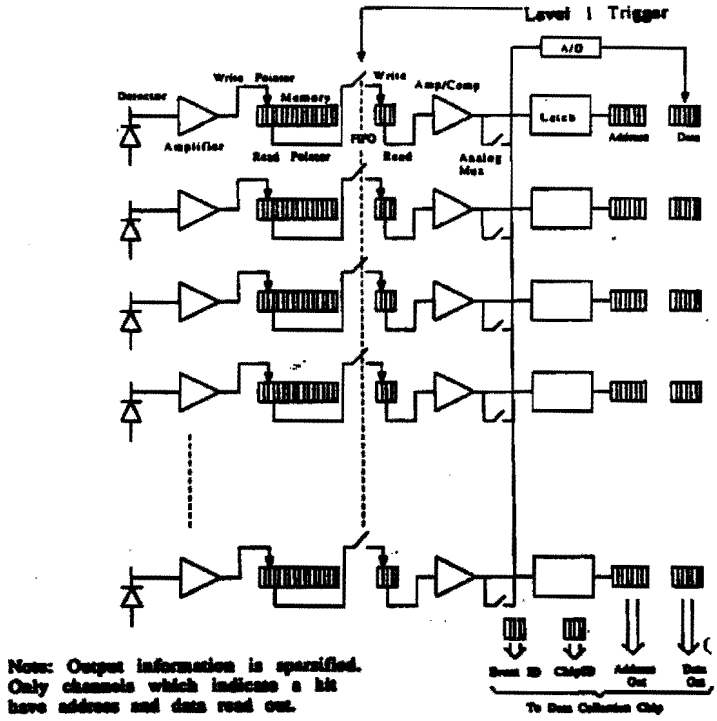

Figure 19: A block diagram of the BVX readout chip. There are 3 stages: amplification, storage, and digitization/sparsification. Digitization takes place only after a Level-1 trigger accept.

8. On-board 16-bucket analog memory for each of 128 channels. This gives 6.4 μs of delay to allow for the Level-1 trigger-decision time.

9. 4-bit Level-1-trigger FIFO to store information after the Level-1-trigger accept. This allows for simultaneous data-readout and data-acquisition cycles and provides time for the on-board digitization. Data reduction from analog memory to the FIFO is about 50:1.

10. An event number via a 4-bit counter that gets bumped with each Level-1 accept.

11. Events are not necessarily read out in order. They will be assembled downstream of the BVX.

12. One discriminator per channel, with a common threshold for 128 channels and one calibration input for the 128 channels.

13. Data sparsification of the digital outputs, with the option of reading all channels for debugging.

14. Must be able to daisy chain analog and digital outputs from up to 10 chips.

15. Option to suppress the readout of a chip if there are more than 10-20 hits on the chip. We expect typically 1-2 hits/chip per event.

16. Option to gate off unwanted channels.

17. Design for 1-2 mW power consumption per channel.

18. The chip should withstand about 100 krads/year of radiation.

19. Assume the input capacitance is a maximum of about 5pf and the amplifier pitch is less than 50μm.

5.2.2 Summary of Progress

The BVX readout R&D effort encompasses four topics: preamplifier design, A/D design, the study of simultaneous analog and digital operation, and radiation hardness. We discuss the status of each topic briefly as was outlined by R. Yarema at the BCD collaboration meeting, 9/14/90, at Fermilab.

Preamplifier Design

The amplifier design has been done in collaboration with C. Britton of ORNL. Two devices have been designed, fabricated and tested. One was a preamplifier (called IIA) and one was a preamplifier/shaper. There is a new preamplifier designed and presently in layout, and a new preamplifier/shaper in layout, both due to be submitted in November. The MOSIS facility was used and the test chips were fabricated in a 2-μm CMOS process.

A real-time-feedback amplifier design, similar to the CERN AMPLEX, was chosen for IIA. This design contrasts with the switched-capacitor technique used in the SVX chip. A circuit diagram of the IIA preamp/shaper is given in Fig. 20.

Three input-transistor W/L designs were studied: 1000/2, 1500/2, and 2000/2, all on a 45-μm pitch, with channel lengths 4700μm, 4830μm, and 5060μm, respectively. The shaper lengths were all the same, namely 2014 μm. The calculated and measured performance of preamplifier IIA with a total shaping time of 450 ns are listed in Table 6. The shaper was external to the circuit and the noise is shown for two input capacitances.

Table 6: Noise performance of the BVX IIA preamp.

Input	Noise Equivalent	
Capacitance	Calculated	Measured
5 pf	301 e	510 e
16.5 pf	582 e	910 e

These numbers are very encouraging for the first design pass and indicate that the noise goals are probably achievable. The estimated power dissipation for the IIA preamplifier and shaper is 1.2 mW.

The IIIA design has only a slight change to the preamp, but we added a second stage to the shaping to provide higher gain for the A/D. The main problem at this point is a $\pm$2-fC

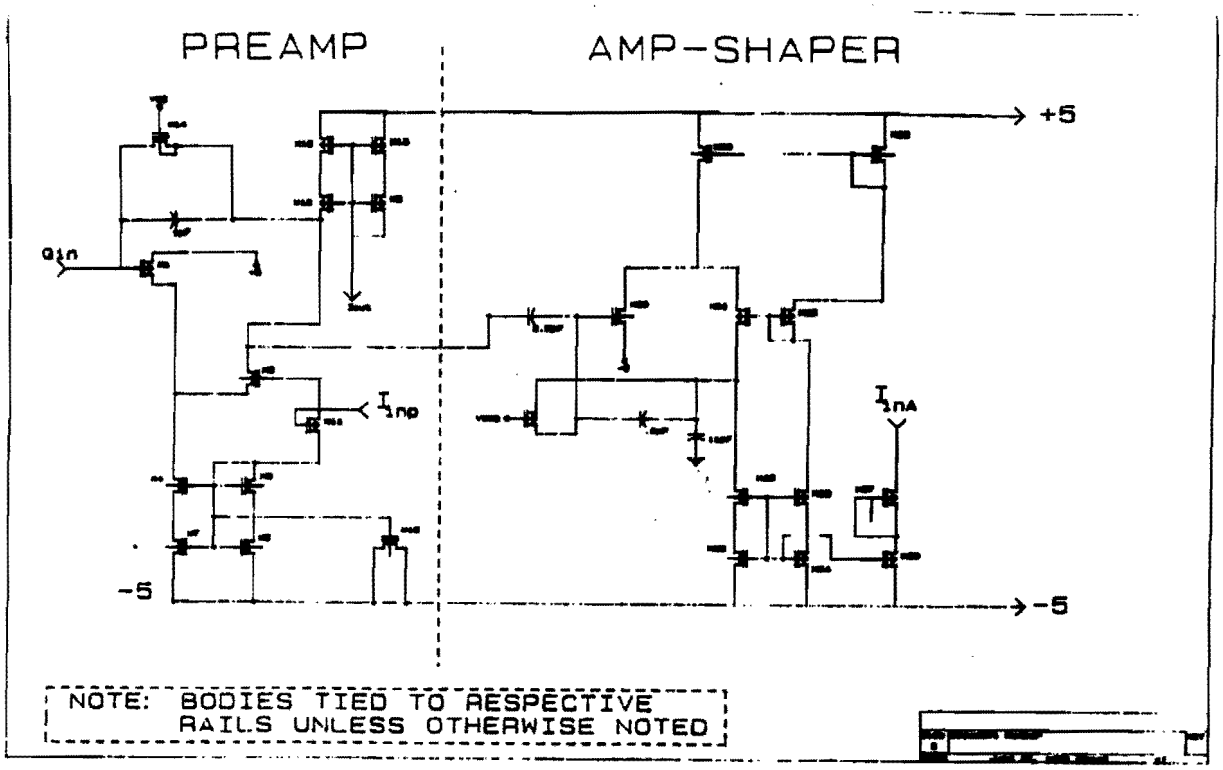

Figure 20: The BVX IIA test preamplifier and shaper circuit.

DC offset at the shaper output which can lead to higher noise. This problem is being studied. Another problem is the physical size of the chip, which will be reduced somewhat with a smaller-feature-size process, but most of that reduction comes from the digital section. In addition, as is well known by the experts, fabrication of a high-value feedback resistor is difficult.

As a comparison, the SVX-H preamplifier, fabricated in a 1.2-μm radiation-soft process, was tested. The preamp is of the switched-capacitor type, the input W/L was 500/3 μm, and it operated with a gain of 26 mV/fC. In the double-correlated-sampling mode, and with a partial reset (which we do not describe), the noise figures are presented in Table 7.

Table 7: Noise performance of the SVX-H preamp.

Input Capacitance	Noise (e)	Shaping Time (ns)
5 pf	700	340
10 pf	1000	360
30 pf	2000	480

A full reset (if the integrator needs resetting) gives about the same noise figures but roughly doubles the shaping times. For reference, the present SVX-D (quad-correlated sam-

pling) with 30-pf input capacitance has a noise figure of 2100 electrons.

We are considering a mixed-mode approach, where the first stage of the preamplifier contains a feedback resistor, and subsequent stages of shaping use the switched-capacitor approach. This may solve the DC-offset problem of the feedback-preamp design mentioned earlier.

A/D Convertor

It became clear early in our considerations that a single A/D per channel would be necessary if high data rates were to be achieved. We have designed, laid out, and submitted for fabrication an 8-bit Wilkinson ADC. The device has 7-bit accuracy, with the 8th bit being used for data sparsification. It has been laid out on a 45-μm pitch using 2-μm technology. Eventually a 1.2-μm feature size will be used, and the chip will run faster and be smaller in size. A block diagram of the ADC is presented in Fig. 21.

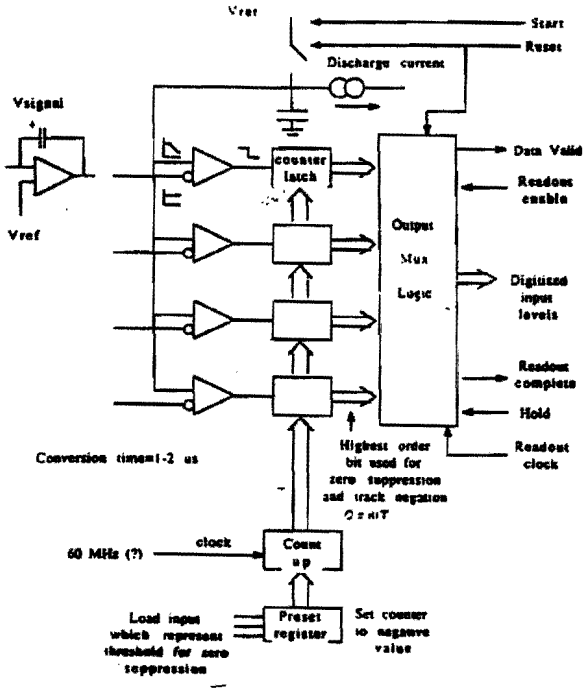

Figure 21: A block diagram of the Wilkinson ADC and data readout.

The expected power consumption is 300 μW. The conversion time for 7-bit accuracy is 2.56 μs, (full-scale σ) using a 25-MHz clock. The readout time is very fast, typically 240 ns for 8 channels. The test chip is expected within a couple of weeks.

Simultaneous Analog and Digital Operation

A test stand to explore simultaneous analog and digital operation has been built. The bonding wires have been shown to cause significant coupling from output to input. An output-to-input capacitance (stray capacitance) of 0.1 ff causes a 0.5-fC input for a 5-volt logic swing.

A test chip was built that included an isolation barrier. The chip contains two ring counters and preamplifier. The amplifier output was studied and the evidence of noise is shown in Fig. 22 as well as the effect of the isolation. Study of this problem is continuing.

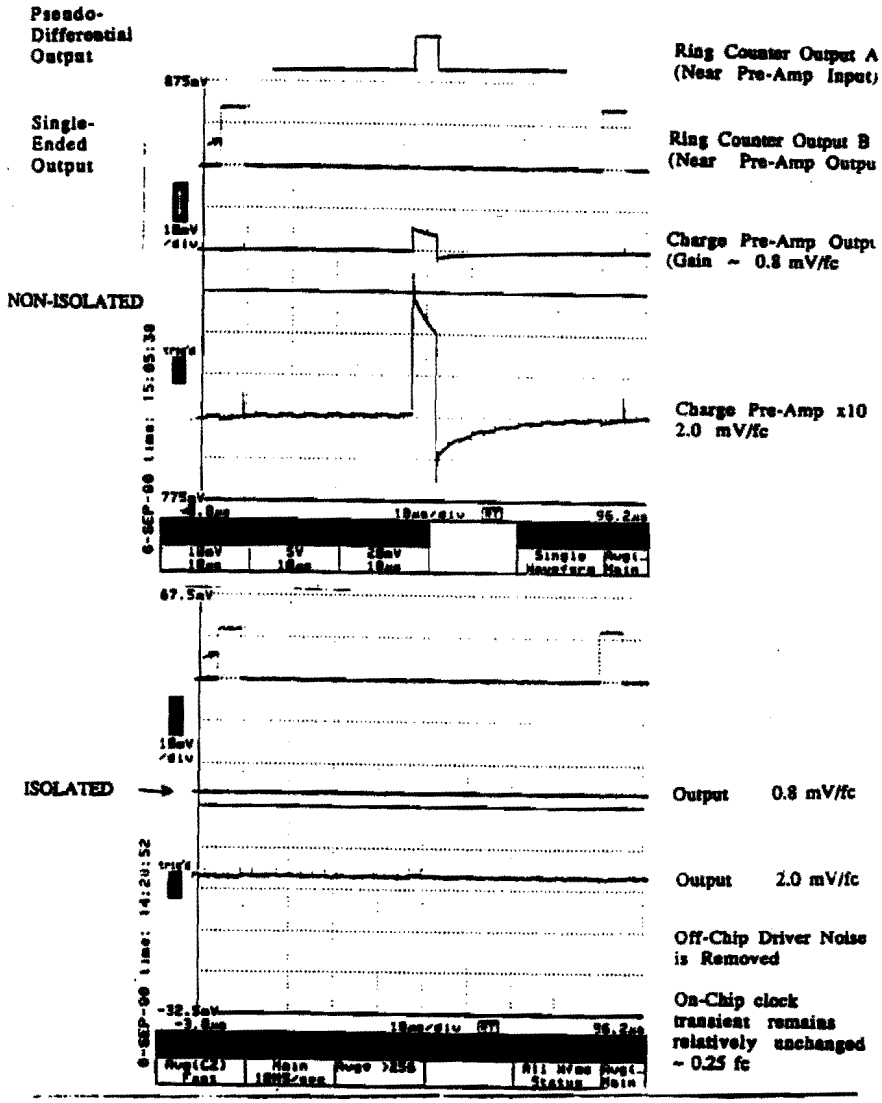

Figure 22: Scope display of noise pickup in simultaneous analog/digital operation. The ring counter can be seen as noise at the preamplifier output. The isolation eliminates this problem.

Radiation Hardness

A nondisclosure agreement with UTMC for fabricating radiation-hard devices has been made by Fermilab. The design rules are in-house for the 1.2-μm process. This work is just beginning and we expect to collaborate with other high-energy-physics institutions that are also just starting to work with UTMC.

5.3 Beam Tests of Silicon Strip Detectors

We have recently completed the first portion of a test program on silicon microstrip detectors with VLSI readout in the M-Test beam. We operated single- and doubled-sided AC-coupled detectors from two manufacturers, SI (Oslo) and MBB (Munich). All detectors were instrumented with the Berkeley SVX version D silicon-strip-readout chip. These chips were interfaced using the Berkeley SRS fast-sequencer and SDA flash-ADC modules. Measurements were made of the signal-to-noise and spatial resolution for tracks at normal and non-normal angle of incidence. Results have been reported at the London Conference on Position Sensitive Detectors and additional results will be reported at the SSC Detector Symposium in Fort Worth and at the IEEE Nuclear Science Symposium.[42]

The silicon strip detectors were mounted in the fixture sketched in Fig. 23, which could orient them at various angles to the beam. Some preliminary conclusions can be drawn from the data collected. Figure 24 shows the pulse height spectra of hits in two adjacent strips for pedestal events, and for events in which a beam particle passed through the detector (but not necessarily the two strips displayed). The noise is gaussian over several decades, and has an r.m.s. value of 4 ADC counts. Figure 25 shows the pulse-height spectrum of clusters of hits from single minimum-ionizing particles after pedestal subtraction. The signal-to-noise is about 10:1. Figure 26 shows the residuals between hits in the test detector and a track defined by three other silicon strip detectors. The inferred spatial resolution for a single detector is 10 μm.

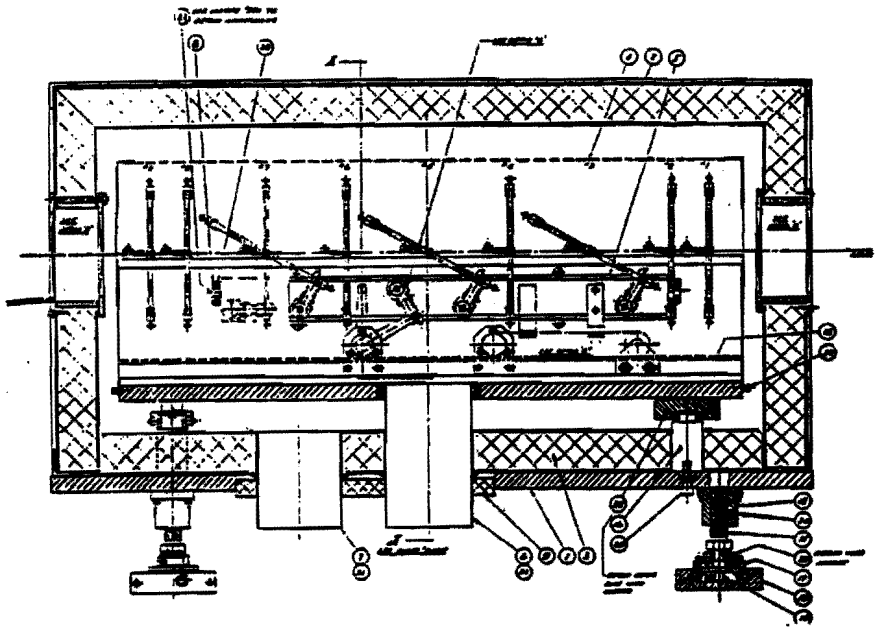

Figure 23: The mounting fixture for silicon-strip-detectors in the M-Test beamline. Three of the detectors could be rotated so the beam was at non-normal incidence.

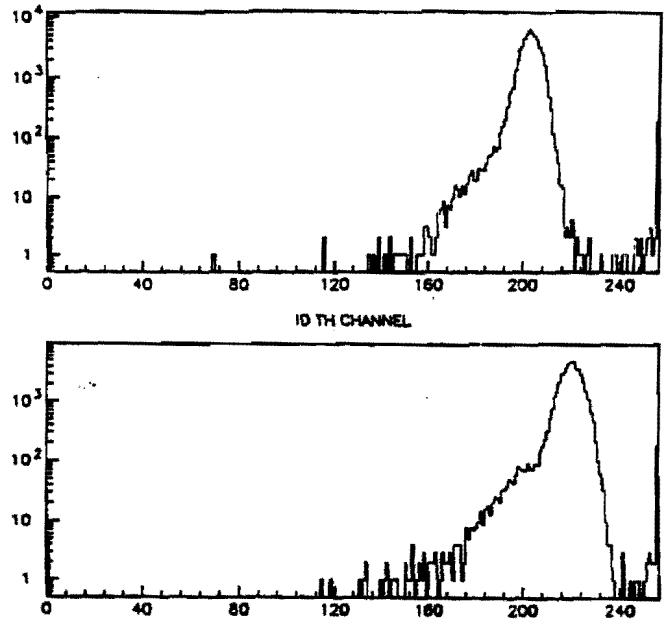

Figure 24: Raw pulse-height spectra summed over two adjacent strips in a silicon detector. The SVX readout chip has negative gain. **Top**; pedestal events. **Bottom**; events with beam particles in the detector, but not necessarily in the two strips displayed.

5.4 Beam Tests of a Silicon Pixel Detector

A 256 × 256 silicon pixel detector[18, 43] was also tested in the M-Test beamline. This device is sketched in Fig. 27. The PMOS VLSI readout circuit is indium-bump-bonded to the detector diode array, permitting different silicon-process technologies for the two components of the detector. Detectors of this type have been previously produced for their sensitivity to infrared radiation, and operated at L-N_2 temperatures. The devices tested at Fermilab had an improved noise performance that permitted operation at room temperature. However, the readout cycle was still 16 msec, as for the earlier infrared devices.

The pixel device was placed in the 227-GeV pion beam and data collected during two shifts. Because of the 60-Hz readout cycle of the detector, each recorded frame was the integral of all particles that struck it in the previous 16 msec. The beam intensity was reduced until only a few tracks appeared in a frame. Figure 28 shows a frame thus recorded with 10 particles in the detector. The signal-to-noise for minimum-ionizing particles is excellent ($\sim$ 50:1), as is the two-track resolution. Figure 29 shows a blowup of an event in which a nuclear fragment travelled a few-hundred μm in the detector after being ejected by a beam pion.

The key result of the beam test was the demonstration of good signal-to-noise at room temperature. As the readout speed increases in future versions, pixel detectors will clearly play an important role at hadron colliders.

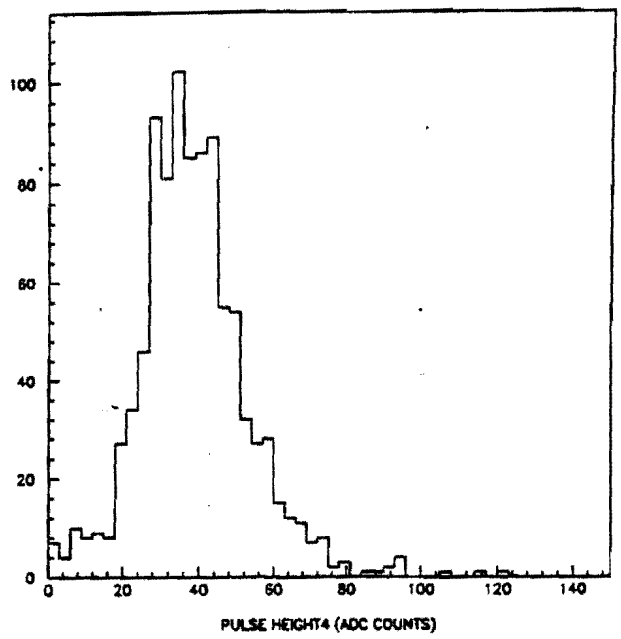

Figure 25: The pulse-height spectrum of minimum-ionizing particles in a silicon detector, obtained by summing of a cluster of strips. Pedestals have been subtracted.

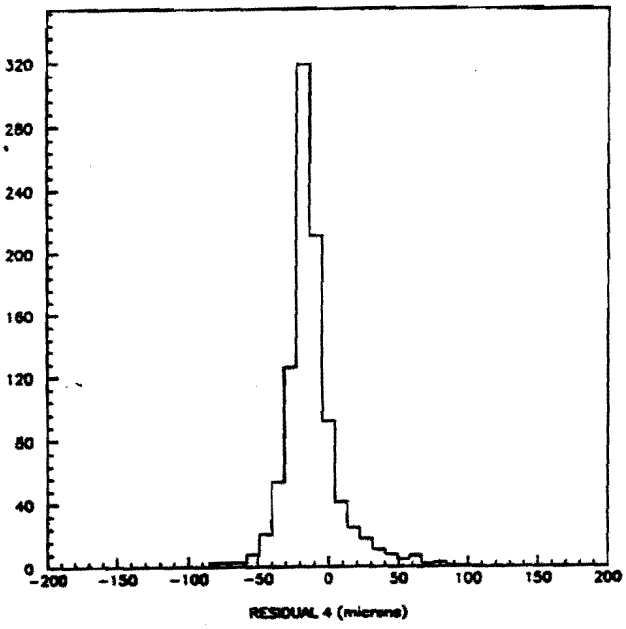

Figure 26: The distribution of residuals between hits in the test silicon detector and a track defined by hits in three other detector planes.

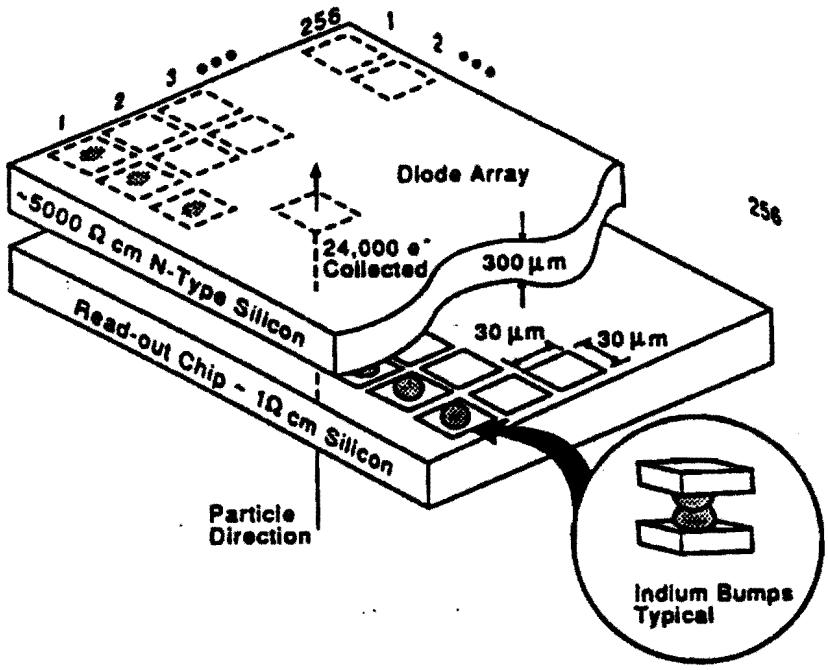

Figure 27: Schematic representation of a silicon p-i-n diode hybrid detector.

5.5 Simulation of Vertex-Detector Performance

Monte Carlo simulations of the BCD vertex detector were begun by P. Karchin and L. Roberts,[44] continued by K. McDonald,[22] and extended by P. Lebrun.[45] We summarize here some of the advances of the latter work, which is still in progress.

In the recent simulations a full analysis program for tracking and vertexing in the silicon detector has been written. It is presented with fake data from a Monte Carlo simulation in the form of ADC counts in and addresses of struck detector elements. This very considerable effort is perhaps unique in that the BCD has its primary analysis program written before the experiment is approved!

Features of the simulation are listed below. Advances over previous work are noted.

1. Events containing B-$\bar{B}$ jets are generated using ISAJET and transmitted to GEANT for detector simulation. Multiple-scattering effects are included in the track propagation. The simulation includes a uniform, transverse magnetic field of 10 kG, as specified for the full BCD experiment. This is the first of our simulations to include a magnetic field.

2. The model silicon detector, sketched in Figs. 13-15, contains some 1.2×10^6 silicon strips.

3. Figure 30 shows the multiplicity distributions of all particles, charged particles, and

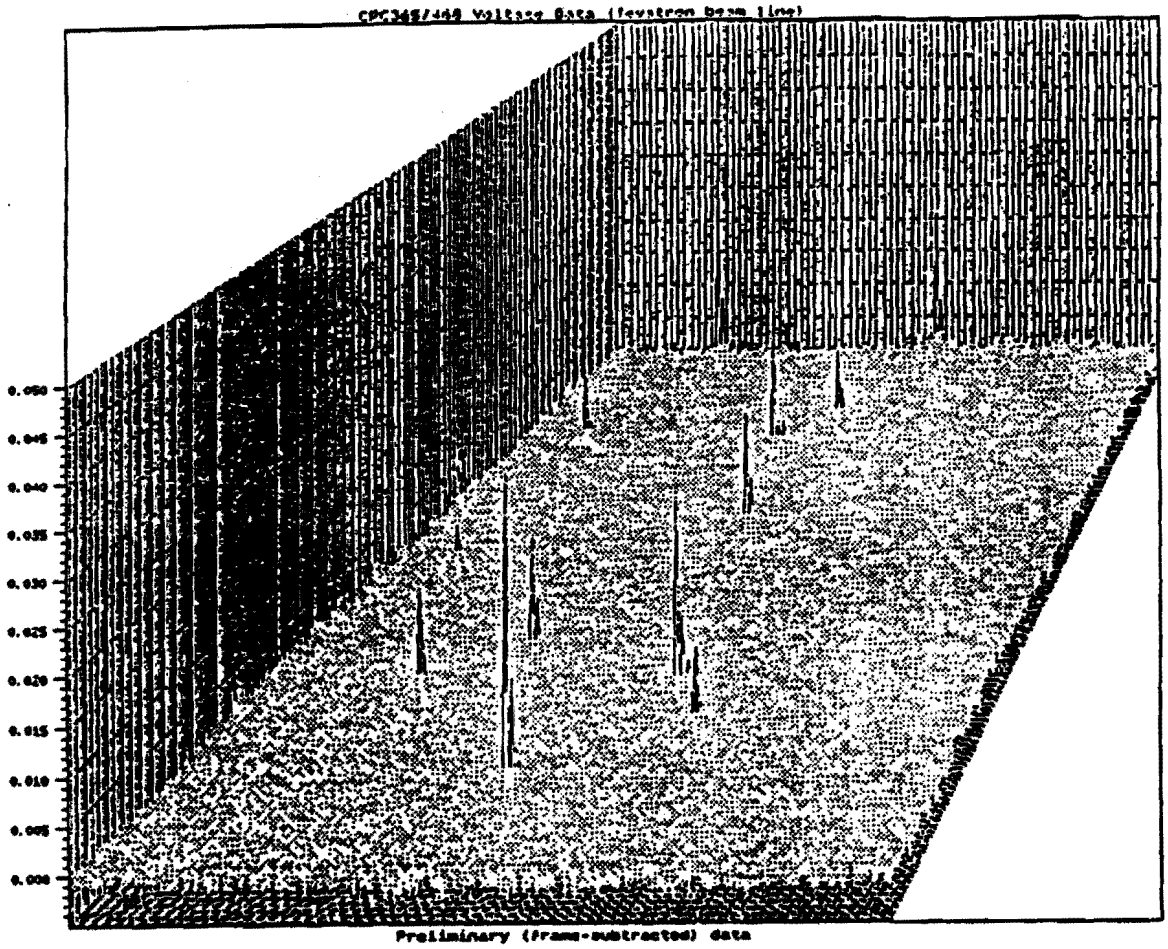

Figure 28: A three-dimensional plot of minimum-ionizing particles in a silicon pixel detector. The vertical axis is the pulse height.

number of struck strips in the vertex detector for the simulated events.

4. The response of each silicon detector to passing charged particles is modelled, including Landau fluctuations in the deposited energy, charge sharing among adjacent strips, and noise in the readout amplifiers. The signal (plus noise) charge is analyzed in a 7-bit ADC, and the ADC counts in each silicon detector channel are written to tape, simulating a raw-data file.

5. Track pattern recognition is performed using a hypothesis as to a track road as would be provided in an outer straw-tube tracking system. Simulated noise counts, and multiple tracks crossing a single detector strip lead to confusion in the pattern recognition, as illustrated in Fig. 31.

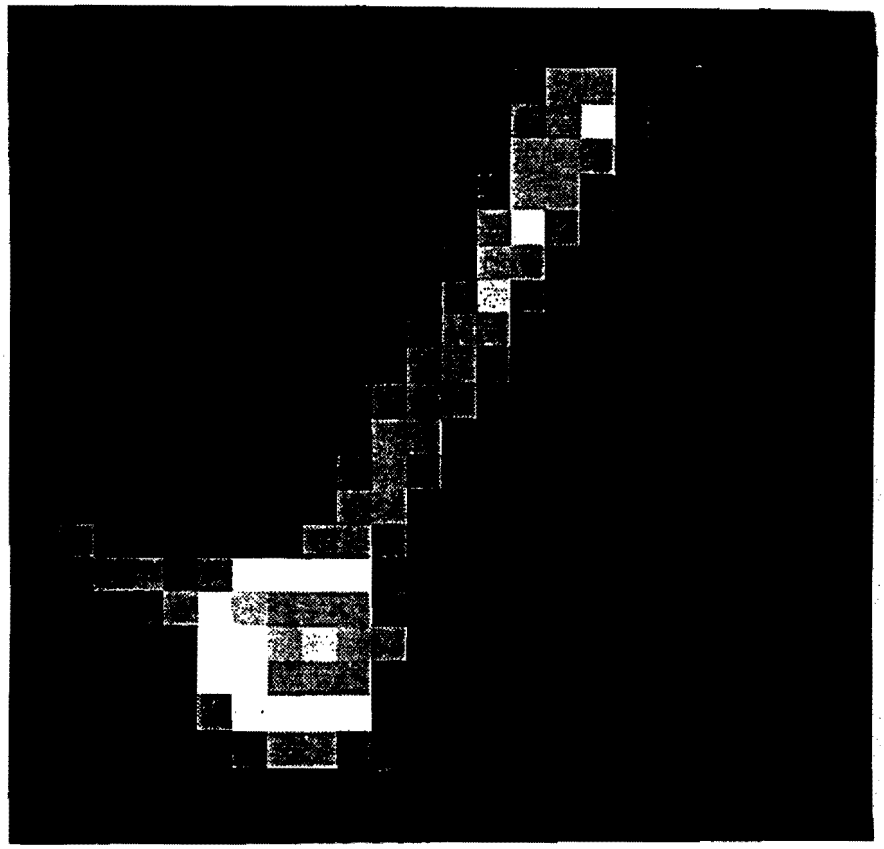

Figure 29: Blowup of a region of an event in the pixel detector showing nuclear fragmentation.

6. The raw strip pulse heights are searched for clusters, corresponding to single-particle tracks. A hit must be above a pulse-height threshold before it is included in the cluster analysis. In a 4π-solid-angle geometry many particles cross the silicon detectors at large angles of incidence, leading to large clusters as sketched in Fig. 32. The summed ADC counts over strips in clusters in disk detectors is shown in Fig. 33.

7. The hit clusters on different silicon detectors are then searched for tracks. Roads are taken from an assumption of track finding in an outer tracking detector not simulated here. In the presence of a nonzero magnetic field the track roads are helical. Figure 34 shows the multiplicity distribution of hit clusters used on the reconstructed tracks.

8. When two hit clusters in a silicon detector are within 3σ of one another in one coordinate, where σ is the r.m.s. cluster width, they are said to be confused.

   Figure 35 shows the confusion probability as a function of strip length for barrel detectors. If the confusion probability is desired to be at most 1%, the strips must be no longer than 1 cm, which leads to a large channel count for the whole detector.

9. Once the tracks have been found, and the errors on the fitted trajectories evaluated, vertex finding is begun. The primary vertex is found first, and tracks with poor fits to

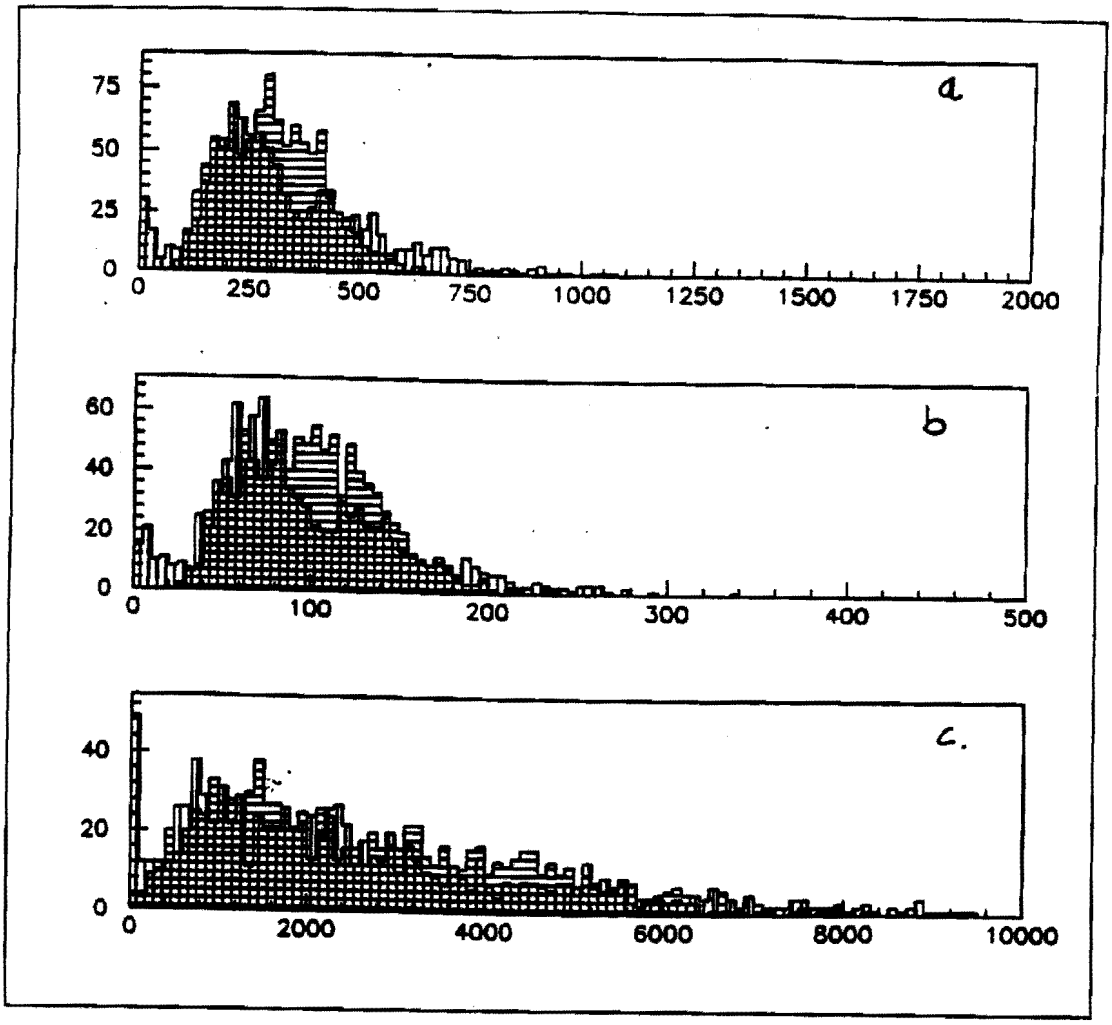

Figure 30: Multiplicity distributions for a): all particles, b): charged particles, and c): struck silicon strips in the simulated events.

this vertex are searched for secondary vertices. The invariant-mass distribution of the tracks to secondary vertices can then be examined for B-mesons decays, *etc.*

All algorithms needed for this have been written and appear to be working. However, the results are too preliminary to justify making firm conclusions are the detector performance at this time.

From these studies we will soon have rather realistic estimates of track and vertex finding in the silicon vertex detector in the presence of electronic noise and signals from large numbers of tracks. From this one can extrapolate the signal-to-background ratio in measurements of various B-decay modes, estimate the accuracy on proper-time measurements, *etc.* A question of importance for the μBCD (and also to upgrades of CDF and D0) is how well does the silicon vertex detector perform as a standalone tracker?

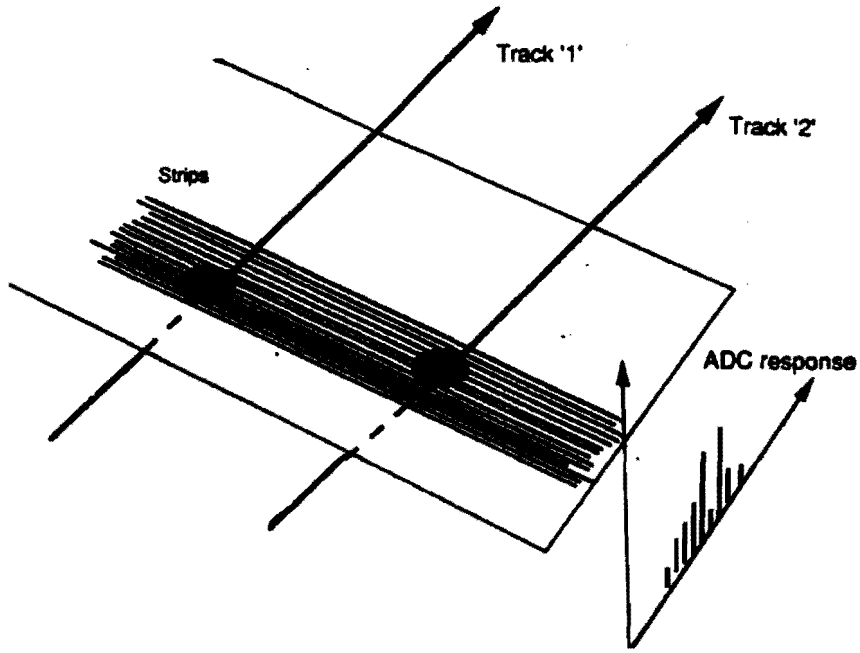

Figure 31: Confusion due to multiple hits in a silicon detector arises when two tracks pass through the same, or closely adjacent, strips.

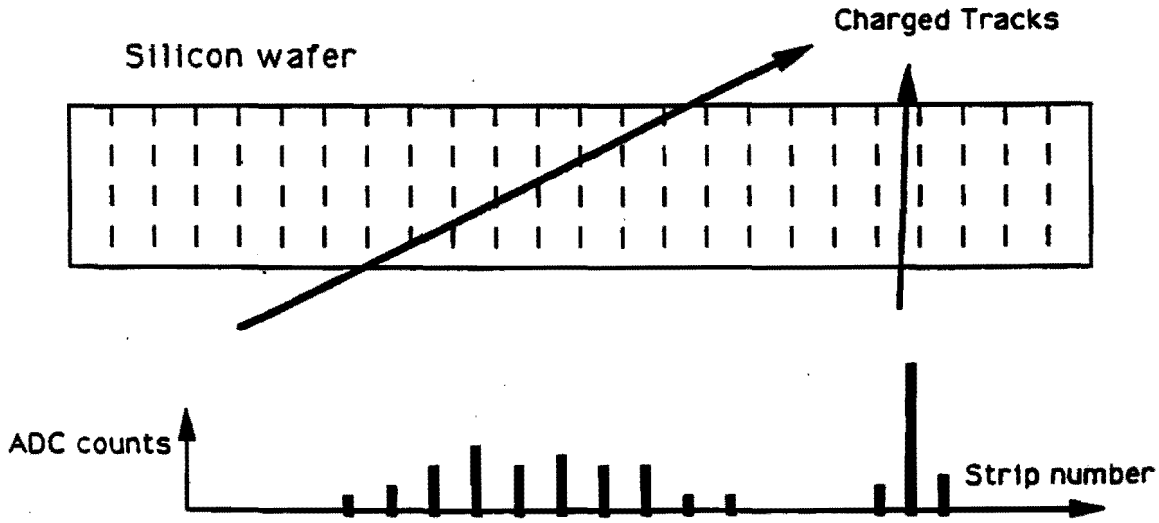

Figure 32: Hit clusters from tracks in a silicon detector. Tracks with large angles of incidence lead to extensive clusters with small pulse height in each strip.

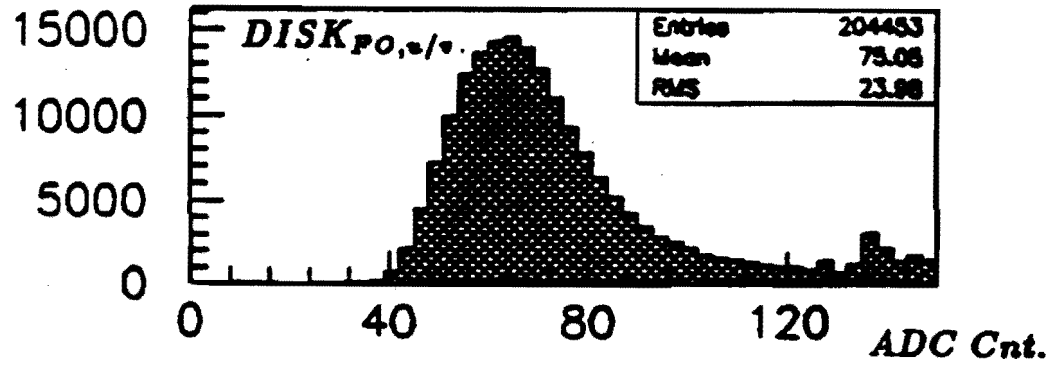

Figure 33: The pulse-height spectrum for hit clusters in silicon disk detectors.

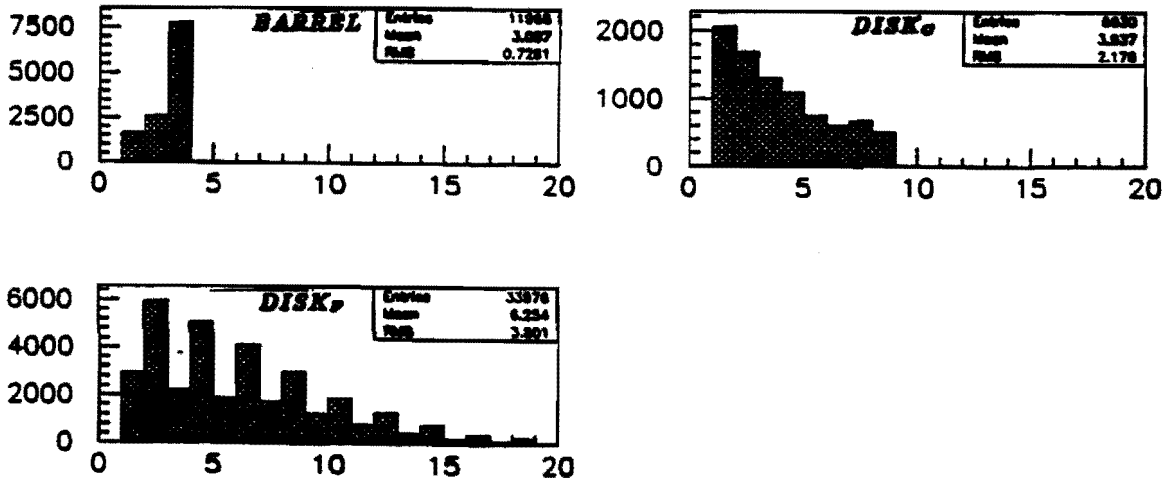

Figure 34: Multiplicity of hits per reconstructed track in the silicon vertex detector.

6 Appendix B: Straw-Tube Tracking

The desire for extreme compactness in the μBCD experiment has led to the use of the silicon vertex detector as a tracker as well, at some compromise in momentum resolution and pattern recognition. In B-physics experiments with more available space a conventional tracking system will be an important complement to the silicon vertex detector. Recent work on future tracking systems has explored the use of straw-tubes because of their low mass and high resolution.

C. Lu and K. McDonald of Princeton have been involved in hardware R&D on straw-tube systems, and M. Lundin and L. Stutte of Fermilab have pursued simulations of system

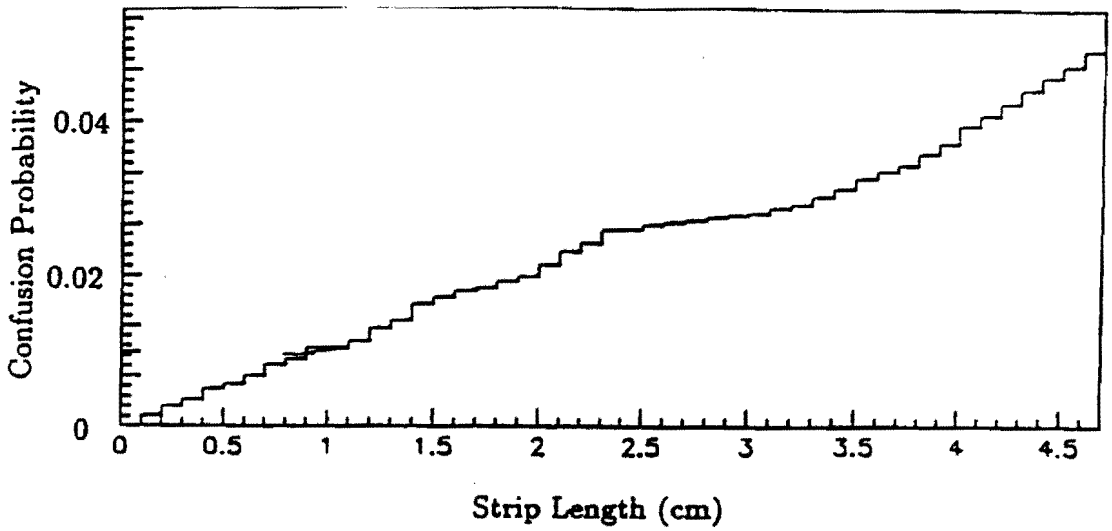

Figure 35: Hit-confusion probability in the barrel detectors as a function of silicon strip length.

performance. Preliminary reports of this work have been presented at the Workshop on Major SSC Detectors (Tucson, Feb. 19-23, 1990),[46] at the IISSC Industrial Symposium (Miami, Mar. 14-16, 1990),[47] and at the International Conference on Advanced Technology and Particle Physics (Como, Italy, June 11-15, 1990),[48] and in considerable detail in the Renewal Proposal to the SSC Subsystem R&D program.[49]

A brief summary of the work accomplished in FY90 follows:

1. Purchase of 3000 sets of Ultem feedthroughs, brass taper pins, and aluminum collars for 7-mm-diameter straws, according to designs from an Ohio State U. group.[50]
2. Winding of 4 sets of straw tubes ($\sim$ 1500 total) by Stone Industrial for prototype tests.
3. Purchase of Makrofol conducting polycarbonate foil, 0.5-mil thick. An attempt to copperize this failed. It can be aluminized to about 1 ohm per square by Sheldahl – this is the standard cathode material in use.
4. Purchase of conducting Kapton foil, 0.85-mil thick. Kapton can be copperized. 0.5-mil thickness is available, but with a $\sim$ \$200k minimum order.
5. Purchase of a spiral winding machine for the manufacture of straw tubes. However, no straws have yet been wound by us.
6. Construction of a clean 'shack' for assembly of straw tubes. This 10′ × 16′ workspace achieves Class 1000 with no people present.
7. Purchase of a 2-m-long granite straight edge for precision alignment of straws during assembly.
8. Purchase of a set of 25 mandrels that can be inserted into straws during glueing.
9. Purchase of a N_2-driven glueing apparatus.

10. Assembly of a 21-tube prototype (along with M. Convery and D. Marlow of Princeton U.), using the mandrels and glueing apparatus of items 9 and 10.

11. Purchase of LeCroy electronics for this prototype (as the electronics expected to emerge from the Front-End Electronics Subsystem R&D are not yet available in sufficient quantity).

12. Construction of two kinds of wire-tension monitors. Results from these have pointed towards an improvement in the OSU scheme for tensioning the wire in the straws.

13. Pressure tests of straws, showing that the straws can hold 10 atmospheres.

14. Creep tests of straws, showing that a 2-m-long straw subject to a 1-lb weight stretches about 10 mils over a 2-month period. The straws also show expansion and contracting of about 10 mils during temperature shifts of 10°F (as expected from the known thermal-expansion coefficient).

15. Demonstration that straws could be pressurized during assembly, as an alternative to the use of mandrel inserts.

16. Design of an assembly fixture for 8-layer superlayers using grooved vacuum pads.

17. Design of a coaxial straw end-plug that incorporates gas and high voltage distribution, signal transmission, and wire tensioning. Custom high-voltage capacitors have been obtained for this.

18. Study of the wire instability in long straws, showing the effect of a wire offset, and of deformations in the straw.

19. Construction of several prototype straws for studies of gas gain and drift timing. Some modules can be pressurized.

20. Development of a technique using a 0.3-ns N_2 laser pulse to eject single electrons from the cathode wall of a straw.

21. Characterization of gas gain as a function of temperature, pressure, and applied voltage for several gas mixtures. Comparisons are made using both a Fe^{55} source and the N_2 laser; differences allow quantitative deductions about electron attachment. The gain spectra for single-electron avalanches are measured.

22. Measurements of timing (and hence spatial) resolution for single electrons, using the N_2-laser technique. The best performance observed (at 1 atmosphere) is 50-μm resolution in Ar/CO_2 (50/50) and CF_4/Isobutane (85/15) mixtures.

23. Comparison of amplifier performance between the LeCroy TR402 amplifier and the U. Penn straw-tube amplifier. The latter is measured to have about 1300-electron equivalent noise (15 times better than LeCroy), while contributing less than 0.5 ns to the timing uncertainty.

24. Development of a model of straw-tube response including characterization of the avalanche, electrical performance of the tube, and of the amplifier. This permits extrapolations of measurements with the N_2 laser to wider regimes.

25. Construction of a precision gas-mixing system, with control of both flow and pressure.

26. Initial development of a gas-analysis capability based on gas chromatography.

27. Simulation of overall system performance in the TEV I environment.

We now present details on the three of the topics just listed.

6.1 Studies of Single-Electron Avalanches with a N_2 Laser

6.1.1 Experimental Set-up

UV light sources have been used to generate photoelectrons from photosensitive plates for time-of-flight measurement of electrons in different gases.[51, 52] Also, several papers report on the use of laser-induced ionization in drift chambers to mimic the track of a minimum-ionizing particle.[53, 54, 55, 56] We have developed a technique to study single photoelectrons ejected from the wall of a straw-tube chamber by a N_2 laser. Measurements of the drift time and of avalanche size have been made.

A sketch of the experimental set-up is shown in Fig. 36. The test chamber permits both a laser beam and an Fe^{55} source to generate primary electrons.

The N_2 laser generates pulsed 337-nm (3.67-eV) UV photons, with a pulse length of about 350 ps. The pulse energy is about 50 μJ, corresponding to about 10^{14} photons. The test drift tube was made of 7.67-mm-diameter aluminum tubing.

The photoelectric work function of aluminum is 4.08 eV, which is larger than the laser-beam energy; therefore the quantum efficiency for producing the photoelectron from the wall is expected to be very small. But due to the large number of photons per pulse we still can get enough photoelectrons. We are most interested in single-photoelectron events, so we use an iris diaphragm to reduce the beam intensity.

The laser beam was focused onto the inner wall of aluminum tube after passing through a 1-mm-diameter hole in the wall. The hole is offset by 1 mm from the center line of the tube. Because the beam spot on the inner surface of the tube is quite small, we can neglect mechanical imperfections and consider that the drift distance of the photoelectrons was just the radius of the tube. A beam splitter was used to reflect part of the laser beam to a photodiode (RCA C30905E), which generates a fast, large electric pulse as a start signal for the TDC system. A preamplifier was directly connected to the test drift tube through a high-voltage capacitor. The drift-tube signal was used as a stop signal.

Two different preamplifiers have been used in our measurements: a LeCroy TRA402 and U. Penn/AT&T preamplifier. The U. Penn preamplifier was used for studying the performance of CF_4/Ar and CF_4/isobutane mixtures with different mixing ratios. The other gas mixtures were measured by the LeCroy preamplifier.

The sensitivity and noise performance of these two preamplifiers have been measured, as shown in Fig. 37. The sensitivity measurement was carried out by charging a small capacitor with an EG&G ORTEC 419 precision pulser. After this known charge was amplified by the

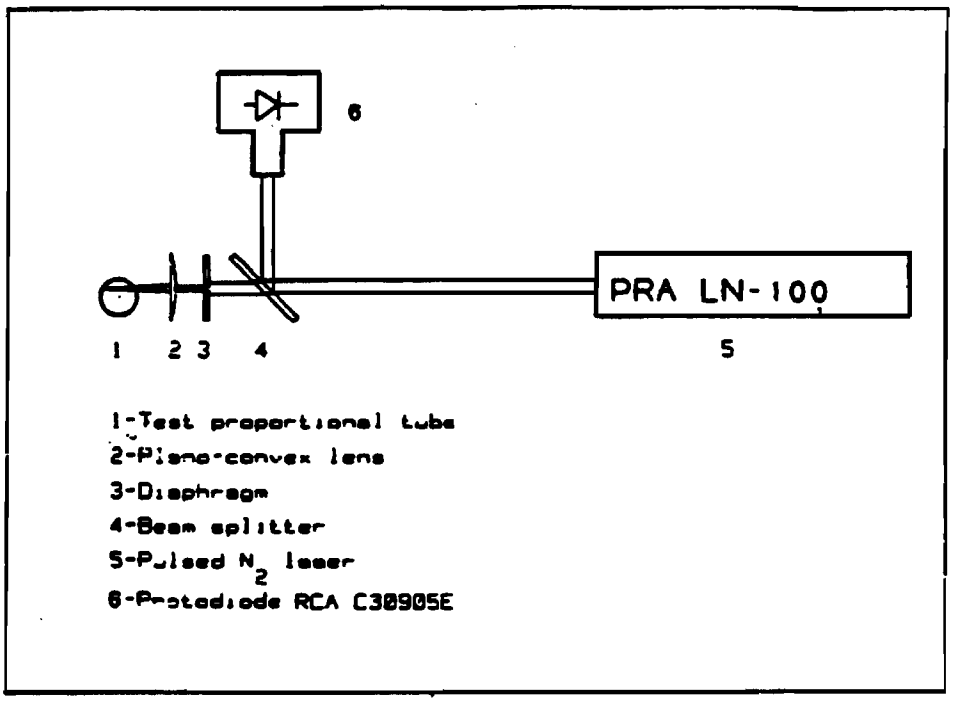

Figure 36: Sketch of the experimental set-up.

preamplifier, we measured the amplitude of the output signal on a HP 54502A digital oscilloscope. The noise *vs.* input capacitance was measured by attaching various BNC connectors (regarded here as capacitors) to the input of the preamplifier and reading the V_{rms} value on the digital scope. The capacitances of these BNC connectors were then measured with a HP 4815A RF vector impedance meter at 100-MHz frequency.

Under our experimental conditions the U. Penn preamplifier appears to be 5 times more sensitive than the LeCroy TRA402. The typical E.N.C. (equivalent noise charge) at 10-pF input capacitance is about 1600 electrons for the U. Penn preamplifier, and 17000 electrons for the LeCroy TRA402. When a 2-meter-long, well-shielded straw tube (7 mm in diameter, 25-μm anode wire) was attached to the U. Penn preamplifier, the E.N.C. was about 2000 electrons.

The threshold of the discriminator following the preamplifier was set at 30 mV (into 50 ohms), so the gas gain of a single-electron avalanche had to be greater than 5×10^4 (U. Penn) and 2.6×10^5 (LeCroy TRA402), respectively.

6.1.2 Time Spectra

Several gas mixtures have been tested with this setup.

Due to the very small quantum efficiency and large number of primary UV photons, the number of photoelectrons in each pulse should vary according to a Poisson distribution. We reduced the aperture of the iris diaphragm until at most 1 in 4 laser pulses yielded any photoelectrons, and hence at least 90% of recorded events were initiated by single photoelectrons.

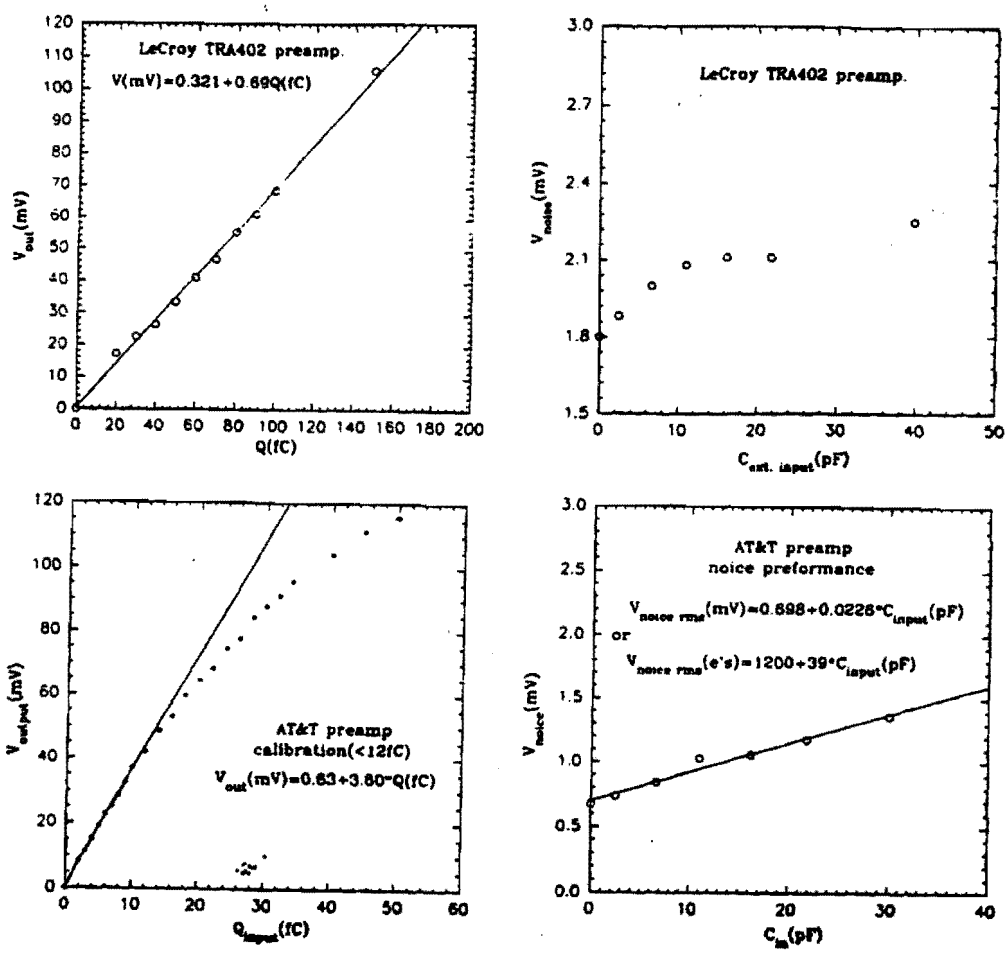

Figure 37: (a). Sensitivity and noise performance of a LeCroy TRA402 preamplifier. (b). Sensitivity and noise performance of the U. Penn/AT&T preamplifier.

Some typical single-photoelectron events are shown in Fig. 38 as recorded by a digital oscilloscope. The chamber was under constant gas pressure and high voltage for a P-10 gas mixture, but note the different time and voltage scales. The time jitter of the signal's leading edge, and the fluctuations in the gain of the gas avalanche can be clearly seen. Figure 38 also shows the after-pulses which are due to photoelectrons released from the tube's wall by the UV photons of the gas avalanche itself. The time difference between original pulses and the after-pulse is just equal to the drift time for the entire radius.

Typical measured time spectra along with Gaussian fits are shown in Fig. 39. Many other gas mixtures have been studied. The fits are very satisfactory.

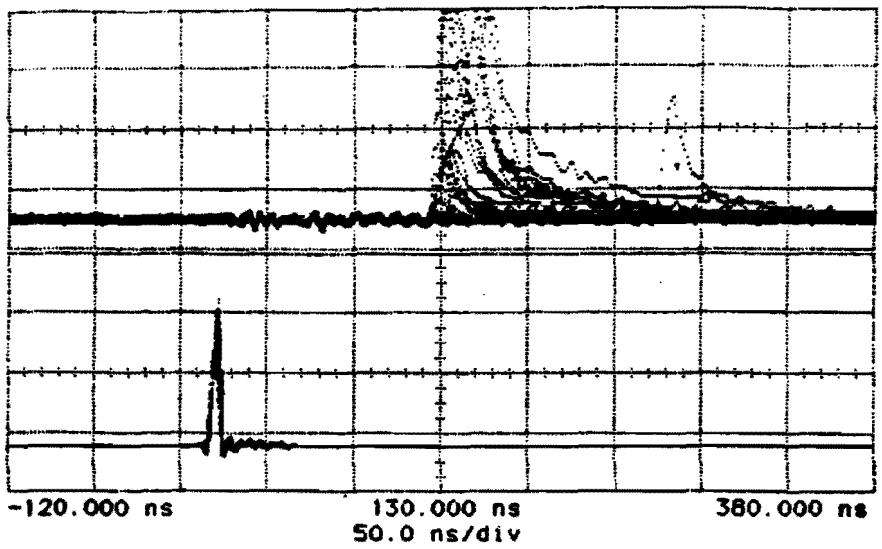

Figure 38: Photodiode and drift-tube signals for single-photoelectron events. P-10 mixture, $P = 760$ torr, $V = 1600$ V. The upper trace shows the drift-tube signals, the lower shows the photodiode signals. The vertical scale of the upper trace is 100 mV/div.

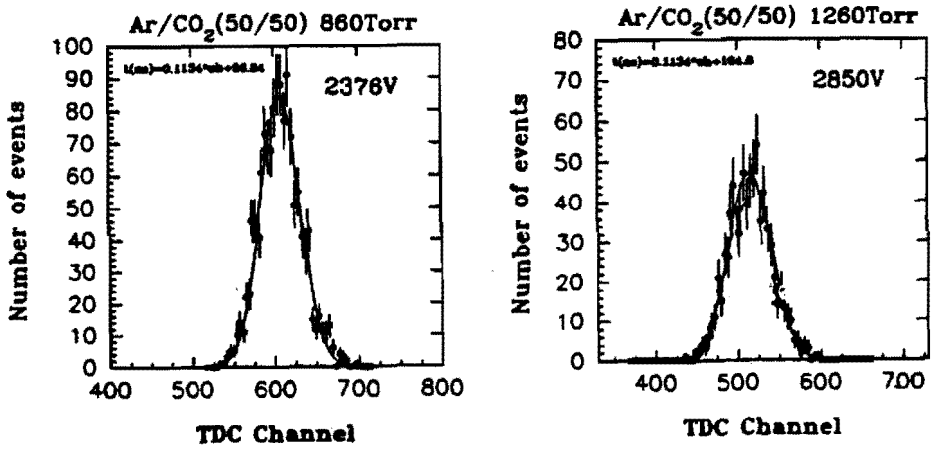

Figure 39: Drift-time spectrum for Ar/CO_2 (50/50).

6.1.3 Drift Time

Based on energy conservation, the following equation holds,[57]

$$eEw = \langle \Lambda \epsilon v / \ell_e \rangle \tag{19}$$

where E is the electric field, w is the drift velocity, ϵ is the kinetic energy, $\Lambda(\epsilon)$ is the mean fractional energy loss in a collision, v the random electron velocity, and $\ell_e(v)$ the mean free path for collision of the electron with the gas molecules. The left side represents the energy gained between collisions, and the right side is the energy lost in atomic collisions. Assuming ℓ_e is independent of v and the distribution of electron energy is narrow, and taking into account the following equations,

$$w = \frac{2}{3}\frac{eE}{m}\left\langle \frac{\ell_e(v)}{v} \right\rangle + \frac{1}{3}\frac{eE}{m}\left\langle \frac{d\ell_e(v)}{dv} \right\rangle,$$

$$\epsilon = \frac{1}{2}mv^2,$$

it follows that

$$w \simeq \sqrt{\frac{2}{3}\sqrt{\frac{1}{3}}\Lambda \frac{eE\ell_e}{m}}. \tag{20}$$

Since ℓ_e is inversely proportional to gas pressure P,

$$\ell_e = \ell_{e0}/P,$$

where ℓ_{e0} is ℓ_e at 1 atm. Therefore

$$w \simeq \sqrt{\frac{2}{3}\sqrt{\frac{1}{3}}\Lambda \frac{e\ell_{e0}}{m}}\sqrt{\frac{E}{P}}. \tag{21}$$

This is the well-known result that the drift velocity should depend only on (E/P).

Using simplified formulae to approximate the published curves on the drift velocity *vs.* E/P, we are able to calculate the total drift time. Adjusting the parameters in the formulae to get the best fit of our data, the results are shown in Fig. 40. The agreement is impressive. Because our data are collected under various pressures, and the drift velocity curves used in our fitting were measured or calculated at 1 atm, our results further confirm $w \propto f(E/P)$.

6.1.4 Spatial Resolution

From the same argument as in previous section, it follows that[57]

$$\epsilon_k = \langle \epsilon \rangle \simeq \frac{3\ell_{e0}}{\sqrt{3\Lambda}}\frac{E}{P}, \tag{22}$$

where ϵ_k denotes the characteristic energy, which is a function of E/P. The spatial resolution σ is then

$$\sigma_x = \sqrt{\frac{2\epsilon_k x}{eE}}, \tag{23}$$

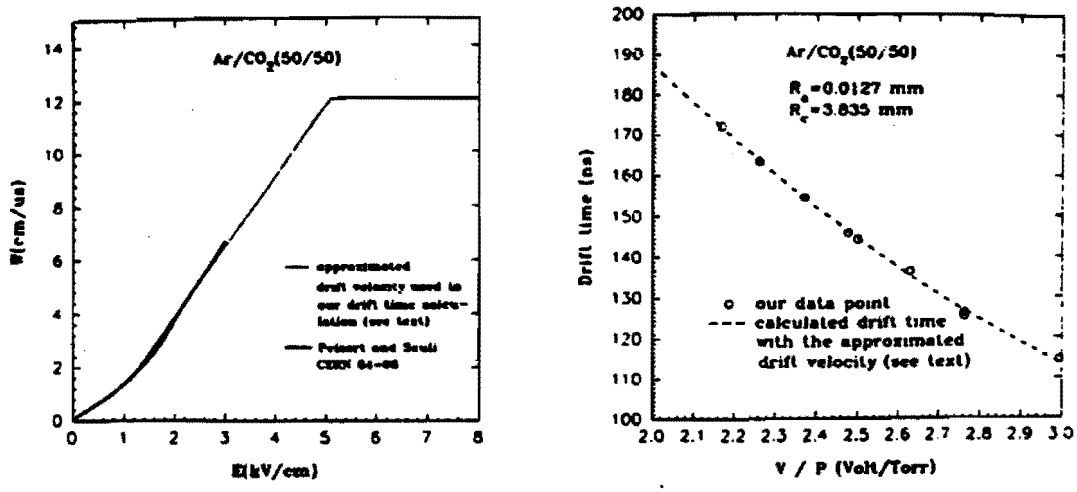

Figure 40: Drift velocity and drift time of Ar/CO_2 (50/50).

where x is the drift distance. Using (22) instead of ϵ_k in (23) we arrive at

$$\sigma_x = \sqrt{\frac{2\ell_{eo}}{\sqrt{3}\Lambda}}\sqrt{\frac{x}{P}}. \tag{24}$$

While $\Lambda(\epsilon)$ is a function of electron energy ϵ, ϵ remains at a constant value up to rather high E field for a "cool gas" such as CO_2, for which Λ remains effectively constant. In such cases we conclude from (24) that

$$\sigma_x \propto \sqrt{\frac{1}{P}}.$$

We have directly measured the value of σ_t, and converted to σ_x using the x *vs.* t curve near the tube wall. Figure 41 shows our data as well as a fit of the form

$$\sigma_x = \sigma_0 + A/\sqrt{P}$$

for Ar/CO_2.

6.1.5 Discussion of Spatial Resolution

The total drift times over the radius of our proportional tube agree well with the published data. Direct comparison with the published data of our results on spatial resolution are difficult due to very limited existing data.

Pius[58] and Jean-Marie *et al.*[59] have measured the longitudinal diffusion of electrons in Ar/C_2H_6(50/50). This diffusion can be expressed as a constant times the square root of the distance from the anode. We infer that these constants are $\sigma_{0l} \simeq 210\ \mu m/\sqrt{cm}$ from Pius and $\sigma_{0l} \simeq 125\ \mu m/\sqrt{cm}$ from Jean-Marie *et al.*Then for a 0.3835-cm drift distance the spatial resolutions should be 130 μm and 77 μm, respectively. Our result (not shown) for 760 torr is 100 μm, in reasonable agreement.

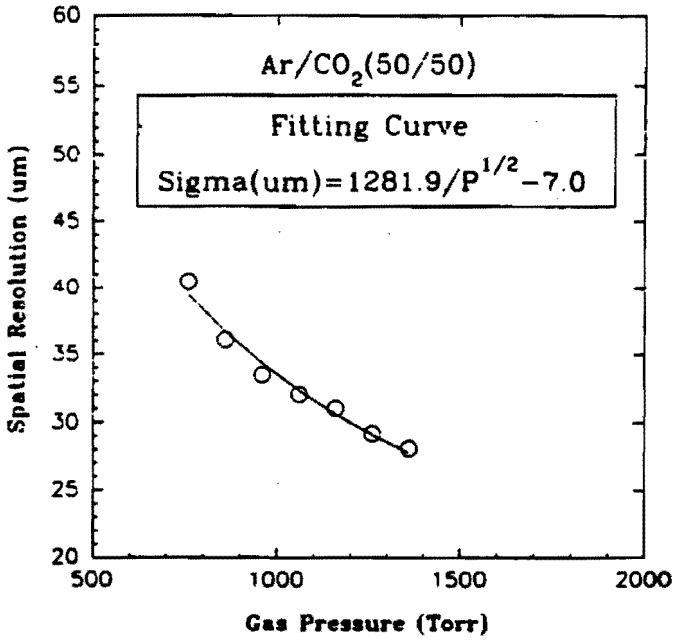

Figure 41: Spatial resolution of Ar/CO_2 (50/50).

The spatial resolution with Ar/CO_2 (50/50) is much better than with Ar/CH_4 (90/10) or Ar/C_2H_6 due to the very slow drift velocity in Ar/CO_2 near the tube's wall, as well as its being a "cool gas." While the results for Ar/CO_2 appear insensitive to the electronic time resolution, this will not necessarily be so for signals originating close to the anode wire, noting that $x \propto \sqrt{t}$ (x distance from anode wire, t drift time).

6.1.6 Timing Performance of Gas Mixtures Containing CF_4

Being convinced by the good agreement between our measurements and published data for the three gas mixtures mentioned above, we made a further investigation for gas mixtures containing CF_4. This "fast" gas is believed to be one of the most attractive candidates for the SSC environment.[60, 61]

In this investigation the U. Penn preamplifier has been employed. The superior noise performance at high frequency of this amplifier allows us to benefit from the very narrow time distribution obtainable using CF_4 gas mixtures. We summarize the drift-time results in Fig. 42.

Very little data have been published on the drift velocity of CF_4/isobutane.[60, 62] Due to the very limited E/P region of these data it is not possible to infer the total drift time from them. The general trend of drift time *vs.* percentage of CF_4 in CF_4/isobutane mixtures and drift time *vs.* V/P looks reasonable. But the peculiar twisting behaviour between Ar/CF_4 (20/80), (0/100) and the other three mixtures may need to be confirmed by further study, because the first two mixtures were measured before oxygen and moisture filters were installed. However, the dependence of the drift time on the percentage of CF_4 and V/P is insensitive for Ar/CF_4.

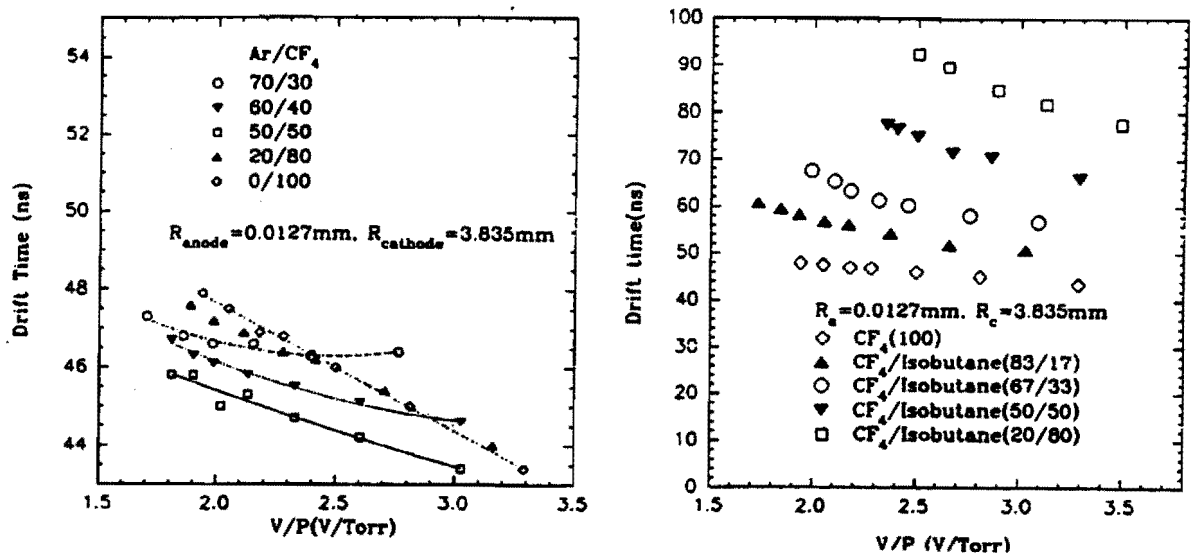

Figure 42: Total drift time of CF_4/Ar and CF_4/isobutane.

Figure 43 shows the time resolution with CF_4 gas mixtures. A slight improvement with increasing gas pressure can be seen. The time resolutions are in the 0.55-0.75 ns range for Ar/CF_4 mixtures, and 0.55-1.0 ns for CF_4/isobutane mixtures. Using data from Fig. 365 we can infer the spatial resolution for Ar/isobutane near the tube wall. Except for pure CF_4, all of the resolutions are 25-50 μm, as shown in Fig. 44. The big gap between pure CF_4 and the rest of the gas mixtures is attributed to the big gap in the published drift-velocity data. which we have used to convert time resolution into spatial resolution directly. Because there is no existing drift-velocity data for CF_4/isobutane (83/17), (67/33), we have adopted the (80/20), (70/30) data instead; this also tends to increase the gap artificially.

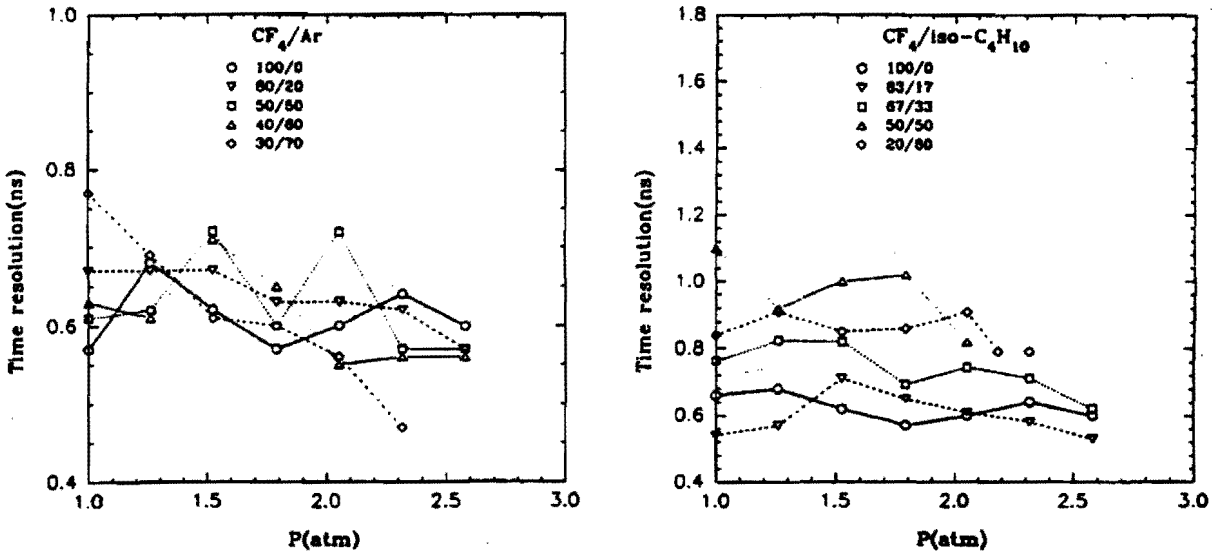

Figure 43: Time resolution of CF_4/Ar and CF_4/isobutane.

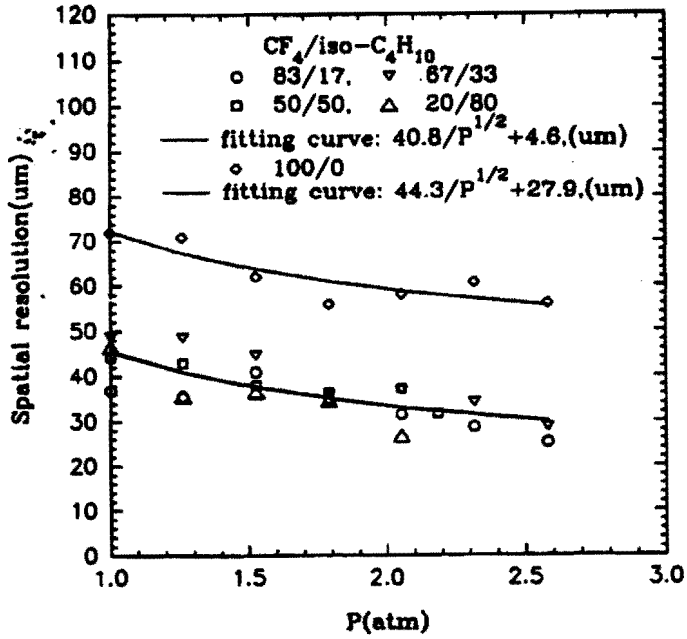

Figure 44: Spatial resolution of CF_4/isobutane.

6.1.7 Fluctuations in Single-Electron Avalanches

A detailed Monte Carlo study of timing strategies in drift chambers[63] has concluded that the simplest approach is still the best. The best accuracy obtainable is based on first-electron timing. Therefore fluctuations in the single-electron avalanche play an important role in timing measurements.

We have studied this with the same experimental set-up as in the timing measurements. Here we use an EG&G ORTEC 142PC charge-sensitive preamplifier instead of the transresistance preamplifier used for timing measurements.

For each gas mixture we first used the timing-measurement set-up to adjust the diaphragm until only one in 10-20 laser pulses yielded a photoelectron. Then the output of the drift tube was plugged into an EG&G ORTEC charge-sensitive amplifier. A wide gate signal generated by the photodiode was used to define the drift tube's signal after amplification. With this there was no evidence for any background pulses, and no background subtraction has been made in the data analysis. The only limitation in mapping the complete single-electron spectrum was the signal threshold which was set to discriminate against the noise.

6.1.8 Experimental Results

The single-electron-avalanche spectra from Ar/CF_4 and Ar/isobutane have been measured for several different mixing ratios. The N_2 laser was used for this. The single-electron-avalanche spectra were then fitted with the Polya distribution

$$P(a) \propto (ba/\bar{a})^{b-1} e^{-ba/\bar{a}},$$

where a is the amplitude of an avalanche, $\bar{a}$ is proportional to the mean gas gain, and b is a measure of the fluctuation of gas gain: $(\sigma_a/a)^2 = 1/b$. Typical experimental distributions with their Polya fitting curves are shown in Fig. 45.

We are able to observe the presence of electron attachment in the chamber gas as follows. Charge spectra were also recorded for each gas mixture at several different high voltages using an Fe^{55} source. If the signal size observed with the Fe^{55} source is not ~ 200 times that from a single photoelectron ejected by a laser pulse, then attachment has occurred. Comparisons of avalanches due to single photoelectrons with those from Fe^{55} x-rays for three Ar/isobutane gas mixtures gave rather consistent results. This convinced us that the gas system had little contamination and the technique for single-electron-avalanche measurement was reliable.

Then when Ar/CF_4 gas mixtures were tested, the large discrepancy between single-electron and Fe^{55} measurements indicates that CF_4 may have serious electron attachment.[60] The gas gain from single electrons was about ten times higher than that from Fe^{55}.

Some processes of electron attachment to CF_4 are summarized in Table 8.[60] Electrons of $\gtrsim 5$ eV can disassociate CF_4 with fair probability. Thus it appears likely that attachment will occur in higher-field regions, such as near the anode wire. The amount of attachment may be reduced somewhat by operating the chamber at lower gas gain – but then sensitivity to single electrons may be lost.

Additional evidence for electron attachment is the poor energy resolution observed with Ar/CF_4 mixtures. Previous work[60] yielded energy resolutions with Ar/CF_4 (95/5) and

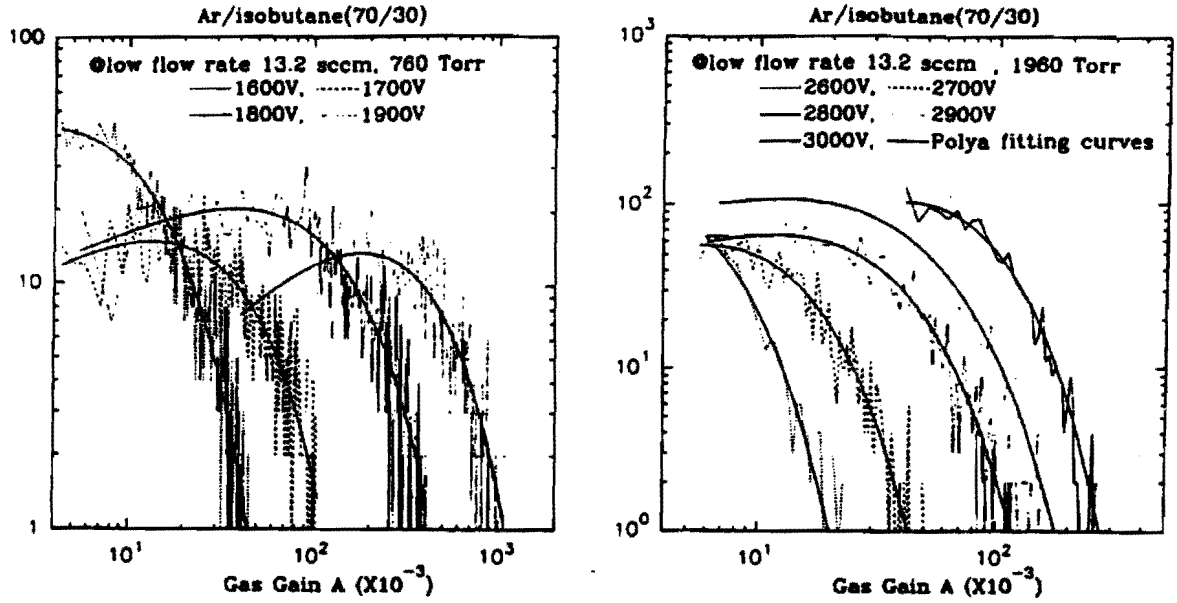

Figure 45: Single-electron-avalanche distributions with their Polya fittings for Ar/isobutane(70/30).

Table 8: Negative ions formed by electron impact on CF_4.

Process $CF_4 + e \rightarrow$	Threshold (eV)	eV at σ_{max}	Reference
$F^- + CF_3$	4.65 ± 0.1	6.15 ± 1	24
	4.7 ± 0.1		25
	4.5 ± 0.3		26
$F^- + CF_3^*$ or $F^- + F + CF_2$	$6.2 \sim 6.5$	~ 7.5	24
$CF_3^- + F$	5.4 ± 0.1	6.9 ± 0.1	24
	5.4 ± 0.1		25
	4.9 ± 0.3		26

(90/10) of $\sim$ 60% and $\sim$ 75%, respectively. We have measured the energy resolution for the mixing ratios (80/20), (70/30), (60/40), and (50/50) under different gas pressures. Typical values are summarized in Table 9, and some spectra are shown in Fig. 46.

Apparently the energy resolution of Ar/CF_4 worsens with increasing gas pressure and with increasing percentage of CF_4. In contrast the dependence of energy resolution on gas pressure for Ar/isobutane is not quite clear.

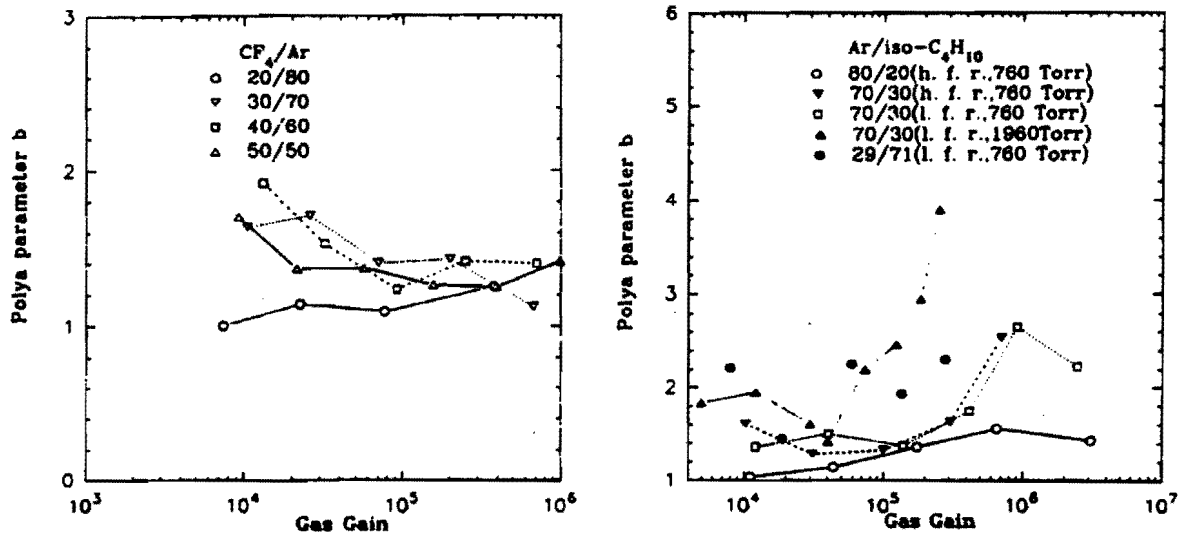

Figure 47: Polya parameters.

- The Polya distribution fits the gain spectrum of single-electron avalanches rather well. The Polya parameter b, which indicates the width of the fluctuation, has been determined for various mixing ratios of Ar/CF_4 and Ar/isobutane.
- Comparison of the gas gains obtained from single electrons as well as from Fe^{55} x-rays has revealed the likelihood of serious electron attachment in Ar/CF_4 gas mixtures, which is certainly due to the CF_4.
- Due to the electron attachment, CF_4 mixtures must be operated with higher voltages to compensate for loss of gas gain. The attachment also leads to large gain fluctuations, so these mixtures yield poor resolution of the deposited energy.

6.2 Model of Straw-Tube Detector Performance

We have parameterized the physics of the straw tubes and their timing electronics via a simple Monte Carlo model,[65] based on a similar model for drift chambers from SLAC.[66]

The model is as follows:

1. Along the track path within the gas, distributed via a Poisson distribution, are n ionization events/cm, n being different for each gas chosen. (The mean value of n is 25.5 for 1 atmosphere argon-ethane, for example.)

2. The electrons drift radially (excluding Lorentz angle effects) toward the wire in an electric field sufficiently high to saturate the drift velocity. They also diffuse radially according to a gaussian with a σ that is a constant times the square root of the initial radial distance from the wire. This diffusion constant is not in general accurately known for all gases.

3. At the wire, each electron is independently amplified by a factor A_i which is distributed according to the Polya distribution

$$P(x) = (3x/2)e^{-3x/2} \qquad \text{where} \qquad x = A_i/\langle A \rangle.$$

4. The tube acts as a transmission line driven by a current source giving a voltage pulse which is, to within a constant:

$$V(T) = A_i/(T_0 + T) \qquad \text{where} \qquad T_0 = 1 \text{ nsec.}$$

5. The amplified signal is characterized by a rise time T_r. This is approximated by assuming the amplifier response to a step-function input is a ramp of duration T_r followed by a long fall time.

6. The final signal that is fed to a discriminator is just the sum of the individual pulses delayed relative to each other by the electron arrival times at the anode. The dispersion in discriminator firing times (and thus the spatial resolution) can then be studied as a function of initial impact parameter, radial diffusion for a given gas, amplifier rise time and discriminator threshold.

Figure 48 compares the model calculation with the experimental results above as described above (but not previously shown). The agreement is encouraging. The model can then be used to predict the spatial resolution for minimum-ionizing tracks as a function of their impact parameter with the straw-tube anode wire, as shown in Fig. 49. If a fast-rise-time preamplifier is used, the lowest curve should be attainable in practice.

6.3 Simulation of Pattern Recognition in a Straw-Tube System

The appropriate momentum scale for detecting B events, produced primarily through gluon-gluon fusion, is quite low—on the order of the B mass. The subsequent decay of the B's will result in tracks with average P_t of approximately 1 GeV/c. Thus, the tracking has to be quite good, even to very low P_t. Studies have shown that significant loss of events occurs if the lower momentum cutoff for reconstructing B decay products is much above 300 MeV/c. This is certainly a challenge in a collider environment. In addition, the dipole field and spatially distributed vertices (in the beam direction) make this a more difficult problem than that commonly encountered in collider detectors using a solenoidal field, in which the tracks in the azimuthal view are circles coming from a single, well-defined beam-interaction point. Because of these challenges, the BCD has chosen to carry out its simulation to a level much more detailed than previous experiments at the proposal stage. Good tracking plays an integral part in one's ability to verticize B-decay candidates. So far, for these studies,

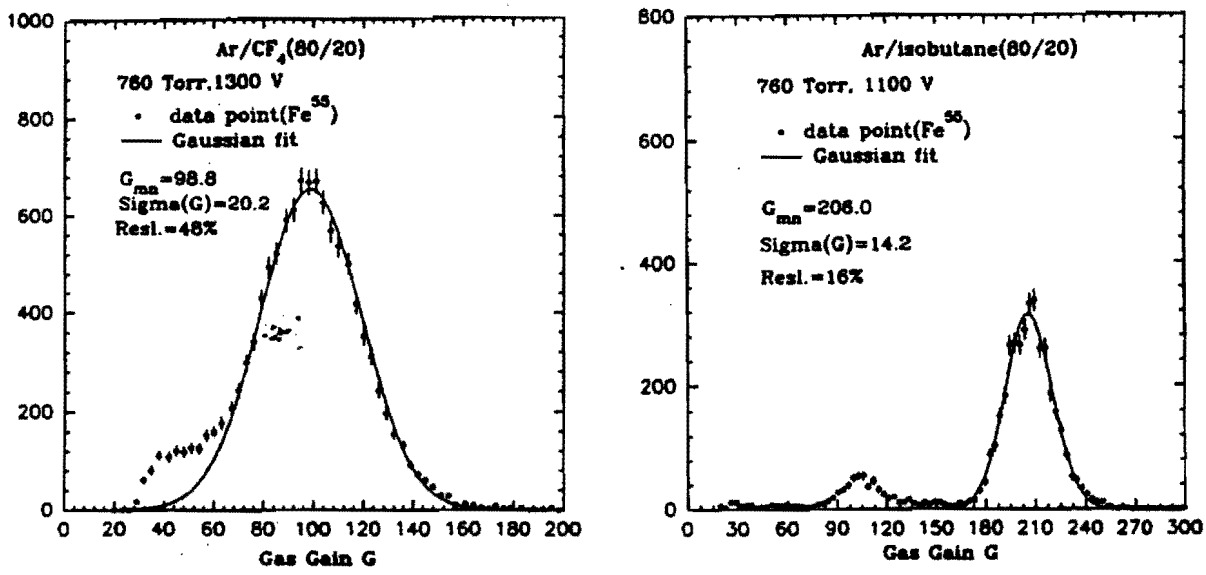

Figure 46: Charge spectra of Fe^{55} in Ar/CF_4 and Ar/isobutane.

Table 9: Energy resolution of Ar/CF_4 and Ar/isobutane using an Fe^{55} source.

Ar/CF_4	P (Torr)	H.V.	Gas Gain	Resolution (Fe^{55})
80/20	760	1300	98.8	48%
	1160	1600	105.9	61%
	1960	2100	107.2	82%
50/50	760	1500	119.0	53%
	1160	1800	92.2	63%
	1960	2400	89.1	98%
Ar/isobutane				
80/20	760	1100	206.0	16%
	1160	1300	377.1	18.4%
	1960	1700	243.8	17.3%
70/30	760	1200	210.5	16.4%
29/71	760	1800	994.9	16.7%
90/10	760	900	188.5	13.3%
	1160	1200	2564.0	12.5%
	1960	1500	1861.0	15.2%

6.1.9 Discussion of Energy Resolution

A statistical model of the energy resolution of proportional counters has been well established. There are two basic contributions to gas-gain fluctuations: variation in the number n_0 of electron-ion pairs, and variation in the size a of a single-electron avalanche. This can be expressed as the follows:[64]

$$\left(\frac{\sigma_A}{A}\right)^2 = \left(\frac{\sigma_{n_0}}{n_0}\right)^2 + \frac{1}{n_0}\left(\frac{\sigma_a}{a}\right)^2,$$

$$\left(\frac{\sigma_{n_0}}{n_0}\right)^2 = \frac{F}{n_0},$$

$$\left(\frac{\sigma_a}{a}\right)^2 = \frac{1}{b},$$

where F is the Fano factor and b is the parameter of Polya distribution. Finally we obtain

$$\left(\frac{\sigma_A}{A}\right)^2 = \frac{1}{n_0}\left(F + \frac{1}{b}\right). \tag{25}$$

Typical values of F and b are 0.05-0.2 and 1-2, respectively. Since n_0 is the number of ion pairs created by the incident radiation,

$$n_0 = E/W,$$

where E is the deposited energy, and W is the average energy loss per ion pair created. For Fe^{55}, $E = 5.9$ keV, and $W \sim 25$-35 eV. For all of the gas mixtures we have tested, $n_0 \sim 200$. The Polya parameters b for these gas mixtures are summarized in Fig. 47. All of them are greater than 1.

A rather surprising fact is that even under the worst case of F and b (but no electron attachment), the energy resolution of 5.9-keV x-rays still should be better than 18%. For Ar/CF_4 the measured energy resolution is worse than this by a factor of 3-5. If n_0 has been reduced by a factor of 9-25 due to electron attachment this behavior would be explained. As noted previously, such a reduction is consistent with the low mean value of the gas gain observed for Ar/CF_4 mixtures with an Fe^{55} source.

6.1.10 Conclusions

- Single-electron avalanches in a proportional counter have been successfully studied with a pulsed N_2 laser set-up. The drift time measurement for three well-understood gas mixtures are in good agreement with published data.
- The drift velocity in CF_4/isobutane is sensitive to the percentage of isobutane. The best time resolution in a 7.67-mm-thick proportional drift tube was ~ 0.6 ns.
- In contrast, the total drift time in CF_4/Ar is not sensitive to the mixing ratio, and is very fast. For five different mixing ratios tested the total drift time varied between 40 to 50 ns, all with time resolution ~ 0.6 ns. This corresponds to a spatial resolution of ~ 50 μm for a 3.83-mm drift.

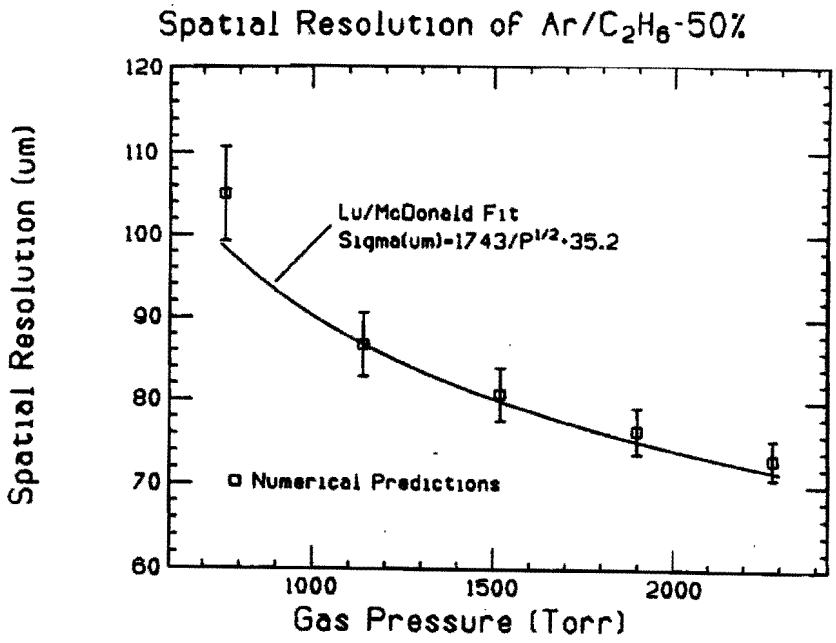

Figure 48: Numerical simulation of the spatial resolution in Ar/c_2H_6 (50/50).

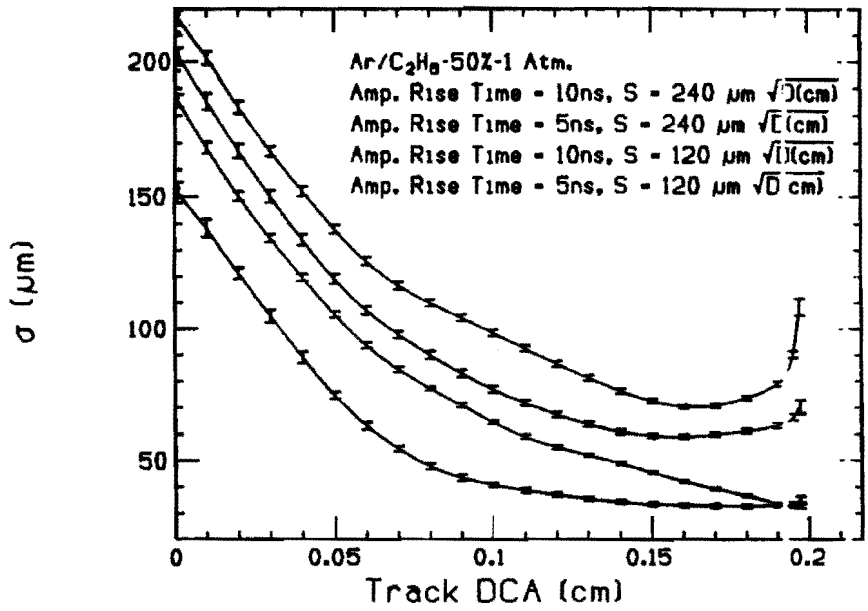

Figure 49: Numerical simulation of the spatial resolution of a straw-tube chamber as a function of the distance of closest approach (DCA) of a minimum-ionizing track to the anode wire.

the initial fit roads have been taken from the given generated momentum, smeared by the expected resolution of the straw tracking system. Straw pattern recognition and tracking will soon be combined with pattern recognition in the silicon to get a more realistic estimate of B-vertexing efficiency, in that actual found tracks will be used as the starting point.

6.3.1 Overview of the Straw-Tube-Simulation Strategy

The straw tracking planes are formed as superlayers of 8 individual planes of straws, all straws in a given superlayer having the same spatial orientation (x, y, u, or v). Superlayers of each type can then be grouped together to aid in pattern recognition. Figure 50 shows the current geometry modelled for the straw tracking system, as viewed in the direction of the magnetic field. The beams enter from left and right. All planes in the beam direction have an u-x-v-y multiplet. Some of the transverse planes have only an x-superlayer. Further optimization of this geometry is one of the goals of the straw simulation.

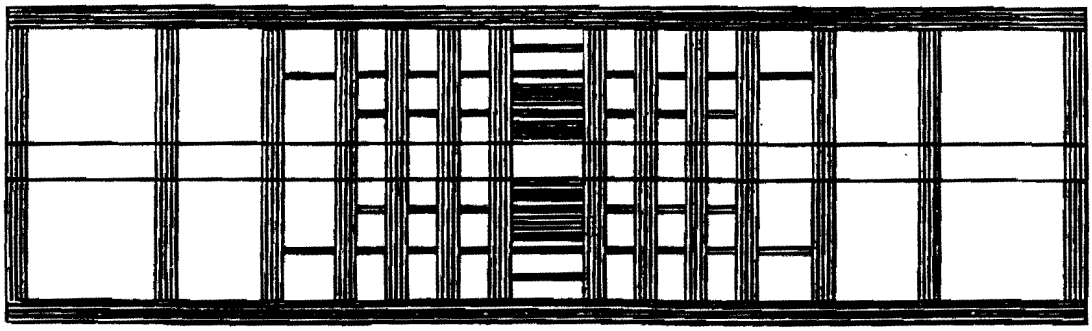

Figure 50: A view of the straw tracking system used in the computer simulation, looking along the direction of the magnetic field. This is the tracking system proposed for the full BCD experiment as sketched in Fig. 7.

Because of the complexity and time required to track through individual straw cells, we have chosen to separate the problem into two parts, as described in more detail below. Briefly, part one is a detailed, cell-level simulation that is intended to measure the pattern-recognition capability within a superlayer, combining hit straws (cells) into track segments called 'minivectors'. Part two is a full detector simulation which links these minivectors together, smeared by the appropriate resolution found in part one, to form tracks. We report here on part two only.

6.3.2 Full Detector Simulation

The goal for this part of the simulation is to find all minivectors associated with a given track, determine the track's momentum and finally to use these determined track parameters in the vertex-determining algorithms. Pairs of hits, representing found minivectors, are recorded at the entrance and exit of each superlayer, smeared by an assumed spatial resolution of

50 μm. At this stage of the study, no confusion from incorrectly identified minivectors is assumed. Minivectors in the outer layer of straw planes are then combined with an assumed primary-vertex position to give a starting search road. The primary-vertex position used is the true position smeared by 0.1 cm in the beam direction, a resolution that can be achieved from a simple fit to the silicon-plane data.

For simplicity, an almost completely hermetic outer layer of straw planes has been assumed. Forward and backward planes have a square beam hole of 10.6-cm half-size. Top, bottom and side chambers cover the full extent of the detector. Since less than 10% of the tracks exit via top or bottom planes, in reality these planes will probably not be built, but are included here for simplicity. In actuality, one would proceed to find tracks associated with the most outer layer of straw planes, eliminate minivectors from these tracks on more inner planes, and iterate inward toward the center of the detector. Again, for simplicity, a constant magnetic field has been assumed.

To start a fit, all pairs of u-v minivectors in an outer-layer plane are searched for a match to a minivector in an x-layer plane. These triplets are matched to a y-layer minivector. Losses at this stage of pattern recognition are small. For those tracks which are within the rapidity coverage of the straw tracking system, approximately 12% have momenta too low to arrive at an outer layer; typically these tracks have momenta well below 300 MeV/c, and are not of interest. For those tracks that do reach the outer straw layers, 95% are found and correctly matched. For the outer straw layers, the u-v planes have been configured as small-angle (15°) stereo planes with tubes running approximately perpendicular to the magnetic-field direction. This gives a match to the y coordinate (the magnetic-field direction) that is largely momentum independent, important in the outer planes that are used to determine the initial search road. For the inner straw layers, the small-angle u-v stereo planes have been configured with tubes running approximately parallel to the magnetic field direction, for increased resolution.

A simple unweighted circle fitter is then used to predict an initial bend-plane momentum. The nonbend-plane momentum is calculated from the dip angle. For the assumed minivector spatial resolution (50 μm) and primary-vertex z-position resolution (0.1 cm), the error on momentum for this initial fit is approximately 7%. Inner-layer planes are then searched with momentum-dependent roads for minivectors associated with each track. For planes in which more than one minivector is found within the search road, the mini- vector closest to the fit is retained. If a set of x-u-v-y minivectors have been found, all minivectors must be within the roads for any of them to be accepted. After all planes have been searched, if additional minivectors have been found, the momentum fits are updated using the x-plane minivectors only, and the search procedure is iterated. The momentum error for these updated fits has been reduced to 4% for momenta greater than 300 MeV/c. An improved fitting routine that uses minivectors from all plane types is now being written which will substantially improve this error.

Figures 51-52 show a typical event in the straw tracking system. This event was generated by ISAJET, using the $b\bar{b}$ two-jet process. Crosses on the figures represent the entrance and exit hits at the straw planes. Figure 51 displays all of the minivectors in the event, while Fig. 52 shows the found minivectors. For all tracks above 300 MeV/c that have outer-layer matches, 87% of the minivectors are found. For those tracks originating from the primary vertex, 91% of the minivectors are found. About 3% of the minivectors found for all tracks are

unassociated with the track. At this stage in the simulation, these numbers are encouraging.

Figure 51: A typical TEV I event from the $b\bar{b}$ two-jet process, showing all minivectors in the straw tracking system.

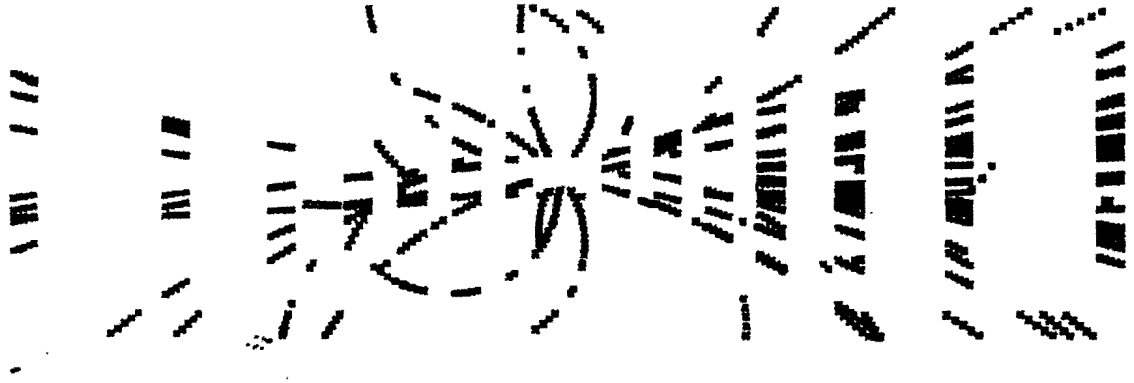

Figure 52: The same event, showing the found minivectors.

As the final step in our simulation we reconstructed the invariant mass of the B from tracks due to the decay $B_d^0 \rightarrow \pi^+\pi^-$. The mass resolution is about 30 MeV/c^2, as shown in Fig. 53, which indicates that the reconstruction program is working about as well as can be expected given the multiple scattering in the chambers.

6.3.3 Further Development

Several improvements are being implemented in the tracking pattern-recognition study:

1. Pattern recognition at the minivector level.
2. A more sophisticated fitting program.
3. Hit contention at the track level.

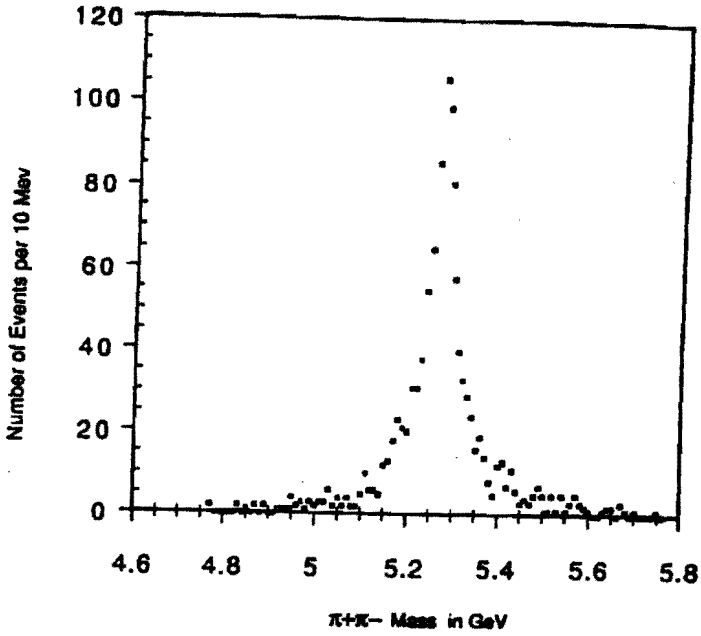

Figure 53: Simulated invariant-mass reconstruction of the decay $B^0 \to \pi^+\pi^-$. Multiple scattering and chamber resolution are simulated, and pattern-finding algorithms assemble the straw hits into tracks. The mass resolution achieved here is about 30 MeV/c^2.

4. After the initial search, two fits can be attempted: one including the primary vertex, and one without it. The best fit of these two could then provide a new search road. This may improve hit finding on tracks which originate close to, but not at the primary vertex.

5. Found minivectors can be eliminated, and the remaining minivectors examined for tracks that do not originate close to the primary vertex.

7 Appendix C: Particle Identification

A B-physics experiment needs identification of charged leptons and charged hadrons. Photons and neutral hadrons are of lesser value as they cannot be unambiguously assigned to a secondary vertex, and hence are less well isolated from the primary interaction than are charged B-decay products.

Very encouraging progress has been made over the last Summer by B. Hoeneisen, D. Anderson, and S. Kwan of Fermilab in the development of solid UV-sensitive photocathodes for use in a fast ring-imaging Čerenkov counter. Such a device with a liquid C_6F_{14} radiator would permit π/K separation up to momenta of 4 GeV/c in a very compact device.

Simulations of pattern recognition in a RICH counter have been performed by A. Lopez

and A. Mendez of U. Puerto Rico.

In the full BCD there is sufficient space that time-of-flight counters could also play an important role in the identification of low-momentum hadrons. S. Alam of SUNY Albany has been working on improving the time resolution of scintillation counters to below 100 ps.

In the full BCD, TRD's augment the electron identification in the electromagnetic calorimeter. J. Palathingal of U. Puerto Rico has developed a simulation of TRD performance to aid in making design choices.

The identified charged particles will, of course, be used in the full reconstruction of all-charged B-decay modes. In addition, they provide triggers and particle/antiparticle tags for the experiment. J. Heinrich of Princeton has recently been studying the efficiency and mistagging probability of various tags.

7.1 Low-Pressure RICH Counters with a Solid Photocathode

The viability of the Ring-Imaging Čerenkov (RICH) technique, which was proposed by Ypsilantis and Sequinot,[67] has been established by a number of groups[68] who have successfully built and tested devices for use in high-energy physics experiments. The central problem to be faced in designing a RICH counter for use at the TEV I or the SSC is obtaining stable operation in the anticipated high-rate high-multiplicity environment. The RICH detector must be sensitive to the single-photoelectron pulses from Čerenkov light, but insensitive to the ionization trails of through-going charged particles. Furthermore, it must be possible to extract signals using a narrow timing gate so as to minimize confusion from out-of-time events.

In most devices built thus far, an intrinsic jitter in photoelectron detection time arises because the absorption length of the photosensitive gas is long enough that the photoelectrons are produced at varying distances from the amplification region and therefore arrive at varying times. For example, the absorption length of TMAE at 30°C is about 15 mm, resulting in a 200-300 ns variation in pulse arrival time, depending on the carrier gas. Since this is several SSC bunch-crossing times, better time resolution must be achieved in the future. The solution we are proposing is based on a solid photocathode detector.

Such a detector is shown schematically in Fig. 54. The UV photons traverse the quartz window, pass through the anode-wire mesh, and eject an electron from the photocathode. This electron is accelerated towards the anode which is connected to a positive voltage source. The applied electric field is sufficiently high that avalanche multiplication occurs. Gains of 10^4-10^7 can be achieved depending on the gas type and cathode-anode spacing. The positive ions produced by the avalanche process drift towards the cathode. The induced charge on the pad is amplified in an SVX or BVX chip.

The cathode is sensitized to UV photons by an evaporated layer of CsI (work function 6.4 eV) + adsorbed TMAE (work function 5.3 eV). It has been shown[69, 70] that this photocathode has a (high) quantum efficiency *vs.* photon energy that is characteristic of TMAE rather than CsI. Furthermore, the combined CsI-TMAE surface appears to be more stable against necessary exposure to air during detector assembly than either material separately. Chamber gases that are compatible with long life of the TMAE surface are methane, ethane, isopropyl alcohol, *etc.*, at pressures in the range 5-60 Torr. Our own work over the past summer,[26] described below, has demonstrated that a fast timing signal from single pho-

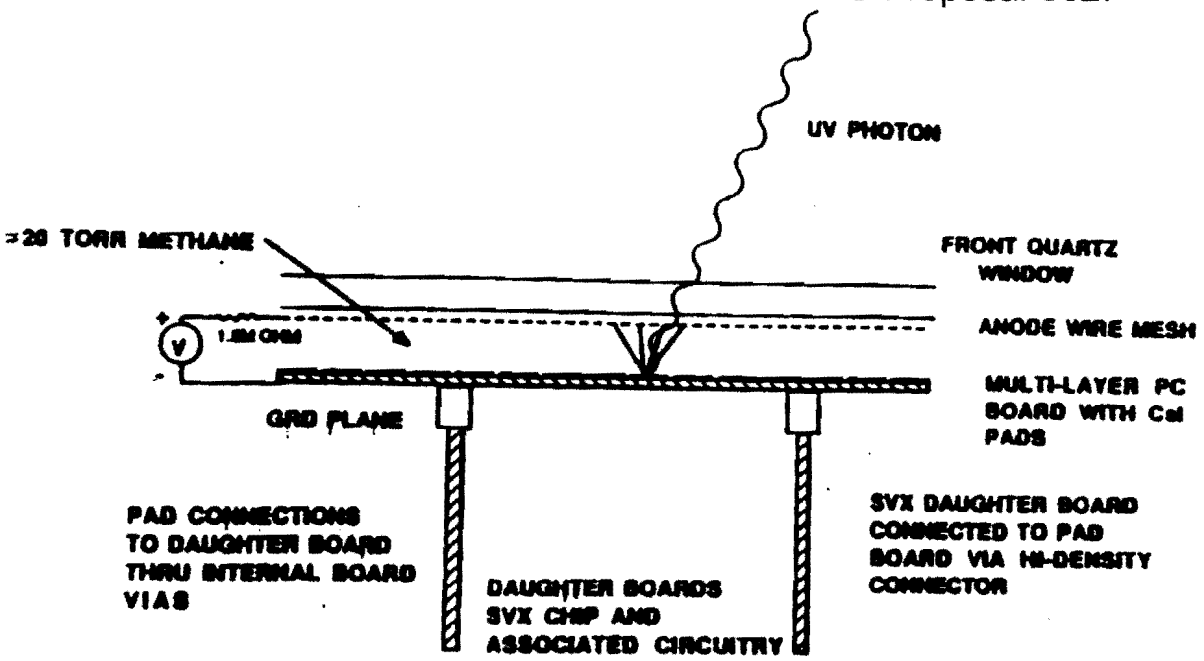

Figure 54: Overview of the photodetector with quartz window, anode-wire mesh, and cathode plane sensitized to UV photons with evaporated layers of CsI and TMAE.

toelectrons can be obtained using such a photocathode. Operation of the detector at low pressures also reduces the sensitivity to passing charged particles in a 4π environment.

Such a detector could meet all the requirements for operation at a hadron collider. It permits subnanosecond timing resolution, has imaging capability, a small thickness, and is almost immune to magnetic fields.

7.1.1 Experimental Setup

The experimental detector of ultraviolet photons is shown schematically in Figure 55. The photocathode metal pads (on a G-10 printed circuit board) are sensitized by an evaporated CsI layer with adsorbed TMAE. The detectors built have (L, LD) = (3.18, 15.2), (1.59, 19.2), (0.794, 18.4), (0.13, 19.2) in mm. The anode is either a mesh (of stainless-steel wires 12.7 μm in diameter with 254-μm spacing, 90% transparent), or a wire plane (gold-plated tungsten of 20-μm diameter and 1-mm pitch). The gas in the chamber is typically at a pressure of 5 to 60 Torr.

A UV photon traverses the quartz window, the ground-wire mesh, and the anode-wire mesh, and releases a single electron on the surface of the solid photocathode. This electron drifts towards the anode which is connected to a positive-voltage source. The applied electric field is sufficiently high that avalanche multiplication occurs. Gains from 10^4 to 10^7 are achieved depending on the gas and cathode-anode spacing. The induced current on the pad is amplified externally to the detector.

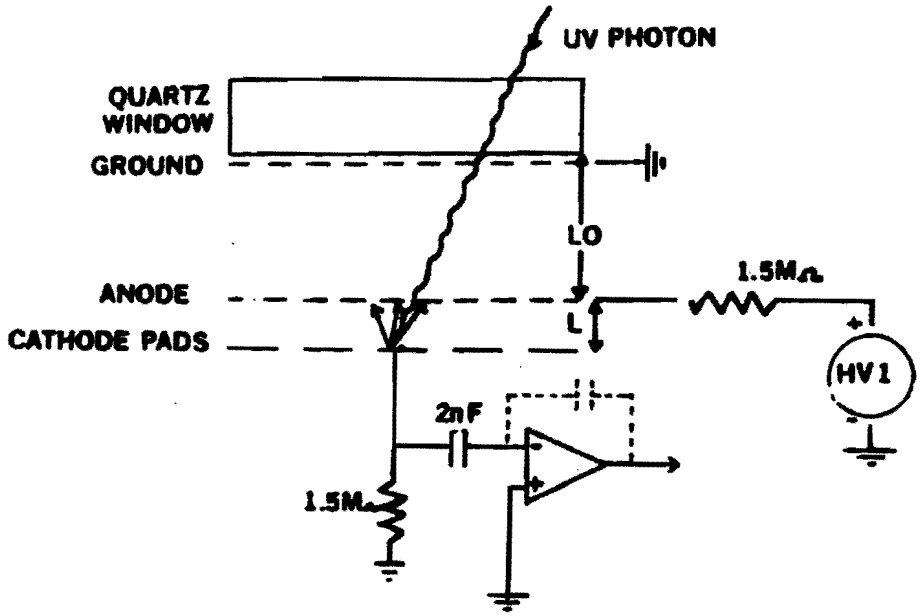

Figure 55: Sketch of the test UV-photon detector.

The UV light source used is a hydrogen-arc discharge lamp operating in a relaxation mode. The light source has a pickup that permits triggering on the light pulse. This light pulse has a full width at half maximum less than 3 ns and has a broad spectrum of wavelengths down to the quartz window cutoff at $\sim$ 170 nm. The desired wavelength is selected with a monochromator (flushed with nitrogen to avoid the UV absorption of air).

The current pulse on a pad, observed directly on an oscilloscope with 50-ohm input impedance, is shown in Fig. 56 for isopropyl alcohol at 7 Torr, an anode voltage HV1 = 410 V, and a cathode-anode spacing of 0.794 mm. Note that this pulse has a "fast" component (shown in detail in Fig. 56b) and a "slow" component. The "fast" component has a delay with respect to the light pulse of 4.5 ns, and a full width at half maximum of 2.5 ns.

A simple model of parallel-plate amplification is illustrated in Fig. 57. In the example of Fig. 56 the "slow" component has a duration of $\sim$ 400 ns and is due to ion drift from anode to cathode. This ion collection time is almost three orders of magnitude shorter than that for a chamber operated at atmospheric pressure. The ion drift velocity in this case is v_i = 0.2 mm/100 ns. The "fast" component of parallel-plate amplification is due to electrons as shown in Fig. 57. The saturated drift velocity of electrons in this example is v_e = 18 mm/100 ns. This is about a factor of four greater than at atmospheric pressure. The gain in this example is $G = 4.2 \times 10^4$. The ratio of the charges in the "slow" and "fast" components is $\sim$ (4.5 mV $\times$ 400 ns)/(80 mV $\times$ 2.5 ns) = 9, which is approximately equal to $\ln(G) = 10.6$, as expected (see Fig. 57).

To measure the quantum efficiency of the solid photocathode we have devised a technique to determine this relative to the known quantum efficiency of TMAE gas. We have designed the experimental chamber so that it may also operate with photoconversion in TMAE gas as

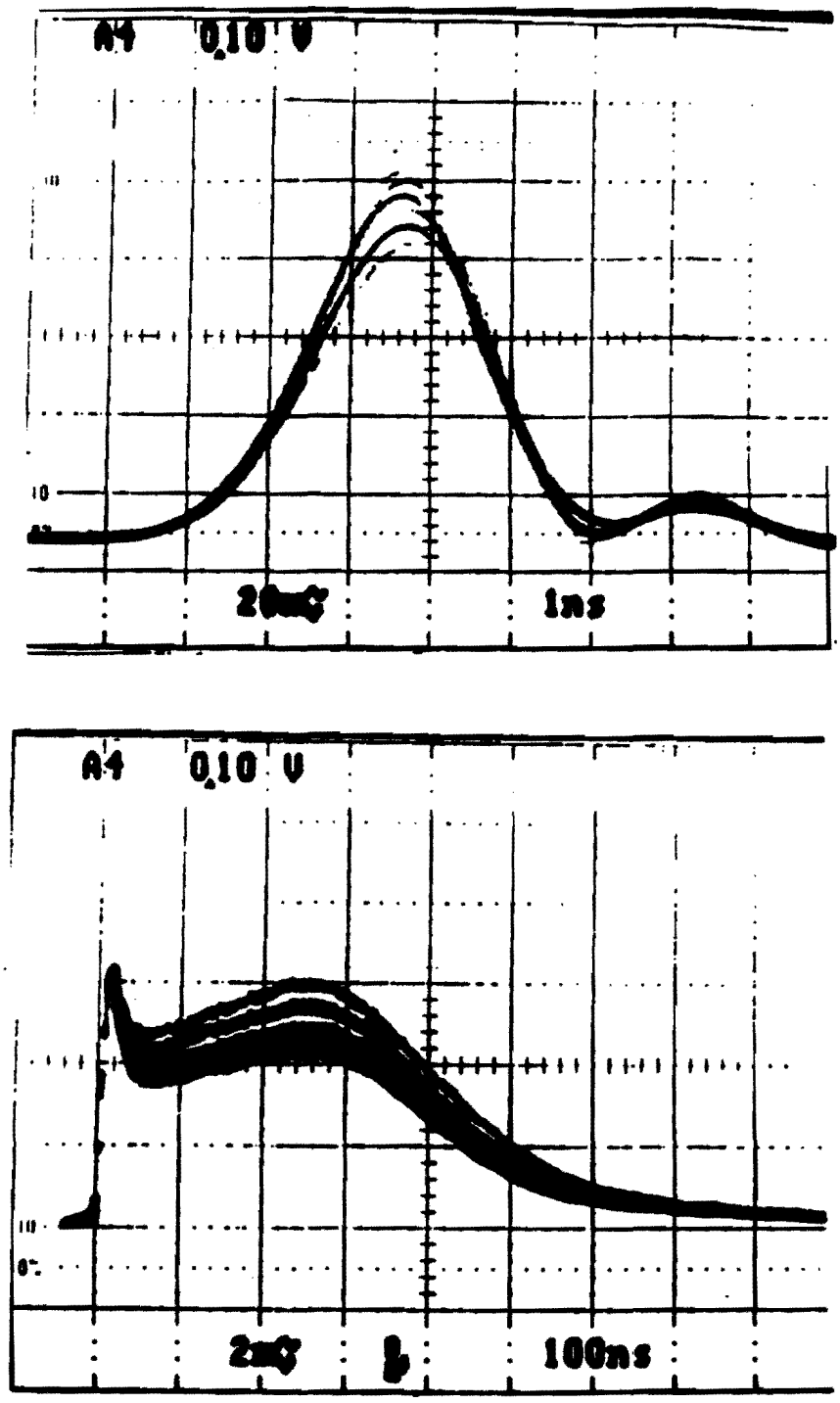

Figure 56: Current pulse of on a pad observed with an oscilloscope with 50-ohm termination. a) The "fast" and "slow" components of the current pulse with the bandwidth of the oscilloscope limited to 20 MHz. b) Detail of the "fast" component with the full 350-MHz bandwidth of the oscilloscope.

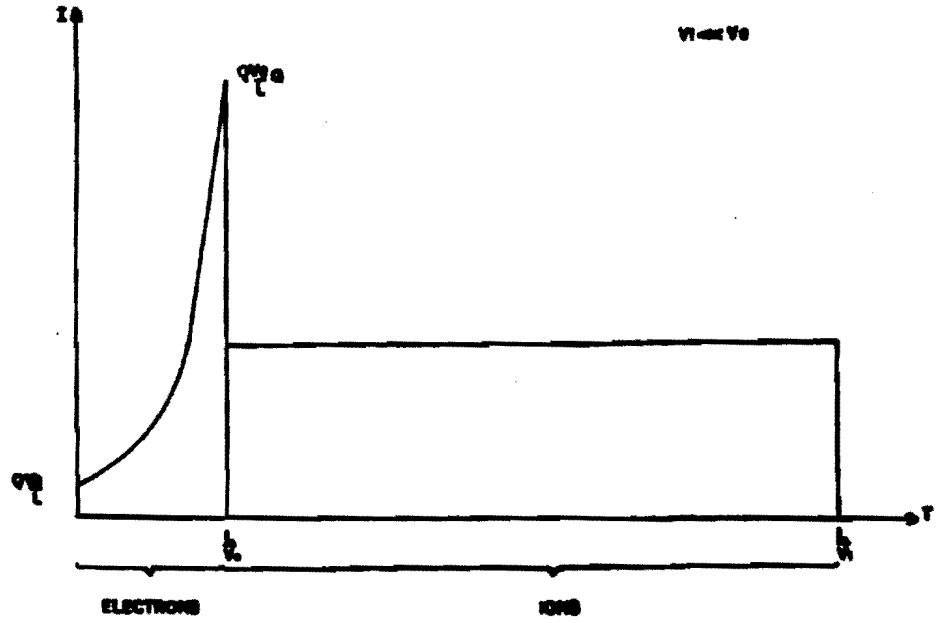

Figure 57: A model of the cathode-pulse shape. Induced current i on cathode or anode as a function of time t for parallel-plate avalanche multiplication. q is the elementary charge, L is the cathode-anode spacing, G is the gain, and v_e and v_i are the electron and ion drift velocities, respectively. The "fast" electron component increases exponentially with time constant $L/v_e \ln G$ due to the avalanche multiplication. The charges in the "slow" ion and "fast" electron components are qG and $qG/\ln G$, respectively. The anode is assumed to be a wire mesh with wire spacing $\ll L/\ln G$.

shown in Fig. 58. In this mode of operation the UV photon traverses the quartz window and the front wire mesh, and is absorbed by a TMAE molecule in the conversion gap releasing an electron. This electron drifts to the center wire mesh and is then amplified by avalanche multiplication as it traverse the 'amplification' gap and arrives at the pad plane (now the anode).

In Fig. 59 we show the current on the pad. In this example the gas is 0.344-Torr TMAE + 60-Torr methane, HV1 = 351 V, and HV2 = 938 V. From Fig. 59 it can be concluded that in this example the electron collection time across the entire 18.4-mm conversion gap is 232 ns, which corresponds to an electron (saturated) drift velocity of 8 mm/100 ns; and the ion drift time across the 0.794-mm amplification gap is $\sim$ 600 ns, which corresponds to an ion drift velocity of 0.13 mm/100 ns. Note that the instant of photoconversion is uncertain by the time it takes an electron to drift across the conversion gap, *i.e.*, 232 ns. This time "jitter" may be reduced by heating the TMAE and chamber (to increase the TMAE vapor pressure and decrease the photon absorption length) or by using a solid (or liquid) photocathode as in the present work.

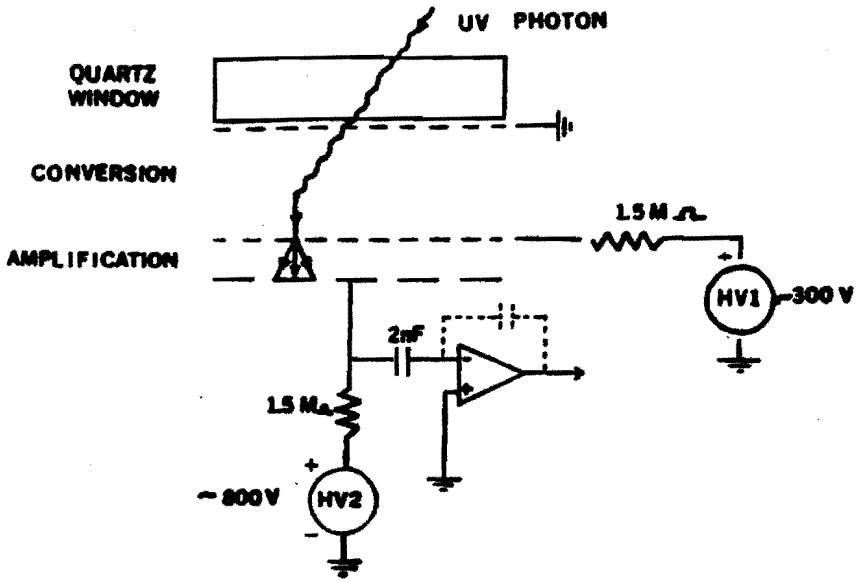

Figure 58: Experimental detector operating in the TMAE gas photoconversion mode. The gas is typically 0.35-Torr TMAE + 60-Torr methane.

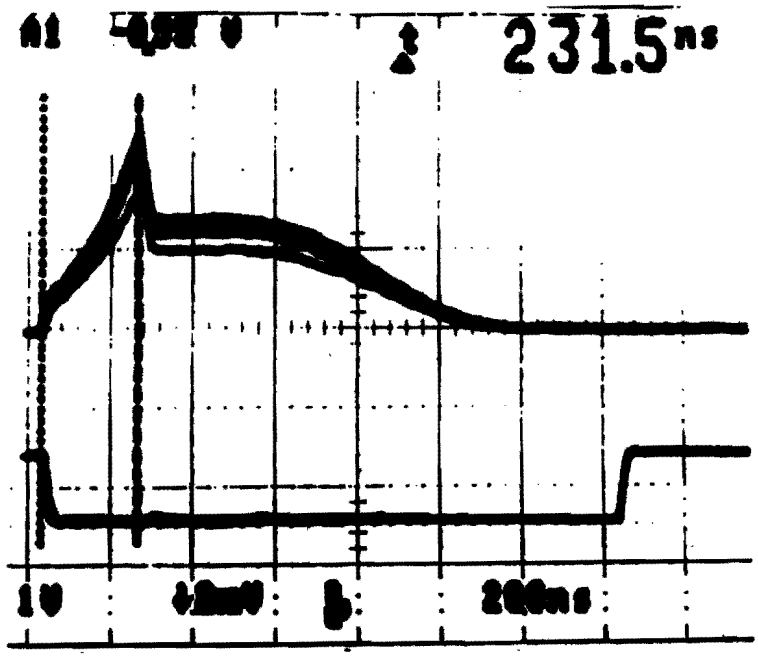

Figure 59: Current pulse on pad of detector operating in the TMAE gas photoconversion mode. The gas is 0.344-Torr TMAE + 60-Torr methane.

7.1.2 Gases

Several gases transparent (or semi-transparent) down to the quartz cutoff wavelength have been tried. We obtain sufficient gain to observe single photoelectrons above the amplifier noise with the following gases (or mixtures of these gases): methane, ethane, pentane, hexane, ethanol, methanol, isopropyl alcohol, acetone and TEA (isopropyl alcohol shows significant ultraviolet absorption). Insufficient gain is obtained with the following pure gases: helium, argon, nitrogen and isobutane.

Figure 60 shows the maximum gain as a function of pressure for several gases and cathode-anode spacings. Note in Fig. 60b that for each gas there is an optimum pressure at which the achievable gain is a maximum. Figure 60a shows that this behavior may be peculiar to a cathode-anode spacing $\sim$ 1.59 mm. Note also that the highest gains ($\sim 10^7$) correspond to the relatively slow gases: hexane and isopropyl alcohol. In this preliminary study we did not find gas mixtures with higher gain than either component separately.

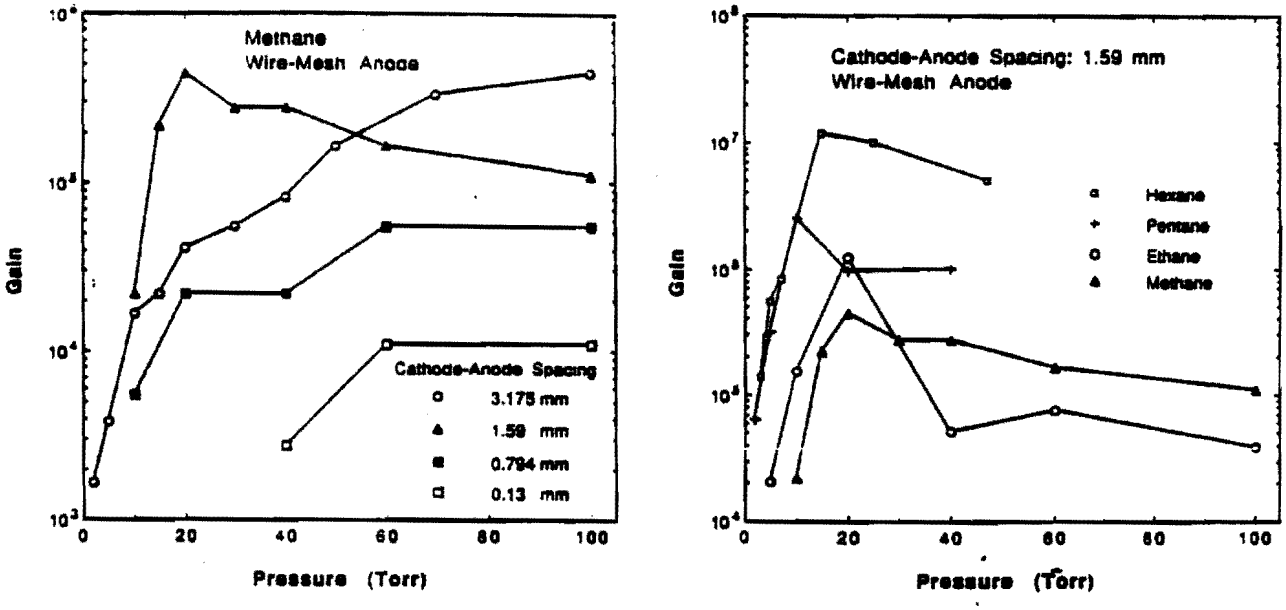

Figure 60: Maximum operating gain as a function of pressure for several gases and cathode-anode spacings.

We also measured the maximum gain with a wire plane anode instead of a mesh. Higher gains can be achieved as shown in Fig. 61.

7.1.3 Photocathode

The photocathode is fabricated as follows. A pad pattern is etched on a G-10 printed circuit board with copper cladding on both sides. The board is cleaned with an abrasive, acetone, and ethyl alcohol. A 0.2-μm layer of aluminum is evaporated onto the copper pads in vacuum

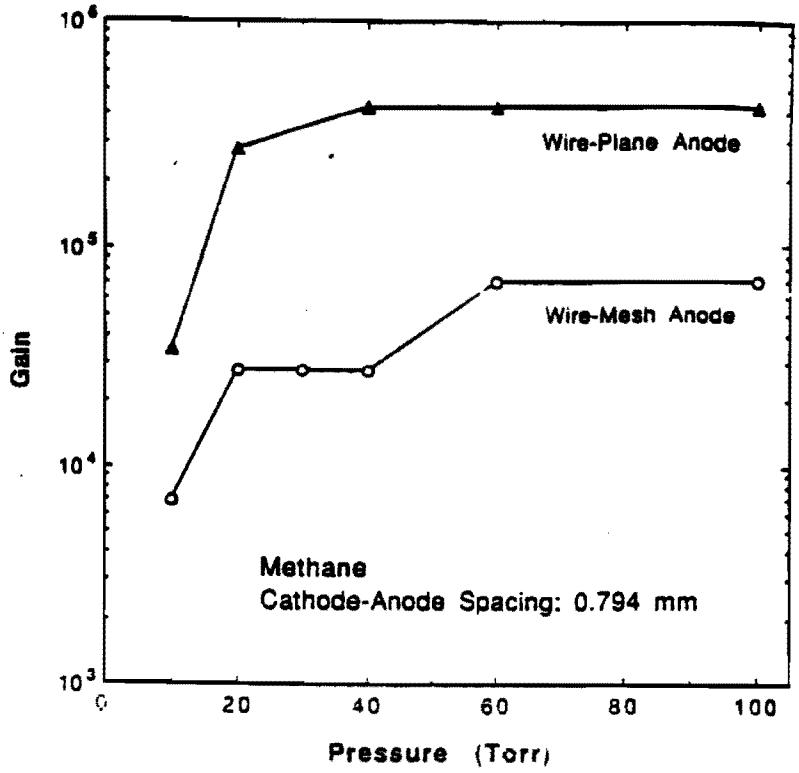

Figure 61: Maximum gain of methane with a wire-plane anode compared with a mesh anode.

at a nominal pressure of 5×10^{-5} Torr. The reason for the aluminum evaporation is to obtain a cleaner surface for the subsequent evaporation of CsI.

The vacuum is broken and the tungsten boat with aluminum is replaced by a molybdenum boat with CsI of scintillator purity. The distance between the boat and the printed circuit board is 21 cm. Layers of 0.3, 0.5, 0.8, 1 or 2 μm thickness CsI are evaporated onto the pads in vacuum at a nominal pressure of 5×10^{-5} Torr at a rate between 0.01 and 0.026 μm/s. The thickness of the evaporated layers is monitored with a quartz crystal.

Immediately after the evaporation of CsI, and without breaking the vacuum, the evaporation chamber is filled with TMAE gas to a pressure of $\sim$ 100 mTorr in order to adsorb a layer of TMAE on the CsI film. To reduce the time from the end of the CsI evaporation and the TMAE adsorption, a tube directs the TMAE to the photocathode.

The vacuum is broken and the photocathode board is removed from the evaporation chamber and is mounted into the detector chamber which is then pumped down to a nominal pressure of 1 mTorr. In this process the CsI + adsorbed TMAE photocathode is exposed to the humid ambient air for 20 to 50 minutes. The photocathode is not exposed to TMAE gas again except for the measurement of relative quantum efficiency to be described above.

Test pads with no aluminum evaporation were also prepared for comparison. We observed that the aluminum evaporation does not increase the quantum efficiency. The reason for adsorbing TMAE onto the CsI is as follows: it has been observed that the quantum efficiency of CsI with adsorbed TMAE does not change with a one-hour exposure to air.[69] This observation is amazing since separately CsI reacts with the water in air,[68, 72] and TMAE reacts with the oxygen in air degrading their quantum efficiency in minutes.

It is also observed that CsI with adsorbed TMAE has a greater quantum efficiency than pure CsI.[69, 70] We have measured the quantum efficiency of the detector in the solid photocathode mode (Fig. 55) relative to the quantum efficiency of the detector operated in the TMAE gas photoconversion mode (Fig. 57). The method used is photon counting with the slits of the monochromator adjusted so that the average number of detected photons per pulse of the UV light source is ~ 0.1 to 0.3. The number of detected pulses is obtained with a multichannel analyzer. We obtain a ratio of the quantum efficiency of the detector operated in the solid photocathode mode to the quantum efficiency of the detector operated in the TMAE gas mode of 0.79 ± 0.05, independent of wavelength from 175 nm to 215 nm, and independent of the CsI thickness from 0.3 μm to 2 μm. This measurement was done after operating the chamber for one week.

The absolute quantum efficiency of the solid CsI + adsorbed TMAE photocathode is obtained by multiplying the known[76] quantum efficiency of an optically thick layer of TMAE gas shown in Fig. 62 by the following factors:

0.79 (ratio of efficiencies of detector operating in photocathode and TMAE gas modes);

0.52 (typical fraction of photons absorbed in 19.2 mm of TMAE at 0.34 Torr[76]) ;

1.1 (to account for one extra mesh in the solid photocathode mode).

The result is presented in Fig. 62.

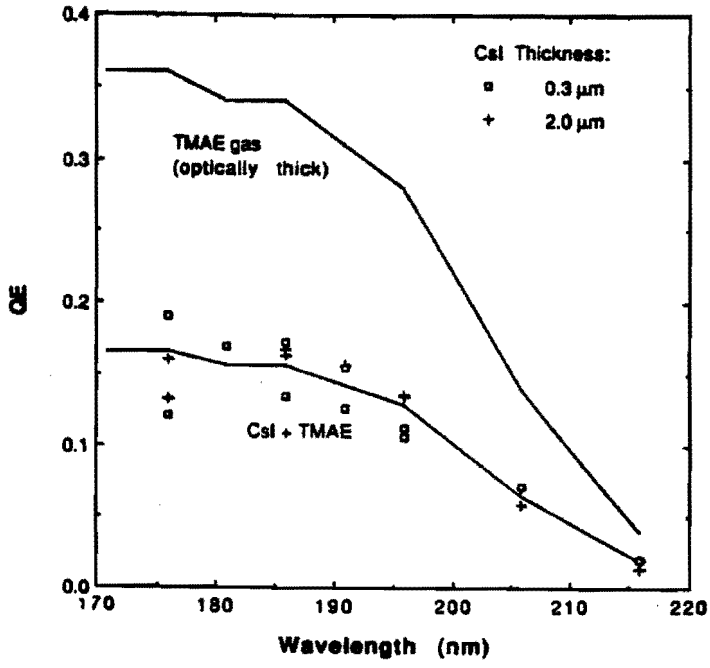

Figure 62: Quantum efficiency of CsI + adsorbed TMAE photocathodes relative to gas TMAE. The quantum efficiency of gas TMAE, which is used as a reference, is taken from R. A. Holroyd *et al.*[76]

7.1.4 Figure of Merit

On one occasion using a pin-hole collimator it was possible to resolve peaks corresponding to 1, 2, 3 and 4 photoelectrons as shown in Fig. 63a. This resolved pulse height spectrum could not be reproduced on subsequent days. Typical pulse-height spectra are unresolved as shown in Fig. 63b.

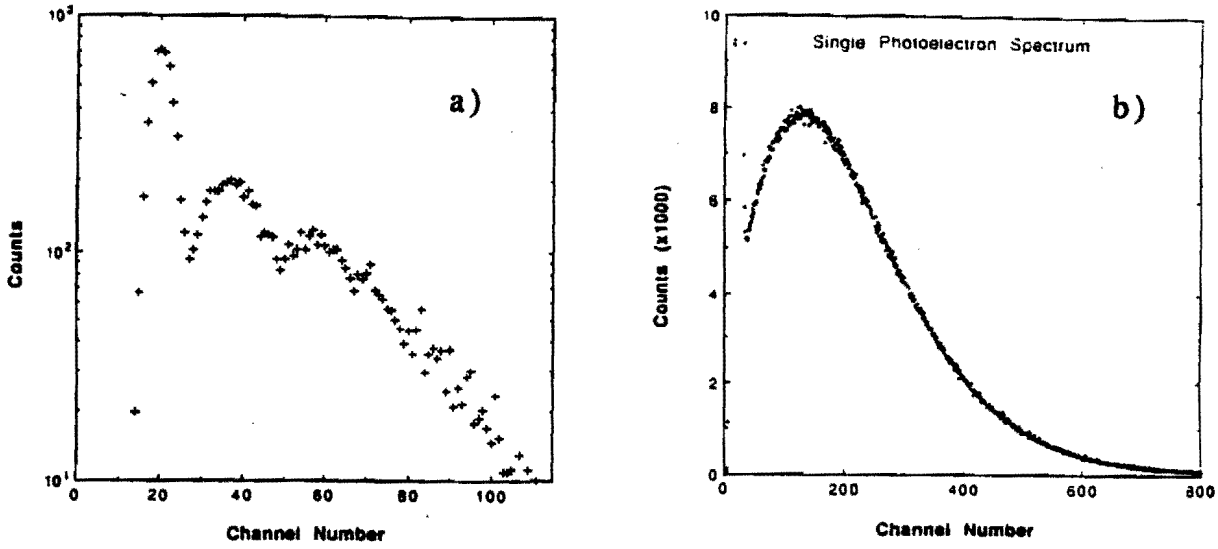

Figure 63: Pulse-height distribution obtained with a multichannel analyzer: a) the resolved peaks corresponding to 1, 2, 3, and 4 photoelectrons; b) a usual (unresolved) single-photoelectron distribution with a mean of 0.49 photoelectrons per pulse of the light source. Note that this distribution has a maximum.

To obtain good timing resolution with pulses of varying height it is necessary to use a discriminator with a threshold proportional to the pulse height. The time resolution is then determined by noise:

$$\delta_t = \frac{V_N C}{I} = \frac{V_N C \tau}{Q} = \frac{\tau}{(V_S/V_N)},$$

where τ is the ion transit time from anode to cathode, $Q = qG$ is the ion charge, C is the capacitance of pad and amplifier, $V_S = Q/C$ is the signal voltage corresponding to an integrating amplifier ($R > \tau/C$), and V_N is the root-mean-square noise voltage.

As an example, take ethane at 20 Torr and a cathode-anode spacing of 1.59 mm (see Fig. 60b) for which we have measured $\tau = 700$ ns. The detector may be operated at a signal-to-noise ratio $V_S/V_N = 100$ to obtain a time resolution of order 7 ns. The measured signal-to-noise ratio before breakdown in this case is 800. For hexane and isopropyl alcohol we have obtained single photoelectron signal-to-noise ratios of order 104.

The detection of the "fast" component of the current pulse for single photoelectrons is possible but not practical for our application as it requires the highest achievable gains (which implies fast aging and the possibility of breakdown).

To understand the noise issue in more detail, let us use the Johnson relation

$$\frac{V_N^2}{R} = nkTB,$$

where n is the noise figure, $B = 1/(2\pi RC)$ is the bandwidth, C is the capacitance, RC is the integration time constant of the amplifier, k is the Boltzmann constant and T is the absolute temperature. Note that the resistance R cancels and the time resolution can be written in the form

$$\delta_t = \frac{\tau}{qG}\sqrt{\frac{nkTC}{2\pi}}.$$

In conclusion, a small time resolution requires low capacitance, small noise figure, short ion transit time, and high gain. Note that a figure of merit of the parallel-plate avalanche amplifier is the current qG/τ. Methane is a relatively fast gas, for which the optimum pressure and cathode-anode spacing are $\sim$ 20 Torr and $\sim$ 1.6 mm., respectively.

7.1.5 Aging

During this investigation measurements were made on several photocathodes for a period of approximately 3 weeks each. The photocathodes are typically exposed to air four times for a total of approximately 160 minutes. It is noted that during the three week period the quantum efficiency of the used pads drops by a factor of order 1/3. There is little or no degradation of quantum efficiency of unused pads. The most rapid loss of efficiency apparently occurs when measurements with TMAE gas are being made, especially if an intense mercury source is used instead of the pulsed hydrogen source. It is known that TMAE gas is corrosive.

Also a loss of quantum efficiency is noted when working at the highest gains with hexane. This loss of quantum efficiency may be due to deposits onto the photocathode of hydrocarbon radicals produced in the avalanche process.[73, 74, 75] Another cause of loss of quantum efficiency may be due to chemical reactions of the photocathode with corrosive radicals produced in the avalanche process.[73, 74] It is known that an intense flux of UV photons may increase the concentration of Cs atoms on the surface of the photocathode.[74]

From previous studies[73, 74] we know that methane breaks down into CH_2 and produces polymers. Ethane produces little polymerization but may form corrosive aldehydes by photodissociation; Ethanol and methanol do not polymerize but produce corrosive formaldehyde. Isopropyl alcohol does not polymerize and produces no aldehydes, it photodissociates into hydrogen and acetone which have cleaning action. Hexane may polymerize into liquid or solid products at room temperature. The "fast"[61] gas CF_4 is electronegative and its photodissociation products may etch surfaces. It has been observed that mixtures of ethane and isopropyl alcohol show no polymerization or corrosion[73] and is therefore a good candidate for aging studies.

It is clear that the aging problem must be overcome. A systematic study of aging is under way.

7.1.6 Conclusions

We have shown that a solid photocathode that can be handled in air, with a UV-quantum efficiency of $\approx$ 16%, can be routinely fabricated. This photocathode can be deposited on a pad for readout, and operated with a single-step low-pressure avalanche amplification with high gain ($\sim 10^4$ to 10^7). Such a device has the timing resolution and rate capability necessary for operation at a hadron collider. Operating at low pressure and in parallel-plate mode, the chamber should be insensitive to passing charged particles.

The problem of supporting the large quartz window with a differential pressure of one atmosphere is manageable. The distance from photocathode to quartz window would be on the order of 2 mm, with a wire mesh about 1.5 mm from the photocathode. At the corner of each pad one can place a small ceramic bead with a corresponding bead between the mesh and the window. Thus the window and backplane can be supported every cm or so.

The one serious remaining problem is that of aging of the photocathode. The observed aging is almost certainly the result of contamination due to cracking of the counter gas. It is believed that mixtures such as ethane and isopropyl alcohol[73] will improve the situation if not solve the problem altogether. A systematic study of aging is under way. In any case, the aging problem does not seem to be as bad as it has been for RICH detectors operated with gaseous TMAE.

Based on these studies, we are ready to construct a prototype RICH detector. The technology explored here is suitable for industrial production of detector modules that can be assembled like tiles for almost any experimental configuration.

7.1.7 Prototype RICH Counter for Beam Tests

We are currently constructing a prototype detector at U. Pennsylvania that is large enough to contain a full Čerenkov ring from a high-momentum track impinging on a liquid C_6F_{14} radiator. The prototype is shown in Fig. 64. It consists of a cylindrical stainless-steel vessel, 10 inches in diameter and 5 inches long. The device operates at low pressure, typically 10 Torr. The entrance window is 1/8-inch-thick quartz. The anode is a stainless-steel mesh (25-μm wire), and the cathode, which serves as the vacuum seal as well, is copper-clad G-10, about 1/4 inch thick. The pads are 5-10 mm square and there is one amplifier connected to each of the 1024 pads. The amplifiers are the SVX-D chip, with 128 channels per chip.

In addition, a smart pad-chamber is being constructed with palladium evaporated onto the cathode plane, giving about 5-kΩ resistance between pads. There are than only 256 smart pads, also read out into SVX-d amplifiers. Good spatial resolution is obtained via measurement of charge sharing among the amplifiers at the corners of each smart pad.

In both chambers, the photocathode is 1 μm of CsI and a monolayer of adsorbed TMAE.

7.2 Simulation of Pattern Recognition in a RICH Counter

An ISAJET/GEANT simulation of a RICH counter has been performed for the Central RICH counter of the full BCD configuration.[77] In this the liquid radiator is located at a radius of 105 cm, followed by a 25-cm drift space to the photodetector at a radius of 130 cm.

Figure 65 shows the simulated pattern of photons hits over the surface of the RICH counter for a typical event. Confusion due to overlapping rings in minimal. However, about

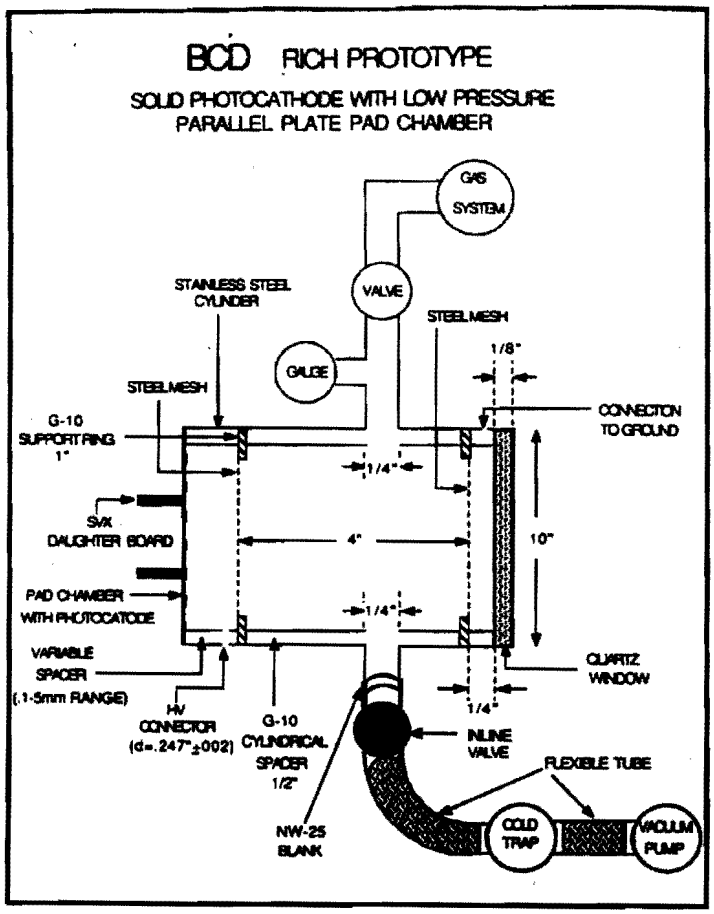

Figure 64: The BCD prototype low-pressure RICH detector. Čerenkov photons enter from the right and impinge on the solid photocathode. The liberated electrons are then accelerated back to the steel-mesh anode and the signals from the electron avalanches induced on the pads are read out with the SVX-D amplifiers.

25% of the rings intersected the boundary of the detector. The hardware must reflect the out-of-bounds hits back into the active detector area, and the software be able to identify the resulting folded rings.

The detector area was subdivided into large 'smart' pads that can each measure the coordinate of a photon hit to $\sim 1/20$ of a pad width. A pad is said to be cleanly hit if it is struck by exactly one photon. Figure 66 shows the number of clean hits per ring as a function of pad size. The quality factor (Q.F.) of 65 photons/cm is the more realistic assumption. Pads of 3 cm $\times$ 3 cm result in about 80% of the struck pads being cleanly struck. Multiple hits on a pad are mainly due to photons from the same charged particle, rather than different particles. The effect of the multiple hits on π/K separation is under investigation.

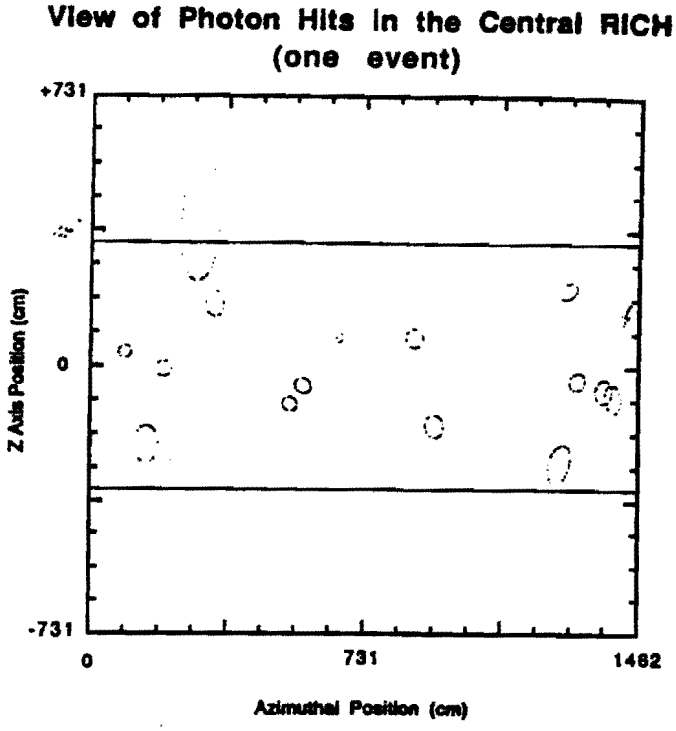

Figure 65: The distribution of Čerenkov-photon hits over a Central RICH counter, according to an ISAJET/GEANT simulation.

The distance between Čerenkov rings in this simulation is about 5 times that in the μBCD configuration, and the size of the rings is 2.5 times larger than those in the μBCD. Hence the probability of overlapping rings will be about twice as large in the μBCD as in the simulation. The more serious problem of multiple hits on a pad from the same ring requires the pads to be smaller in the μBCD. The results of Fig. 66 will hold for the μBCD if the pad size is scaled by 1/2.5. That is, a 5-mm pad in the μBCD is equivalent to a 1.25-cm pad in Fig. 66, and hence a 10% probability of multiple hits per struck pad.

7.3 Time-of-Flight Counters with Precision Time Resolution

For π-K separation, the time-of-flight difference over a path length L is

$$\Delta t[\mathrm{ps}] = \frac{L}{c}\left(\sqrt{1+M_K^2/P^2}-\sqrt{1+M_\pi^2/P^2}\right) \sim \frac{L}{c}\frac{M_K^2-M_\pi^2}{2P^2} \sim \frac{3.75L[\mathrm{cm}]}{P[\mathrm{GeV}/c]^2}.$$

We suppose that π-K separation is achieved if the resolution, σ_t, of the time-of-flight system is 1/2 of the time difference Δt. Table 10 summarizes the maximum momenta at which π-K separation is possible by this criterion, for two values of σ_t, and path lengths L relevant to the full BCD design. The time-of flight counters would be located at 200 cm from the beams

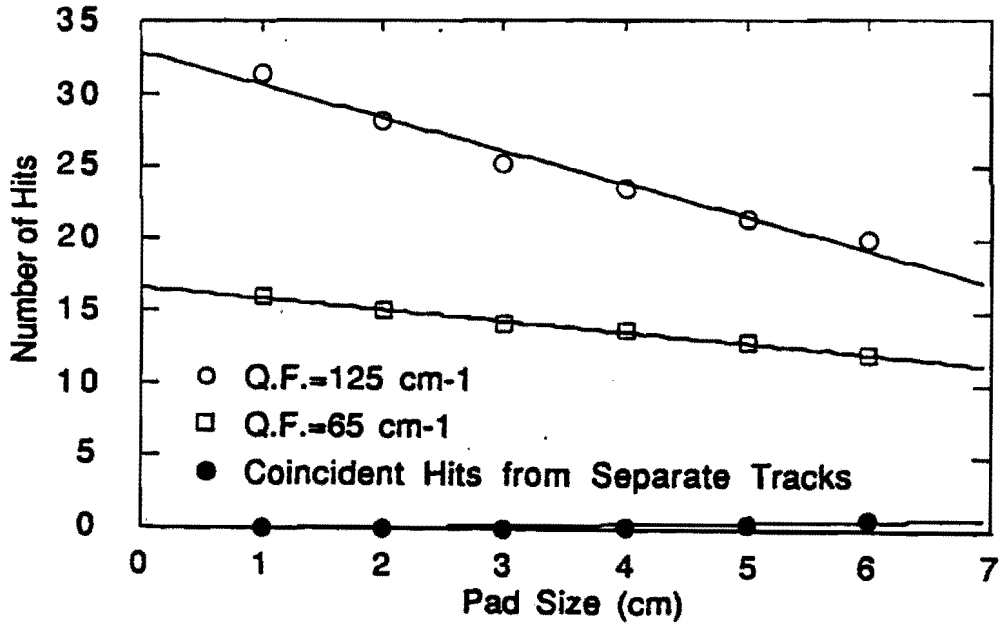

Figure 66: The number of pads in a RICH counter struck by only a single Čerenkov photon as a function of pad size.

in the Central region, so the flight path L is taken as (200 cm)/cos33.7°, noting that the highest-momentum particles occur at the smallest angle.

Table 10: The momentum coverage for π-K identification in the time-of-flight system, for two values of the timing resolution σ_t according to the criterion that $\Delta t = 2\sigma_t$.

Region	L (cm)	P_{max} (GeV/c) [σ_t = 50 ps]	P_{max} (GeV/c) [σ_t = 87 ps]
Central	240	3	2.3
Intermediate	730	5.2	4
Forward	2780	10.4	7.7

The needed timing resolution is primarily determined by the requirement that the time-of-flight system complement the capabilities of the RICH counter in the Intermediate region. There the minimum momentum at which π-K separation can be achieved in a gas RICH counter is about 4 GeV/c. This suggests that a resolution of at most 90 ps is needed. Improvement of this to 50 ps would yield a better match between a time-of-flight system

and the RICH counter in the Forward region, and such a resolution would provide π-K separation for 85% of all particles in the Central region.

A time resolution of 150 ps can be achieved in a single 3-4-cm-thick scintillator viewed by a single phototube.[78] Better resolution would be achieved with greater light collection, but if the scintillator is made thicker then the time spread due to the scintillation at different points along the charged particle's path limits the performance. Better time resolution can only be obtained by combining several samples in 3-4-cm-thick scintillator with appropriate delays to correct for the charged-particle transit time. These samples could be combined into a single phototube using isochronous light guides, or read out via multiple phototubes. The latter option, while more expensive, provides some protection against noise in that an inconsistent time signal among the set could be discarded.

The conjecture is that the time resolution in a set of n scintillators each 3-4 cm thick would vary as

$$\sigma_t = \frac{150 \text{ [ps]}}{\sqrt{n}}.$$

In this case we could achieve $\sigma_t = 87$ ps with $n = 3$ samples, and $\sigma_t = 50$ ps with $n = 9$.

A program to verify the possible improvements in timing resolution is now under way at SUNY Albany.[79] Three configurations of scintillators and phototubes, as shown in Fig. 67, are being tested with cosmic rays.

Earlier versions of the counters in Fig. 67a had only one phototube on each end and show r.m.s. time resolution of $\sigma_t = 110$ ps. With two phototubes on each end the number of scintillation photons doubles, and the time resolution improved to 85 ps. This compares well with the expectation of $110/\sqrt{2} = 78$ ps, using the simple statistical model.

The scintillation counter was then rotated by 90°, as shown in Fig 67b, so that the cosmic rays traversed 10 cm rather than 5 cm of scintillator as before. With twice the number of photons we might expect a resolution of $8r/\sqrt{2} = 60$ ps. A preliminary measurement indicates that $\sigma_t = 75$ ps.

The scintillation counter of Fig. 67c with eight phototubes will be tested soon. It is expected that a time resolution of 50 ps can be achieved with this configuration.

The scintillators used in these tests have been solid bars. Recent studies[80] suggest that somewhat superior timing performance in very long counters can be obtained with scintillating-fiber bundles. We will extend our studies to explore this in the near future.

7.4 Simulation of TRD Performance

In the full BCD experiment, transition radiation detectors (TRD) will augment the electron identification provided in part by the electromagnetic calorimeter. We have performed simulations of the π/e rejection that could be obtained in various TRD configurations subject to the constraint of 90% electron efficiency, and overall TRD thickness of 30 cm. By use of many thin radiator/detector modules and careful choice of the x-ray-energy threshold rather good π/e rejection should be attainable in a compact detector.

The simulation includes a statistical model of x-ray generation in the radiator foils, and of x-ray conversion in the gas of the x-ray detector. Table 11 lists the results of the simulation.

An electron signal consists of energy above threshold deposited in n or more of the N modules, where $n < N$. The threshold energy and minimum-module number n are chosen

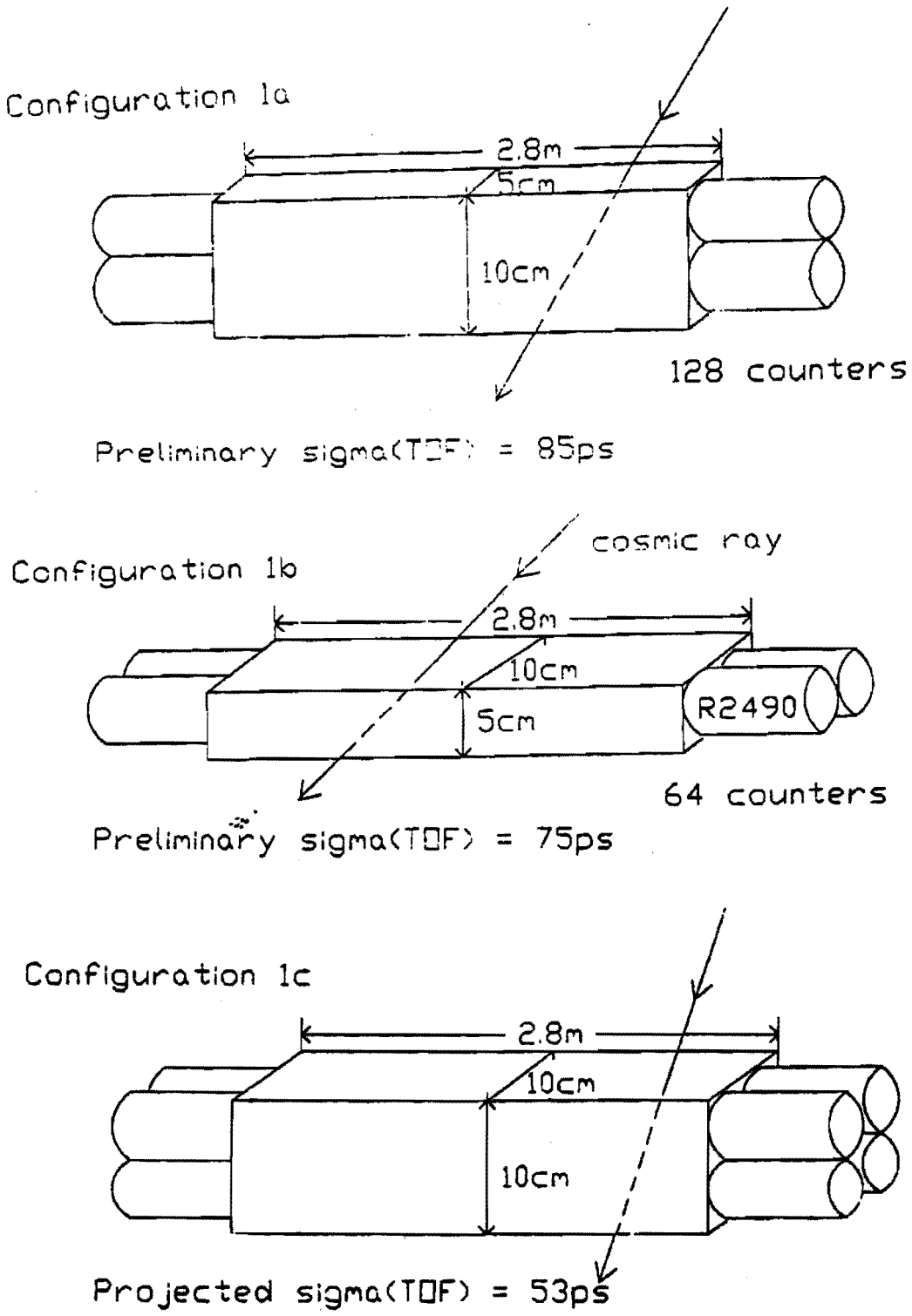

Figure 67: Three configurations of scintillation counters whose timing performance is being studied. Preliminary results indicate that excellent time resolution is possible with these devices.

Table 11: Simulated performance of a TRD of 30-cm total thickness. Each module includes a 6-mm-thick Xe detector and 5-mm thickness of packaging. For a trigger, energy above threshold is required in only a subset of the total number of modules. The electron efficiency is 90% in all cases.

Configuration	1	2	3	4	5	6	7
Radiator length (cm)	0.5	1.0	1.5	1.0	1.5	2.0	3.0
Foil thickness (μm)	12.7	12.7	12.7	25.4	25.4	25.4	25.4
No. of modules	19	14	11	14	11	9	7
X-ray threshold (keV)	4	10	8	10	10.5	10.5	11
No. of modules for e trig	11	4	4	5	4	4	3
π/e rejection	220	650	185	620	620	630	210

to maintain 90% efficiency in all cases. The π/e rejection is quite sensitive to the value of the x-ray energy threshold, but very good rejection is to be expected over a broad parameter space.

7.5 Efficiency of Lepton and Kaon Tags

We propose to determine the particle/antiparticle character of a fully reconstructed B meson via a tag on the second B in the event. The tag would be based on the sign of the lepton in a partial reconstruction of the decays $B \to l^{\pm}X$, or on the sign of the Kaon in $B \to K^{\pm}Y$. In both cases there is some probability of observing a wrong-sign lepton or Kaon due to secondary and tertiary decays. If the probability is p that a wrong-sign tag is made, then the statistic power of a sample of N tagged events is reduced to that of $N(1-2p)$ perfectly tagged events.

Since we only have to worry about the tagging quality when we have a fully reconstructed B, we can have confidence that any other secondary vertex in the event is that of the second B, even if the latter is only partially reconstructed. Hence we only examine the decays of the second B to estimate the mistagging probability p. For this we have generated a sample of 10^5 B's using ISAJET, and let them decay according to a representative sample of hadronic and semileptonic modes. The single-particle cuts described in Sec. 2 above are applied.

The P_t spectra of right-sign leptons (from the primary decay $b \to W^- \to l^-\nu$) and of wrong-sign leptons (from the secondary decay $b \to c \to W^+ \to l^+\bar{\nu}$, *etc.*) have already been shown in Fig. 6. There are actually about 1.5 times as many wrong-sign leptons as right sign, although the wrong-sign leptons have markedly lower P_t . The P_t spectrum of right-sign Kaons (from $b \to c \to s$ with the s-quark appearing in a Kaon) is shown in Fig. 68, and is essentially identical to that of wrong-sign Kaons (from $b \to W^- to\bar{c} \to \bar{s}$, or $b \to c \to W+ \to \bar{s}$, *etc.*). However, right-sign Kaons outnumber wrong-sign Kaons by 12 to 1 (in our ISAJET simulation).

In using the leptons (or Kaons) to determine the particle/antiparticle character of the

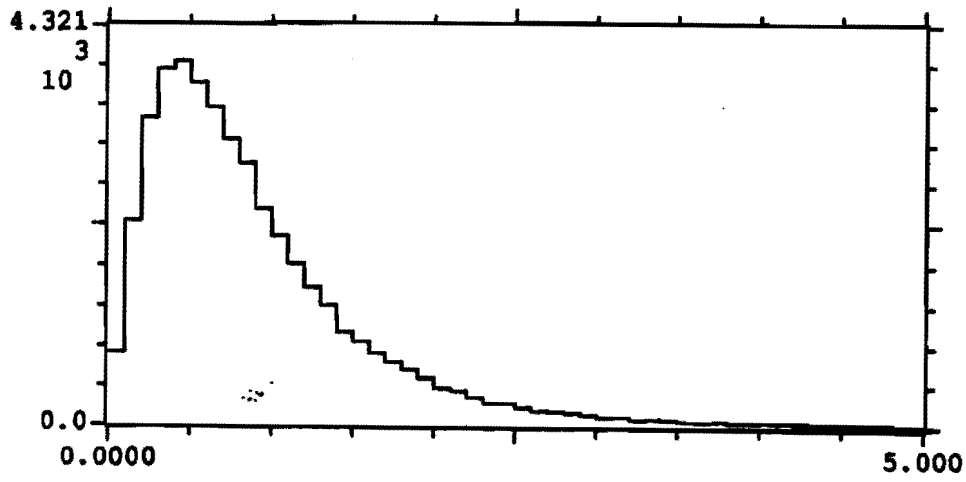

Figure 68: The transverse-momentum spectrum of right-sign Kaons from B-meson decay.

second B we simply look at the sign of the highest-P_t lepton (or Kaon). Only in a small fraction of the decays are there two leptons (or two Kaons) and we have made no attempt to devise a more sophisticated algorithm for this small subset.

Figure 69 shows the fraction of all leptons (or Kaons) at a given P_t that have the wrong sign. While at no P_t are wrong-sign Kaons a problem, for $P_t < 500$ MeV/c the wrong-sign leptons dominate the right-sign. That is, the lepton tag is worthless at $P_t = 500$ MeV/c. For P_t less than this we can change our definition of 'right' and 'wrong' and obtain some useful tags.

The effectiveness of the tags is presented another way in Fig. 70. The quantity $N\,|1-2p|$, the effective number of useful events, is plotted as a function of P_t in the left-hand plots. The right hand plots show the integral

$$\int_{P_t}^{\infty} dN\,|1-2p|\,.$$

The integrals have been normalized to the total number of B's, and so represent the efficiency of a tag as a function of the minimum-P_t cut.

The Kaon tag will be about 10 times as useful as the lepton tag. However, the Kaon tag is not readily associated with a trigger for the experiment, in contrast with the leptons tags.

The efficiency of the lepton tags increases only slightly as the P_t cut is lowered below 1 GeV/c, due to the abundance of low-P_t wrong-sign leptons. A way around this is to use a combined lepton and Kaon tag, requiring both a right-sign lepton and Kaon. Row three of Fig. 70 shows how for very low P_t this tag becomes more efficient than a lepton tag alone, although at high P_t it is only 1/2 as efficient. The combined lepton and Kaon tag is superior from the point of view of immunity to backgrounds we have not considered here.

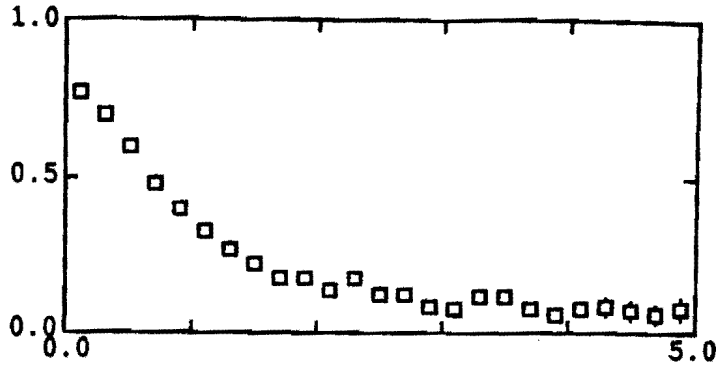

wrong sign e fraction vs PT

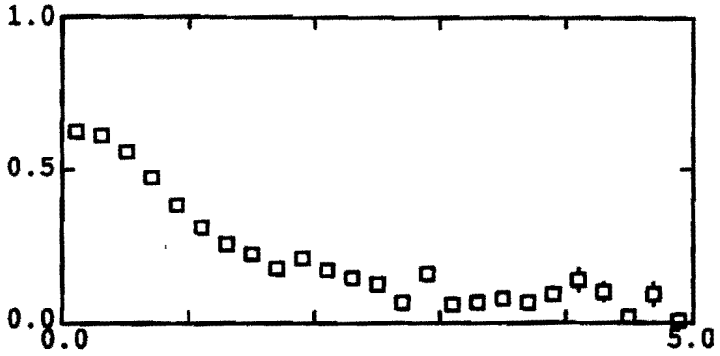

wrong sign mu fraction vs PT

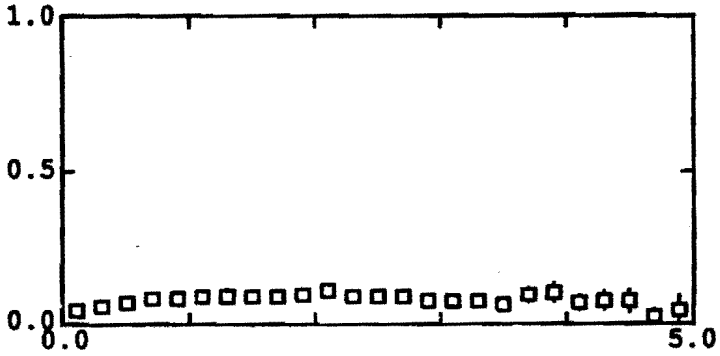

wrong sign K fraction vs PT

Figure 69: The fraction of leptons (or Kaons) that have the wrong sign as a function of P_t .

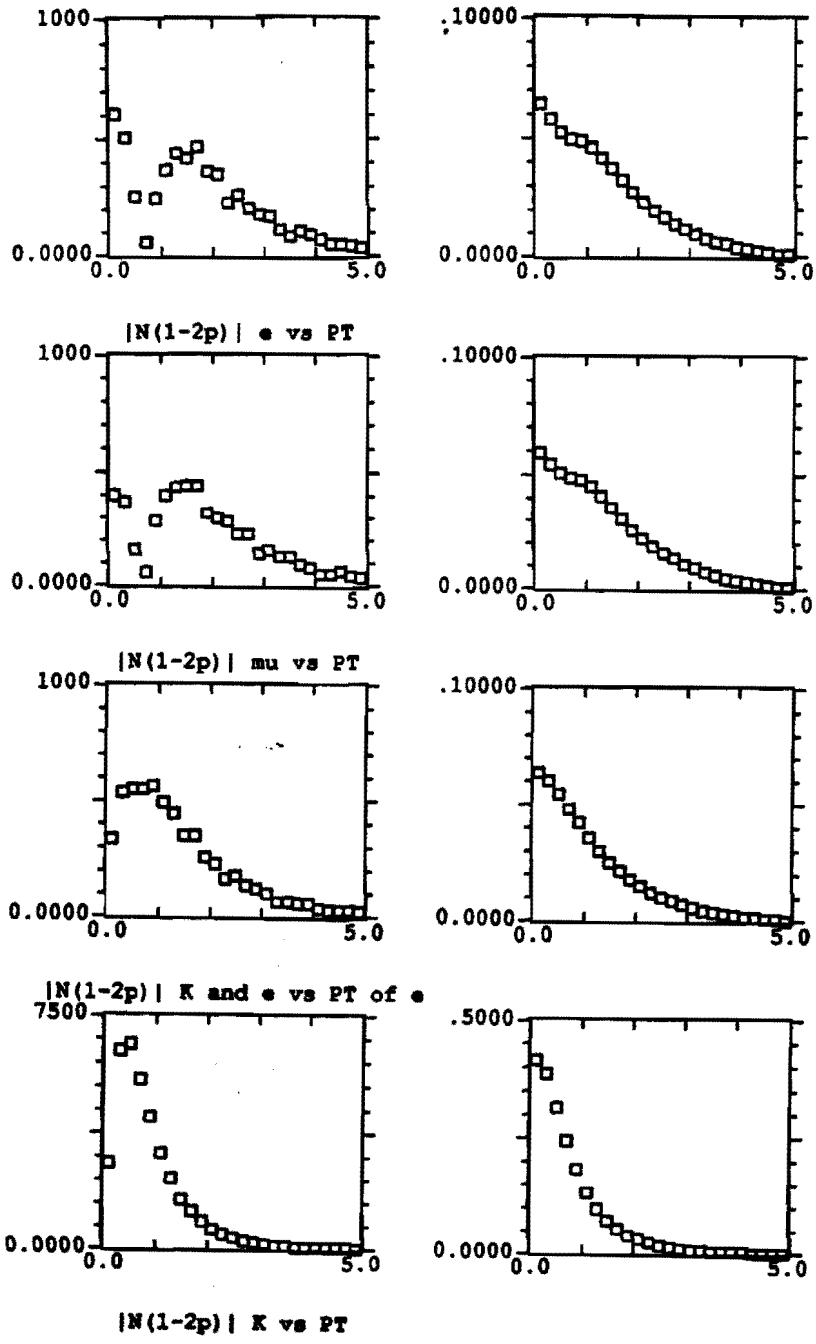

Figure 70: Differential and Integral tagging efficiencies of four types of tags as a function of transverse momentum. Left hand plots: the number $N\,|1-2p|$ of useful tagged events, right-hand plots: the total efficiency of the tag as a function of the minimum-transverse-momentum requirement. The four tags are, from top to bottom, electron, muon, combined electron and Kaon, and Kaon.

8 Appendix D: High-Rate Data-Acquisition System

The BCD Collaboration proposes a high-rate data-aquisition system of a somewhat different architecture and much greater data-handling rate than that of any existing experiment. Although novel to the high-energy-physics community, the high-speed digital technology required is less speculative than the high-performance detectors also proposed for the BCD.

We review this data-acquisition architecture below before reporting progress on prototypes of the event-builder switch by E. Barsotti, A. Booth, M. Bowden, and coworkers in the Computing Division at Fermilab, and on studies of the data flow into a networked processor farm by P. Keener and N. Lockyer of U. Penn.

8.1 Overview

The rate of B-$\bar{B}$ production at the TEV I at a luminosity of 10^{32} cm^{-2}sec^{-1} is 4 kHz, which is 0.1% of the total interaction rate of 4 MHz. The experimental trigger should not be overly restrictive if we wish to collect the large sample of B decays needed for studies of CP violation. Because of the low mass scale of the B's they occur in events kinematically similar to 'minimum-bias' events. An efficient B trigger will therefore also accept a fraction of the minimum bias events. Hence the data-acquisition system will need to have very high rate capability by present standards.

We propose an architecture[81, 82] in which a single level of prompt triggering provides only a modest reduction in the event rate in 1.5-2 μsec, and a large online computer farm[83] implements software triggers based on correlations of full-resolution data from several subsystems of the detector. This is shown in Fig. 71, in which the data flow is from the bottom to the top. Both the prompt trigger and the software triggers should provide reduction factors of order 100, so that approximately 1000 events per second out of 4×10^6 are archived.

The event size is expected to be about 0.5 MByte, so the $\sim 10^5$ events/sec passing the prompt trigger lead to a data-flow rate of about 50 GBytes/sec off the detector into the computer ranch. The archival data rate is also quite substantial: 0.5 GByte/sec = 2 TeraBytes/hour.

8.1.1 Data-Acquisition Architecture

The data-acquisition architecture is shown in Figs. 71 and 72. Briefly, the data from each detector subsystem is stored locally in analog-storage buffers about 100-events deep during the 1.5-2 μsec while the prompt trigger is being formed. If an event satisfies the prompt trigger, its data are moved to a second level of storage while the data are digitized and transmitted to the processor farm. The digitization will take place on the detector (local VLSI ADC's) for most subsystems. In addition, local processing leading to data compaction may take place.

The data are driven from the detector on $\sim$ 1000 fiber-optic cables to the processor ranch at a rate of up to 500 GBytes/sec. Drivers for such data rates are commercially available today. However, this data rate is several orders of magnitude higher than in existing high-energy-physics experiments.

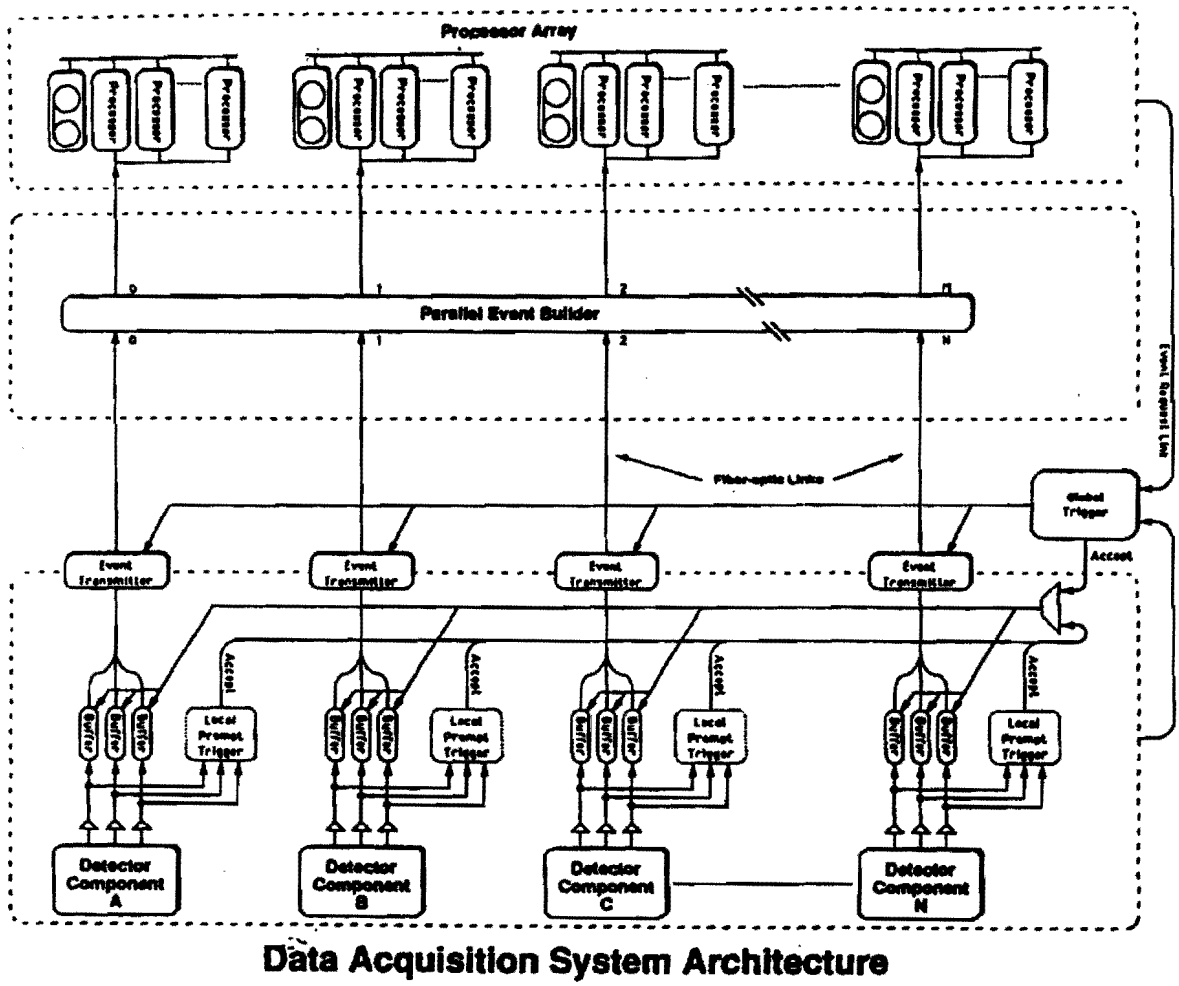

Figure 71: Data-acquisition-system architecture, I.

Before the events can be processed, the $\sim$ 1000 parallel event streams must be organized into the events themselves. This might be accomplished in either of two ways; in a special-purpose event-builder switch based on telecommunications technology,[84] or in the switching network of the processor farm itself should this network have sufficient bandwidth.

The special-purpose event builder is based on the 'barrel-switch' concept illustrated in Fig. 73. The event fragments on the input lines at the left are delayed by one clock cycle on each successive line. Then at every clock cycle, the switch rotates its contacts by one line, so that the fragments of one event on n input lines are all ordered serially on a single output line after n cycles. In the meanwhile, $n-1$ later events are in various stages of building. The switch required for the BCD would have a capability similar to that of a single 10,000-line telephone exchange.

In any case, the processor farm itself must have a powerful network connecting the processors so that data may be sent in and out of the farm at high rate. A sketch of such

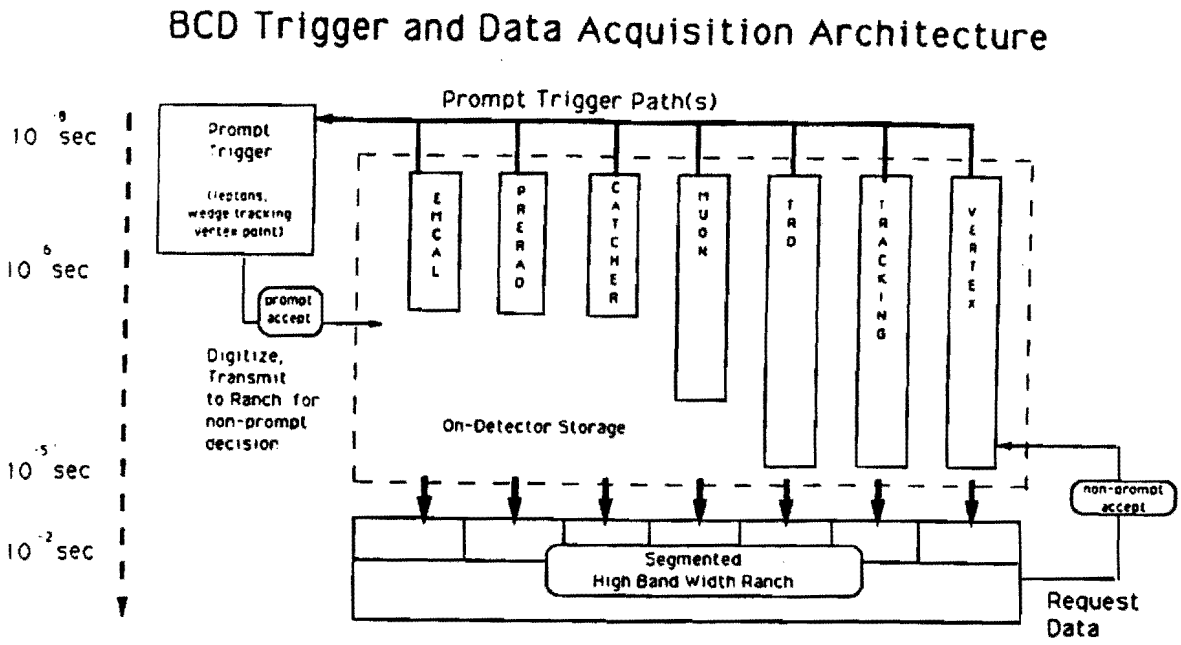

Figure 72: Data-acquisition-system architecture, II.

a processor network is shown in Fig. 74. The numerical processors are located at most, but not all, of the nodes of the network. Some nodes are reserved for data input and output. Various topologies of the processor and I/O nodes are possible, and are under study by us.[16] One possibility is that the input nodes could be connected directly to the detector, and the sophisticated routing capability of the network performs the event-building function described above.

8.1.2 Online Processing Requirements – One TeraOPS

Some 10^5 events/sec must be processed by the computer farm in full-luminosity operation of the BCD. From the experience of the CDF collaboration, a software trigger will require at least 10 sec of computing time on a 1 MOPS processor. If this number is also relevant for the BCD, we will need 10^6 MOPS/sec = 1 TeraOPS of processing power.

8.1.3 Processor-Farm Architecture

The simplest use of processors on the computer ranch is to have each processor executing an identical program that analyzes a single event.

A more sophisticated architecture may be preferable. Here the processor nodes are dedicated to specific tasks and do not attempt to resolve complete events and make a final trigger decision by themselves. Only part of an event is built for a particular processor, much of the event data remaining on the detector (in large buffers) until a partial software-trigger decisions calls for more of the event. Blocks of processors may be assigned to the several types of

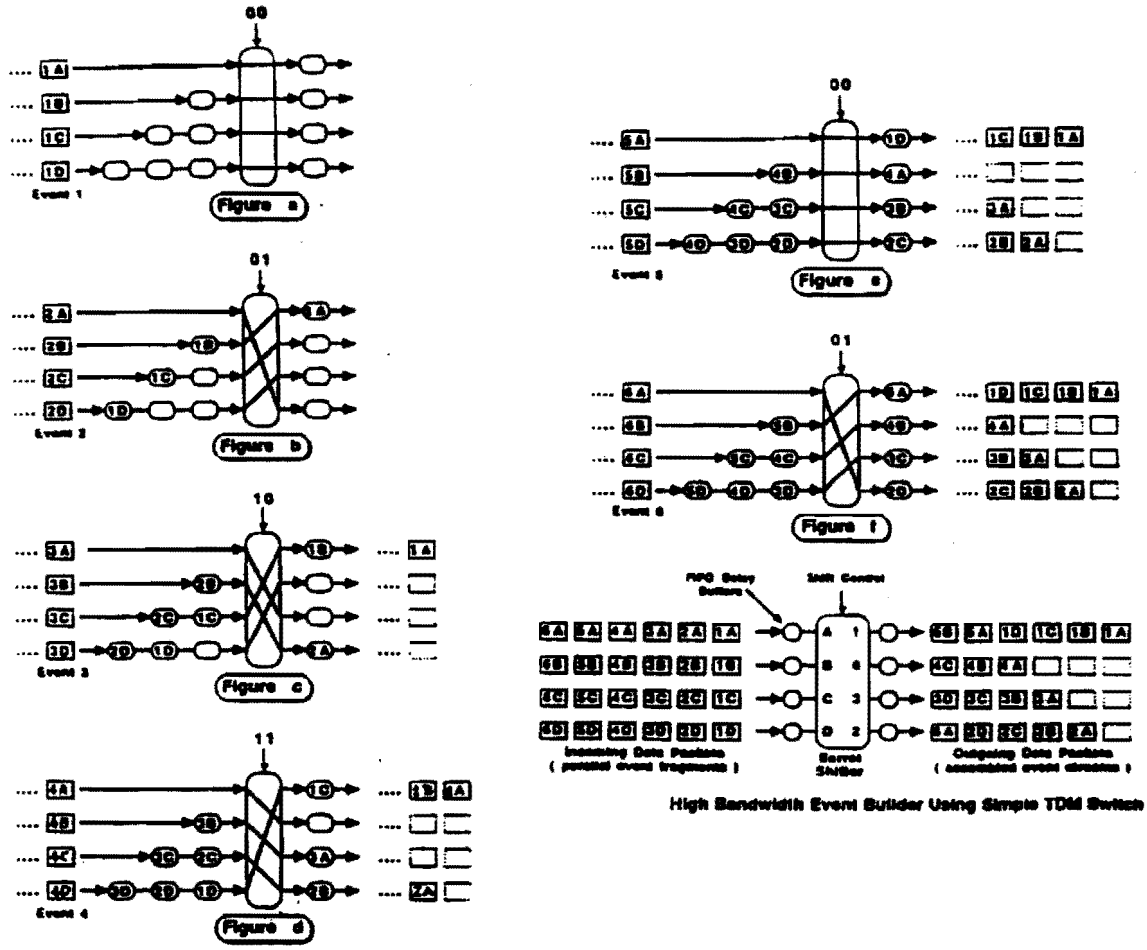

Figure 73: Principle of the barrel-switch event builder. See text for discussion.

triggers being implemented simultaneously. Some processors may carry their analysis much further than the others to provide detailed online monitoring.

Such an architecture, as well as the advanced networking capability to permit the distributed event-building sketched in Fig. 74, are within the scope of the ongoing Intel/DARPA Touchstone Project. A multiprocessor farm with combined performance of $\sim 100 GigaFLOPS$ is to be delivered in 1991. The processors will be connected on a high-bandwidth 2-dimensional mesh network with so-called wormhole routing. Such systems are well suited to the emerging needs of high-energy-physics experiments and to the BCD in particular.

8.1.4 Archival Mass Storage

The BCD anticipates recording at least 100 MBytes/sec to tape. With a compressed event size of 100k Bytes, 1 kHz of events could be recorded using contemporary (Exabyte) tech-

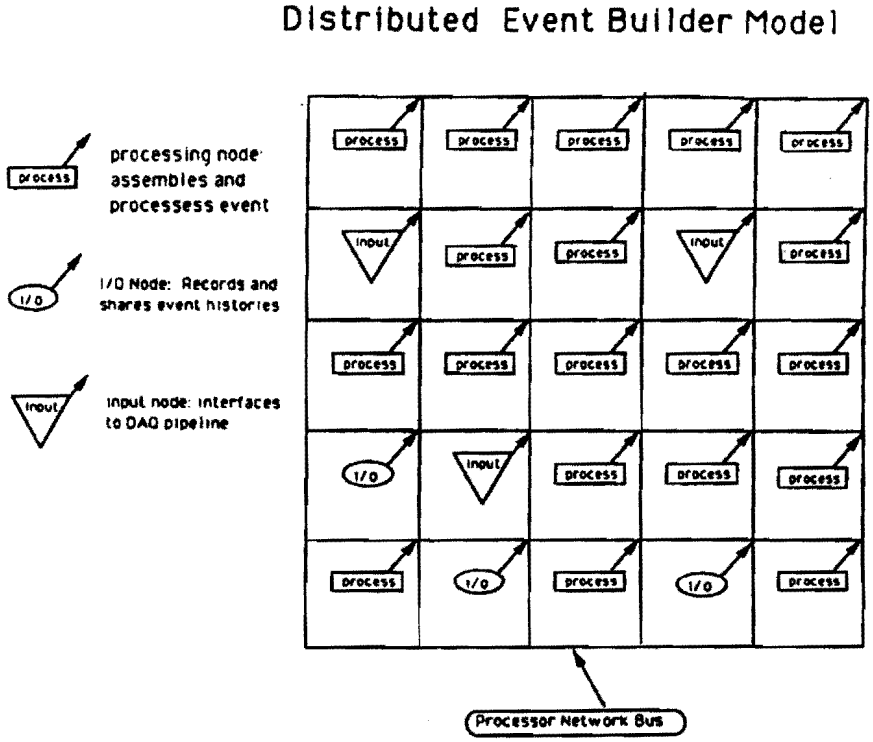

Figure 74: A possible network architecture for the processor farm. Complete events could be injected into the network at various I/O nodes and routed to available processors (Injector Model). Alternatively, the fragments of an event could be delivered to the several I/O nodes and the routing network used to assemble the fragments into a complete event at the target processor (Distributed Event-Builder Model).

nology. It is generally felt that 500 MBytes/sec would be an upper limit on the data archival rate due to sheer volume of data.

The E-Systems Garland Division has proposed a robotized data-acquisition archival configuration which would satisfy these requirements. This configuration uses 19-mm helical-scan digital-video cartridges with a capacity of up to 190 GBytes/cassette and data transfer rates of 15-30 MBytes/sec. In a year's running at 100 MBytes/sec, it is estimated that 1555 TeraBytes of data would be accumulated, requiring 2295 ft^2 of robotized floor area.

8.1.5 Offline Computing Needs

The BCD requires sufficient offline computing resources to maintain a data-analysis rate equal to the archival data-acquisition rate on an annual basis. It is assumed that the online computer will be active calibrating detector subsystems, recording data and thus will be largely unavailable for offline analysis. Extrapolating from the CDF experience, the amount of computing needed to run BCD data through production analysis is about 10–50 GFlops

to handle a data rate of 100 MBytes/sec to tape.

8.2 Event-Builder-Switch Prototype

A prototype of an 8 × 8 channel event-builder switch is now being constructed, and should be completed in early 1991.

The prototype has been designed conservatively to test all data-acquisition and event-building concepts in the new DAQ architecture. The data rates per (optical-fiber) cable are 20 MBytes/sec. The 8 × 8 prototype can thus have a maximum throughput of 160 MBytes per second (sufficient to build 1000 events/sec at the μBCD). The prototype occupies only 1/8 of a crate.

The system is readily expanded to a full crate of 64 channels with a total bandwidth of 1.28 GigaBytes/sec. All these throughputs are based on ideal balanced loads on each input. Load-balancing circuitry upstream of the event-builder switch is required for optimum performance.

A second-generation switch could be built in 1992 with 100 MBytes/sec per channel and 128 channels per crate for a maximum throughput of 12.8 GigaBytes/sec. A larger-capacity system would have $2N$ event-builder crates where N is the (desired maximum throughput)/(12.8 GigaBytes/sec). For example, a 100-GByte/sec switch will require 8 crates.

8.3 Testing Network I/O Architectures

Commercial interest in high-performance processors is very high and exciting developments will continue without any interaction with the high-energy-physics community. However, when large numbers of these processors are brought to bear on a single application, the nature of the interprocessor network will become a limiting factor to overall performance.[85] There may not be a single network architecture that is optimal for all applications, so that interested users can influence the effective computing power of the future by understanding their networking needs in collaboration with industry.

Intel Scientific Computers is the commercial vendor that has shown the greatest interest in networking issues that appear relevant to online processor farms in high-energy-physics experiments. As part of their Touchstone Project, funded by DARPA, they are building a high-bandwidth mesh network for processor interconnections that includes multiple high-speed I/O channels. We are interacting with Intel to explore the optimization of these I/O channels for high-energy physics.

The Intel high-bandwidth mesh network is not yet available, but we are fortunate to have access to their currently supported network, the Intel IPSC/2 hypercube, that is the basis of a 32-node farm of *i860* processors in the Division of Applied and Computational Mathematics at Princeton U.

Tests are being made of three configurations of I/O into the hypercube.

Figure 75 shows the connection of a VME I/O interface to a special-purpose device called an I/O node that resides on the hypercube network. This is the standard I/O configuration supported by Intel, and allows the data to be routed to any specified processor. It uses two additional modules to make the connection: a Direct-Connect Routing Module (DCM)

that makes the actual connection to the network and includes local buffering, and the iLBX module which is a local bus originally designing for tightly connecting two computing nodes independent of the hypercube network.

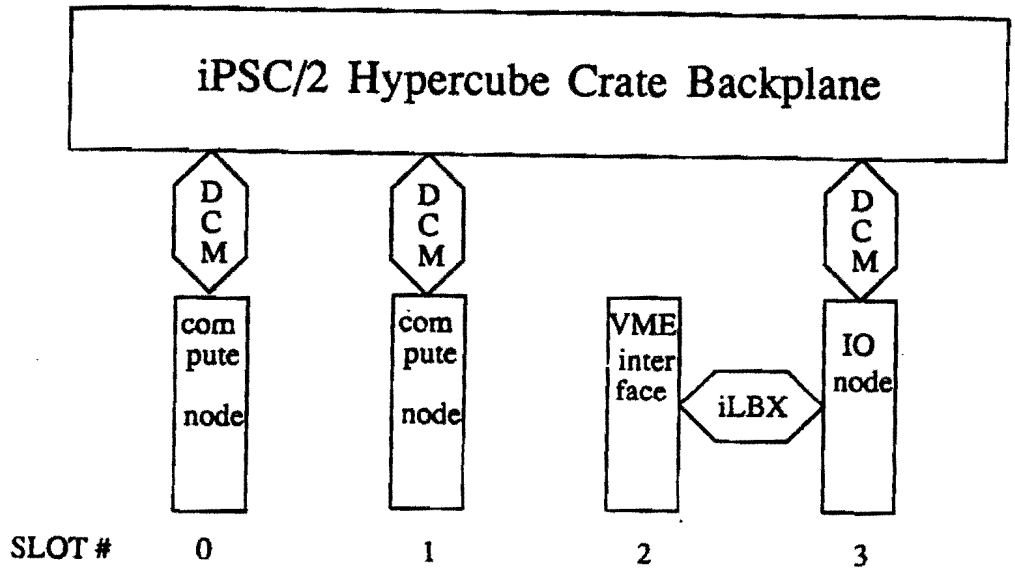

Figure 75: The standard configuration of I/O into an Intel iPSC/2 Hypercube network. The VME interface first connects to the iBLX bus that connects to a special I/O node. All nodes are buffered from the network by Direct-Connect Routing Modules (DCM). Data entering the I/O node can be routed to any other node.

If an external switch has already routed the data from an entire event onto one of n input lines, it could be more effective to tie that line directly to the processor that will analyze the data. The processor must, of course, have sufficient memory to buffer several incoming events. Figure 76 shows a configuration in which the VME interface is connected directly to a compute node via the iBLX bus.

An interesting alternative is to use the processor-farm network as an event builder, injecting only fragments of an event at each of several I/O nodes, and letting the sophisticated routing of the network organize the fragments into whole events delivered to an available processor. This will place great demands on the bandwidth of the network, and would benefit from a more direction I/O connection to the network than that shown in Fig. 75. Figure 77 shows a direct connection of the VME interface card to DCM, which should allow higher throughput. This requires a hardware modification to the current Intel design of the VME interface.

All three I/O configurations are current under study by us, both in hardware, and in Verilog software simulations.[88] Evolution beyond the standard I/O configuration is likely to occur only as a result of such effort by users outside Intel. However, Intel has expressed interest is providing hardware support for new I/O configurations.

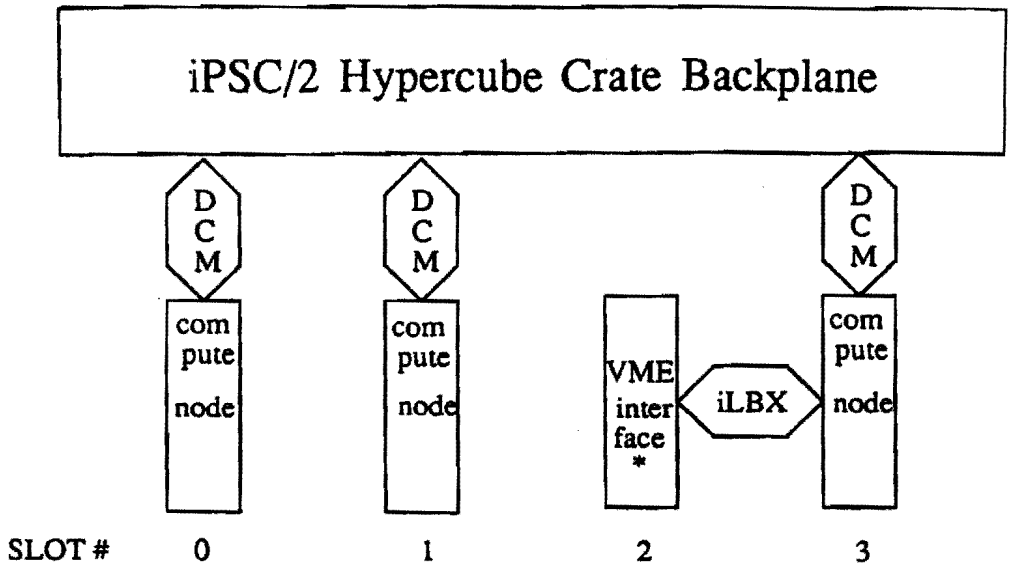

Figure 76: A configuration of I/O into an Intel iPSC/2 Hypercube network in which data flows directly into a compute node. This is advantageous if an external switch has already routed the data to the proper node.

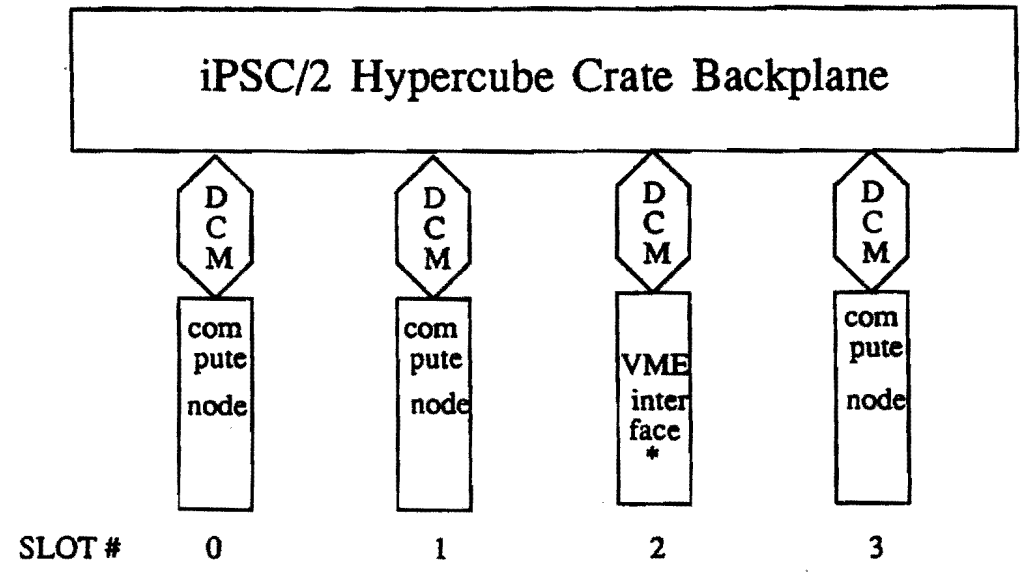

Figure 77: A configuration of I/O into an Intel iPSC/2 Hypercube network in which the data interfaces more directly to the network. This is advantageous if the advanced routing capability of the network is to be used to perform event building .

9 References

[1] E. Fernandez *et al.*, *Lifetime of Particles Containing b Quarks*, Phys. Rev. Lett. **51**, 1022 (1983).

[2] N.S. Lockyer *et al.*, *Measurement of the Lifetime of Bottom Hadrons*, Phys. Rev. Lett. **51**, 1316 (1983).

[3] P. Nason, S. Dawson, and R.K. Ellis, *The Total Cross Section for the Production of Heavy Quarks in Hadronic Collisions*, Nucl. Phys. **B303**, 607 (1988); *The One Particle Inclusive Differential Cross Section for Heavy Quark Production in Hadronic Collisions*, Nucl. Phys. **B327**, 49 (1989).

[4] H. Albrecht *et al.*, *Observation of B^0-$\bar{B}^0$ Mixing*, Phys. Lett. **192B**, 245 (1987);

[5] M. Artuso *et al.*, *$B^0\bar{B}^0$ Mixing at the $\Upsilon(4S)$*, Phys. Rev. Lett. **62**, 2233 (1989).

[6] P. Karchin, N.S. Lockyer *et al.*, *Proposal for a Bottom Collider Detector* **BCD**, (March 1987).

[7] N.W. Reay *et al.*, *Letter of Intent for a Tevatron Beauty Factory*, (March 1987).

[8] N.W. Reay *et al.*, *Summary of the Collider Architecture Working Group*, Proceedings of the Workshop on High Sensitivity Beauty Physics at Fermilab, J. Slaughter, N. Lockyer, M. Schmidt, eds. (Nov. 11-14, 1987), p. 253.

[9] H. Castro *et al.*, *Letter of Intent for the BCD, A Bottom Collider Detector for the Fermilab Tevatron*, (October 7, 1988).

[10] H. Castro *et al.*, *Proposal for Research and Development: Vertexing, Tracking and Data Acquisition for a Bottom Collider Detector*, submitted to the Fermilab PAC (Jan. 2, 1989).

[11] S. Dhawan *et al.*, *Performance Limits of Silicon Strip Front-end Electronics for the SSC Bottom Detector*, SSC Generic R&D Proposal (1988); *Mechanical Structures for Microvertex Detectors*, SSC Generic R&D Proposal (1988).

[12] E. Barsotti *et al.*, *Proposal for Generic Detector R&D for the SSC* (Processor Farms), (1988).

[13] E. Barsotti *et al.*, *Proposal for Generic Detector R&D for the SSC* (Event Builder), (1988).

[14] K.T. McDonald and M.V. Purohit *Proposal for Generic Detector Development (Silicon Drift Chambers)*, (August 31, 1988); C. Lu *et al.*, *Proposal for Generic Detector Development in FY 1990 (Silicon Drift Chambers)*, (June 1, 1990).

[15] G.R. Kalbfleisch *et al.*, *A Proposal to Investigate Radiation Hardened Semiconductor Device Technologies for Use with Silicon Strip Detectors at the SSC*, (1988)

[16] L.D. Gladney *et al.*, *Proposal to SSC Laboratory for Research and Development for a Parallel Computing Farm*, (Sept. 29,1989); *Subsystem Renewal Proposal to SSC Laboratory for R&D of a Parallel Computing Farm*, (Sept. 11, 1990).

[17] C. Lu *et al.*, *Proposal to the SSC Laboratory for Research and Development of a Straw-Tube Tracking System*, (Sept. 30, 1989); B. Brabson *et al.*, *SSC Detector Subsystem Summary Report and Proposal for FY 1991 (Central and Forward Tracking)*, (August 31, 1990).

[18] E. Arens *et al.*, *SSC Detector R&D Proposal: Development of Technology for Pixel Vertex Detector*, (Oct. 1, 1989).

[19] W. Chen *et al.*, *SSC Detector Subsystem R&D Proposal to Develop Track and Vertex Detector Based on Silicon Drift Devices*, (Oct. 1, 1989); *SSC Detector Subsystem R&D Interim Report on Silicon Drift Devices for Tracking and Vertex Detection*, (Sept. 1, 1990).

[20] B. Hoeneisen *et al.*, *Proposal for R&D on a Ring Imaging Čerenkov (RICH) Detector Subsystem*, (Sept. 1, 1990).

[21] BCD Collaboration, *Bottom Collider Detector Expression of Interest*, submitted to the SSC (May 25, 1990).

[22] BCD Collaboration, *Response to the SSC PAC*, (July 11, 1990).

[23] J.G. Heinrich and K.T. McDonald, *B-Physics Options at TEV I*, Princeton U. preprint DOE/ER/3072-61 (August 10, 1990).

[24] For an extensive discussion, see Section 2 of ref. [21].

[25] R.L. Gluckstern, *Uncertainties in Track Momentum and Direction Due to Multiple Scattering and Measurement Errors*, Nucl. Instr. and Meth. **24**, 381 (1963).

[26] B. Hoeneisen, D.F. Anderson and S. Kwan, *A CsI-TMAE Photocathode with Low-Pressure Readout for RICH* FERMILAB-Pub-90/182 (Sept. 1990).

[27] M. Bauer, B. Stech, and M. Wirbel, *Exclusive Non-Leptonic Decays of D-, D_s-, and B-Mesons*, Z. Phys. C **34**, 103 (1987).

[28] P. Krawczyk, D. London, R.D. Peccei, and H. Steger, *Predictions of the CKM Model for CP Asymmetries in B Decay*, Nucl. Phys. **B307**, 19 (1988).

[29] G. Bélanger *et al.*, *Weak Decays: Theoretical Summary*, Proceedings of the Summer Study on High Energy Physics in the 1990's (Snowmass, 1988) S. Jensen, editor, p. 339.

[30] C. Bernard *et al.*, Phys. Rev. D **38**, 3540 (1988).

[31] The relevant box diagram was first calculated by J. Ellis, M.K. Gaillard, and D.V. Nanopoulos, *Left-Handed Currents and CP Violation* Nucl. Phys. **B109**, 213 (1976). That this leads to p/q being a pure phase and very small $|\epsilon_B|$ seems to have been first noticed by J.S. Hagelin, *Weak Mass Mixing, CP Violation, and the Decay of b-Quark Mesons*, Phys. Rev. D **20**, 2893 (1979).

[32] First discussed by A.B. Carter and A.I. Sanda, *CP Nonconservation in Cascade Decays of B Mesons*, Phys. Rev. Lett. **45**, 952 (1980); *CP Violation in B-Meson Decays*, Phys. Rev. D **23**, 1567 (1981).

[33] I.I Bigi and A.I. Sanda, *Notes on the Observability of CP Violations in B Decays*, Nucl. Phys. **B193**, 85 (1981).

[34] First introduced by L. Miani, *CP Violation in Purely Lefthanded Weak Interactions*, Phys. Lett. **62B**, 183 (1976); our notation follows L. Wolfenstein, *Parametrization of the Kobayashi-Maskawa Matrix*, Phys. Rev. Lett. **51**, 1945 (1983).

[35] First discussed in L.-L. Chau and W.-Y. Keung, *Comments on the Parametrization of the Kobayashi-Maskawa Matrix*, Phys. Rev. Lett. **53**, 1802 (1984).

[36] R. Yarema, *BVX Workshop Summary*, BCD-RP-207 (Nov. 28, 1989).

[37] G. R. Kalbfleisch and K. T. McDonald, *Configuration of Silicon Vertex Detector*, BCD-P-010 (April 16, 1988).

[38] H. Mulderink, N. Michels, and H. Jöstlein, *Mechanical and Thermal behavior of a Prototype Support Structure for a Large Silicon Vertex Detector (BCD)*, Fermilab TM-1616 (August 23, 1989).

[39] H. Jöstlein and J. Miller, *Heat Resistance and Air Pressure Drop in a Model of the BCD Silicon Vertex Detector*, BCD Internal Note RP-211 (Jan. 9, 1990).

[40] H. Jöstlein and H. Mulderink, *Continued Studies of the Mechanical and Thermal behavior of a Prototype Support Structure for a Large Silicon Vertex Detector (BCD)*, Fermilab TM-1685 (Oct. 1990).

[41] C. Lindenmeyer, *Proposed Method of Assembly for the BCD Silicon Strip Vertex Detector Modules*, Fermilab TM-1627 (Oct. 16, 1989).

[42] H. Attias *et al.*, *Beam Tests of Silicon Microstrip Detectors with VLSI Readout*, submitted to the SSC Detector Symposium (Ft. Worth, Oct. 1990).

[43] J.G. Jernigan *et al.*, *Performance Measurements of Hybrid p-i-n Diode Arrays*, presented at the 1990 International Industrial symposium on the Super Collider, (Miami Beach, Mar. 14-19, 1990).

[44] L.A. Roberts, *Monte Carlo Simulation of Silicon Vertex Detector for Bottom Collider Detector*, Fermilab preprint FN-488 (June, 1988).

[45] P. Lebrun, *A Bottom Collider Vertex Detector Design Monte Carlo Simulation and Analysis Package*, Fermilab TM-1682 (October 1,1990).

[46] C. Lu *et al.*, *Prototype Study of the Straw Tube Proportional Chamber*, Princeton U. preprint DOE/ER/3072-56 (Feb. 15, 1990).

[47] C. Lu and K.T. McDonald, *A Straw-Tube Tracking System for the SSC*, to appear in the Proceedings of the IISSC (Miami, Mar. 14-16, 1990).

[48] C. Lu and K.T. McDonald, *Drift-Chamber Timing Studies with a N_2 Laser*, Princeton U. preprint DOE/ER/3072-60 (June 10, 1990).

[49] W.S. Anderson *et al.*, *Addendum to the Progress Report and Renewal Request for R&D on Central and Forward Tracking*, Princeton U. (Sept. 4, 1990).

[50] M. Frautschi *et al.*, *The AMY Inner Tracking Chamber*, Ohio State U. preprint (Oct. 1989), submitted to Nucl. Instr. and Meth.

[51] J.L. Pack and A.V. Phelps, *Drift Velocities of Slow Electrons in Helium, Neon, Argon, Hydrogen and Nitrogen*, Phys. Rev. **121**, 798 (1961).

[52] G.S. Hurst and J.E. Parks, *Time-of-Flight Determinations of Electron Diffusion Coefficients and Electron Drift Velocities in Ethylene, Water Vapor, and in Hydrogen*, J. Chem. Phys. **45**, 282 (1966).

[53] J. Va'vra, *The Use of a Nitrogen Laser for Observation of Space Charge Effects in Drift Chambers and Development of High Precision Vertex Chambers*, Nucl. Instr. and Meth. **225**, 13 (1984).

[54] K.W.D. Ledingham *et al.*, *Laser Induced Ionization in Proportional Counters Seeded with Low Ionization Potential Vapours*, Nucl. Instr. and Meth. **225**, 319 (1984).

[55] UA1 Collaboration, *A Laser Calibration Scheme for the UA1 Central Detector at High Luminosity (ACOL)*, Nucl. Instr. and Meth. **A263**, 26 (1988).

[56] J. Bourotte and B. Sadoulet, *Ionization of Multiwire Proportional Chamber Gas by Double Photon Absorption*, Nucl. Instr. and Meth. **173**, 463 (1980).

[57] V. Palladino and B. Sadoulet, *Application of Classical Theory of Electrons in Gases to Drift Proportional Chambers*, Nucl. Instr. and Meth. **128**, 323 (1975).

[58] F. Pius, *Measurement of the Longitudinal Diffusion of a Single Electron in Gas Mixtures Used in Proportional Counters*, Nucl. Instr. and Meth. **205**, 425 (1983).

[59] B. Jean-Marie *et al.*, *Systematic Measurement of Electron Drift Velocity and Study of Some Properties of Four Gas Mixtures: A-CH_4, A-C_2H_4, A-C_2H_6, A-C_3H_8*, Nucl. Instr. and Meth. **159**, 213 (1979).

[60] L.G. Christophrou *et al.*, *Fast Gas Mixtures for Gas-Filled Particle Detectors*, Nucl. Instr. and Meth. **163**, 141 (1979).

[61] J. Fischer *et al.*, *Proportional Chambers for Very High Counting Rates Based on Gas Mixtures of CF_4 with Hydrocarbons*, Nucl. Instr. and Meth. A238, 249 (1985).

[62] T. Yamashita *et al.*, *Measurements of the Electron Drift Velocity and Positive Ion Mobility for the Gases Containing CF_4*, Preprint.

[63] J. Va'vra, *Search for the Best Timing Strategy in High Precision Drift Chambers*, Nucl. Instr. and Meth. **225**, 445 (1985).

[64] G.F. Knoll, *Radiation Detection and Measurement*, 2nd ed., (John Wiley & Sons, New York, 1989).

[65] M.C. Lundin, *Study of Drift Tube Resolution Using Numerical Simulations*, Fermilab TM-1680 (Sept. 1990).

[66] Proceedings of the SLC Workshop on Experimental Use of the SLAC Linear Collider, SLAC-247 (March, 1982), p. 158.

[67] J. Sequinot and T. Ypsilantis, *Photo-ionization and Čerenkov Ring Imaging*, Nucl. Instr. and Meth. **142**, 377 (1977).

[68] See *e.g.*, M. Adams *et al.*, *$\pi/K/p$ Identification with a Large-Aperture Ring-Imaging Čerenkov Counter*, Nucl. Instr. and Meth. **217**, 237 (1983); R.J. Apsimon *et al.*, *A Ring Imaging Čerenkov Detector for the CERN Omega Spectrometer*, IEEE Trans. Nucl. Sci. **NS-32**, 674 (1985); D.W.G.S. Leith, *Status of Čerenkov Ring Imaging*, Nucl. Instr. and Meth. **A265**, 120 (1988).

[69] G. Charpak, V. Peskov, and D. Scigocki, *Study of BaF_2 Calorimeters in Future Hadron Colliders*, CERN-EP/90-41, CERN/LAA/EC/90-005 (4 April 1990), presented at the 8th Workshop of the INFN-ELOISATRON Project on Perspectives for New Detectors in Future Supercolliders (Erice, 17-24 Oct. 1989).

[70] J. Sequinot *et al.*, *Reflective UV Photocathodes with Gas-Phase Electron Extraction: Solid, Liquid, and Adsorbed Thin Films*, CERN-EP/90-88 (20 June 1990), submitted to Nucl. Instr. and Meth.

[71] R. Chechik and A. Breskin, *On the Properties of Low-Pressure TMAE-Filled Multistep UV-Photon Detectors*, Nucl. Instr. and Meth. **A264**, 251 (1988); A. Breskin, Weizmann Institute preprint (1989).

[72] V. Dangendorf *et al.*, *A Gas-Filled UV-Photon Detector with CSI Photocathode for the Detection of Xe Light*, Nucl. Instr. and Meth. **A289**, 322 (1990).

[73] M. Atac, private communication.

[74] M. Atac, in *Vertex Detectors*, ed. by Francesco Villa, Plenum Publishing Corp. (1988), p. 151.

[75] V. Dangendorf *et al.*, presented at the SPIE 1990 Symposium on Instrumentation in Astronomy (Tucson, Arizona, 12-17 Feb. 1990).

[76] R.A. Holroyd *et al.*, *Measurement of the Absorption Length and Absolute Quantum Efficiency of TMAE and TEA from Threshold to 120 nm*, Nucl. Instr. and Meth. **A261**, 440 (1987).

[77] A. Mendes, *Monte Carlo Computer Simulation of the RICH Detector for the Bottom Collider Detector*, BCD Internal Note RP-247 (Aug. 7, 1990).

[78] K. Kodam *et al.*, *Hybrid Emulsion Spectrometer for the Detection of Hadronically Produced Heavy Flavor States*, Nucl. Instr. and Meth. **A289**, 146 (1990).

[79] M.S. Alam, *Time-of-Flight Research and Development*, BCD Internal Note RP-248 (Oct. 1990).

[80] R. Stroynowski, *Light Propagation and Timing with Scintillating Fibers*, Caltech preprint CALT-68-1668 (Aug. 1990).

[81] E. Barsotti *et al.*, *Digital Triggers & Data Acquisition Using New Microplex & Data Compaction IC's*, Proceedings of the Workshop on High Sensitivity Beauty Physics at Fermilab (Nov. 11-14, 1987) J. Slaughter, N. Lockyer, M. Schmidt, editors, p. 369.

[82] E. Barsotti *et al.*, *A Proposed Scalable Parallel Open Architecture Data Acquisition System for Low to High Rate Experiments, Test Beams & All SSC Detectors*, IEEE Trans. Nuc. Sci. **NS-37**, 1216 (1990).

[83] J. Rattner, in Proceedings of the Workshop on B Physics at the SSC (DeSoto, June 1989).

[84] M. Bowden *et al.*, *A High-Throughput Data Acquisition Architecture Based on Serial Interconnects*, IEEE Trans. Nuc. Sci. **NS-36**, 760 (1989).

[85] William J. Dally, *A VLSI Architecture for Concurrent Data Structures*, (Kluwer, Hingham, MA, 1987).

[86] L.D. Gladney *et al.*, *Initial Experience with the Intel i860 Microprocessor*, U. Penn preprint UPR-0184E (March, 1990).

FERMILAB-Proposal-0827

P-827/Add.1

Addendum to the Proposal for a B-Physics Experiment at TEV I: The μBCD

(January 7, 1991)

H. Castro, B. Gomez, F. Rivera, J.-C. Sanabria, *Universidad de los Andes*
J.F. Arens, G. Jernigan, *U.C. Berkeley, Space Sciences Lab*
P. Yager, *U.C. Davis*
J.N. Butler, L.A. Garren, S. Kwan, P. Lebrun, J. Morfin, T. Nash, L. Stutte, *Fermilab*
P. Avery, J. Yelton, *U. Florida*
M. Adams, D. McLeod, C. Halliwell, *U. Illinois, Chicago*
R. Burnstein, H. Cease, H. Rubin, *Illinois Institute of Technology*
E.R. McCliment, Y. Onel, *U. Iowa*
D. London, *U. Montreal*
M.S. Alam, A. Deogirikar, W. Gibson, *S.U.N.Y. Albany*
C.L. Britton, K. Castleberry, C. Nowlin, C. Sohns, *Oak Ridge National Lab*
P. Gutierrez, G.R. Kalbfleisch, D.H. Kaplan, P. Skubic, J. Snow, *U. Oklahoma*
L.D. Gladney, N.S. Lockyer,[1] R. Van Berg, *U. Pennsylvania*
D.J. Judd, D.E. Wagoner, K. Paick, L. Turnbull, *Prairie View A&M U.*
J.G. Heinrich, C. Lu, K.T. McDonald, *Princeton U.*
A.M. Lopez, J.C. Palathingal, A. Mendez, J. Millan, R. Palomera-Garcia, *Universidad de Puerto Rico*
B. Hoeneisen, C. Marin, C. Jimenez, *Universidad San Francisco de Quito*
M. Sheaff, *U. Wisconsin*
A.J. Slaughter, E. Wolin, *Yale University*

[1] Spokesperson

Executive Summary

In this Addendum to the μBCD Proposal[1] we elaborate on several of the themes introduced there. In Section 2 we estimate that modifications to CDF and D0 short of implementing the μBCD have very marginal prospects for observing CP violation. Optimum results would, of course, be obtained in an experiment dedicated to B physics, the full BCD. The μBCD offers a physics path that could lead to the full BCD, or a B-physics experiment within the context of the existing collider program.

The critical technology in the μBCD is the silicon vertex detector. In Sec. 3 we review the need for a 3-dimensional detector – one that measures tracks in two projections. Section 4 proposes extensions to the ongoing BCD R&D program to explore techniques of construction of the 3-D vertex detector. For this we seek a budget of \$126k, and the additional half-time support of an engineering physicist. Section 5 reviews the need for Kaon identification in a B-physics experiment, and notes that the decisive justification is the advantage of a Kaon tag over lepton tags. We close with several comments on the physics of CP violation in Sec. 6.

Contents

List of Tables

List of Figures

1 Introduction

The Fermilab Collider B-physics program should evolve towards an experiment that can study a wide range of phenomena, including CP violation, in the late 1990's. Whether this experiment arises from CDF or D0 or is a new initiative there is a need to develop several technologies that are not emphasized in the present collider program, as they imply some compromise to the capability of top-quark searches. The three technologies are: 1) a 3-D vertex detector, 2) Kaon identification, and 3) a high-rate data-acquisition system. It will require considerable time and effort to develop these technologies, so it is important that work begin now. The μ-BCD proposal provides a near-term B-physics focus for the R&D program, which could proceed in parallel with the ongoing top-quark searches.

The ongoing R&D program (T-784) of the BCD group should include a new level of engineering studies in 1991, as discussed in Sec. 4. For this we seek a budget of \$126k, and the additional half-time support of an engineering physicist.

An immediate issue in defining the scope of B physics at Fermilab in the 1990's is whether CDF or D0 upgrades can reach CP violation in $J/\psi K_S^0$. This mode is a natural starting place for experiments since the triggering is easy. We estimate in Sec. 2 that measurement of CP violation is not possible in upgraded CDF or D0 experiments unless the asymmetry is very large and the upgrades are expanded to include Kaon identification and lepton coverage down to low P_t. Even then, the prospects for a significant measurement are very marginal.

Fermilab should support a program of B physics with a broader scope than only $B \to J/\psi X$ to include B_s mixing and study of CP violation in several modes. The CP-violating asymmetries are not guaranteed to be large in any one class but must be large in at least two of four classes if the Standard Model is correct. The phenomenon of B_s mixing is more accessible than CP violation and serves to test the techniques that must be developed for the latter. A capability for B_s mixing requires a significant investment in triggering and data acquisition.

The μ-BCD is a better starting point for a full-range B-physics program than the proposed CDF and D0 upgrades because of its emphasis on all of the relevant technical issues, and because of its freedom from the operational constraints of the existing top-quark-search experiments.

2 Estimates of Sensitivity of Solenoid and Dipole Detectors to CP Violation in $B \to J/\psi K_S^0$

An upper limit estimate of the future capability of CDF can be made by extrapolation from the 10 or less $J/\psi K_S$ decays being studied in CDF (Internal Note only) from an exposure of 3 pb^{-1}. With no upgrades we would expect 3,300 reconstructed decays in a run of 1000 pb^{-1}. Improvements in muon coverage, and reduction in the minimum P_t cut could triple this to some 10,000 reconstructed decays.

But these must be tagged as to the particle/antiparticle character of the B at production. This can be done via the sign of the lepton in the decay of the second B to $l^{\pm}X$. The total semi-muonic branch is 10%, but acceptance cuts will reduce this by $\sim 1/2$, a P_t cut at 2 GeV/c will cost a factor of 1/4, and the requirement that the muon be consistent with a

secondary vertex will reduce the tagging efficiency by another factor of $\sim 1/3$ to an overall value of about 0.5% in CDF. Hence there would be only about 50 tagged, reconstructed decays via muons that are useful for the CP-violation analysis.

With a sample of N tagged, reconstructed $B \to J/\psi K_S$ decays, the smallest CP-violating asymmetry that can be resolved to three standard deviations is about $(3{\cdot}2{\cdot}2)/\sqrt{N} = 12/\sqrt{N}$, where the factors of 2 arise from the dilutions due to mixing of both the fully reconstructed B, and of the tagging B. Thus 50 events do not allow a significant measurement of CP violation.

We have estimated the potential sensitivity of the proposed CDF upgrade, D0 upgrade, an optimal solenoidal detector for B physics (BSD), and of an optimal dipole detector (BCD) using various combinations of techniques as given in Table 1. The projections for CDF include the effect of adding Kaon identification, which has not been proposed yet.

Table 1: The numbers of tagged, reconstructed $B \to J/\psi K_S$ decays in a run of 1000 pb^{-1} at CDF, at an upgraded D0, at a Bottom Solenoid Detector (BSD), and a Bottom Collider (dipole) Detector (BCD) for J/ψ decays to $\mu\mu$ and ee and for tagging of the second B via $\mu^{\pm}$, $e^{\pm}$, and $K^{\pm}$. Also listed is the minimum value of the CP-violating asymmetry A that could be resolved to three standard deviations. The numbers in parentheses might be obtained in CDF with the addition of Kaon identification, which is not part of the present CDF-upgrade plan.

Technique	CDF		D0		BSD		BCD	
	Events	$A_{\min}$	Events	$A_{\min}$	Events	$A_{\min}$	Events	$A_{\min}$
μ only	50	1.00	140	1.00	140	1.00	200	0.85
e only	50	1.00	50	1.00	500	0.52	500	0.52
$\mu + e$	200	0.85	400	0.60	1200	0.35	1250	0.34
$\mu + K$	(250)	(0.76)	—	—	1400	0.32	2250	0.25
$e + K$	(250)	(0.76)	—	—	3750	0.20	4650	0.18
$\mu + e + K$	(1000)	(0.38)	—	—	5600	0.16	8400	0.13

A number of comments to Table 1 are in order:

1. We assume that the detectors would be equipped with a silicon vertex detector with both 'disks' and 'barrels' permitting 3-dimensional reconstruction of secondary vertices from B's with low transverse momentum.

2. The muon and electron coverages in CDF are assumed to be only modest improvements over that presently planned. For equal coverage of muons and electrons the tagged, reconstructed event sample is four times as large as that for use of muons only.

3. D0 must, of course, be upgraded with a (solenoid) magnet to pursue B physics. While

D0 could evolve into the BSD, the BSD considered here has little in common with the existing D0 detector except the muon system.

4. The Bottom Solenoid Detector (BSD) represents a maximal upgrade of CDF or D0 for B physics. Although its capabilities approach those of the dipole solution (BCD) it will be more difficult technically to achieve them in the solenoid geometry.

5. The BCD is based on a transverse dipole magnet such as the Chicago Cyclotron Magnet. It has full solid angle coverage for tracking, Kaon and electron identification, and forward muon coverage.

6. The muon coverage for D0, the BSD, and the BCD is primarily in the forward regions, with requirements that $P > 3$ GeV/c (to penetrate the hadron absorber) and $P_t > 1$ GeV/c. It is assumed that CDF has only central muon coverage since the P_t trigger in the forward muon system has a threshold too high (5 GeV/c) to affect the CP limits. We allow muons with $P > 2$ GeV/c in the central region of CDF. The net advantage of the new detectors over CDF for muons is only a factor of a few. This advantage is available in a solenoid geometry only if the proposed silicon vertex detector actually functions as the forward tracker as well, at considerably greater cost than a silicon vertex detector for the BCD. The silicon tracker is being proposed by D0.

7. The electron coverage of the BSD and the BCD is assumed to include all $P_t > 1$ GeV/c, for both forward and central electrons. While such coverage would be very advantageous, it will be quite difficult to obtain this in practice. It could only be obtained in CDF or D0 with a major upgrade to their electron-identification systems.

8. The use of Kaons is for tagging the second B via the sign of the Kaon from the $b \to c \to s$ cascade decay. The Kaon tag is about five times as useful as the lepton tags. We presume the needed compact RICH counter could be built for all detectors.

We draw some overall conclusions that are supported by additional arguments in Sections 3 and 5 below:

- A 3-dimensional vertex detector, large-solid-angle low-P_t lepton coverage, and Kaon identification are critical to a CP-violation capability at the Tevatron.

- No Tevatron experiment has a reasonable chance at measuring CP violation without the advantage of a Kaon tag, which requires Kaon identification. This is the decisive justification for hadron identification. The Kaon tag will be based on partial reconstruction of the second B in the event, for which no mass constraints will be available to compensate for an absence of hadron identification.

- The higher event rates at a Bottom Solenoid Detector (BSD) or a Bottom Collider Detector (BCD) with a dipole magnet arise because of increased coverage at forward angles (to which a solenoid field is not well matched) and because of electron identification down to very low transverse momentum. Useful forward muon coverage in a solenoidal detector can only be obtained at the expense of building a silicon tracker rather than a vertex detector. Also, the electron-identification system of the BSD would be a major upgrade beyond those already proposed by either CDF or D0.

3 The Need for a 3-D Vertex Detector

Although fixed-target experiments all use vertex detectors that provide three-dimensional (3-D) measurements of track coordinates, existing vertex detectors for collider experiments are typically two dimensional (2-D). Certainly there is extra complexity in constructing a 3-D vertex detector to provide 4π solid-angle coverage at a collider. Here we review why a 3-D vertex detector is essential for a collider B-physics experiment.

We desire the complete reconstruction of B decays to all-charged final states with high efficiency. To do this in a high-multiplicity environment, the B-decay tracks must be isolated from the primary interaction vertex by the observation of the secondary vertex of the B. The average path length perpendicular to the beam before a B decays is $\approx c\tau = 360$ μm, noting that $\langle P_t \rangle \approx M_B$. Silicon vertex detectors typically have position resolution of 10 μm, which leads to (transverse) vertex resolution of ≈ 20 μm. While this seems small compared to the typical path length of 360 μm that must be resolved, such a silicon vertex detector does not have excess capability, as discussed below.

In addition, we desire to study the mixing of the neutral B mesons, both for its own interest and as a necessity for the analysis of CP-violating decay asymmetries. This requires the determination of the proper decay time to a small fraction of the B lifetime. Again the (transverse) spatial resolution on the secondary decay vertex must be a small fraction of $c\tau = 360$ μm. Precision measurements, particularly important for B_s mixing, are clearly best made with a 3-D vertex detector.

In an experiment that does not aspire to study B_s mixing, could one deliver a viable signal of secondary B-decay vertices with a 2-D vertex detector? Note that two lines in 3-space are in general skew; they have a nonzero distance of closest approach. But in any 2-D projection those two lines appear to cross at some point. There is a qualitative loss of ability to distinguish three-dimensional secondary vertices from random track pairings by restricting measurements to two dimensions.

It is 'intuitively' plausible that if a 3-D vertex detector has a figure of merit F_{3D} for finding true secondary vertices, then a 2-D detector would have a figure of merit $F_{2D} \approx \sqrt{F_{3D}}$.

We illustrate this in a Monte Carlo simulation of events containing $B \to \pi^+\pi^-$ decays.[2] In each event a search is first made for two-track (secondary) vertices consistent with the B mass. Then the remaining tracks are searched for the primary vertex. A measure of the significance of a secondary vertex is the ratio S/σ_S, where S is the distance between the primary and secondary vertices. A two-track secondary vertex will be considered physical only when $S/\sigma_S \gtrsim 10$.

We define the *merit factor* F as the number of detected $B \to \pi^+\pi^-$ secondary vertices divided by the number of false two-track secondary vertices. The simulated results are shown in Fig. 1. For a cut of $S/\sigma_S = 10$ we found that $F_{3D} \approx 24$, while the three different figures of merit for 2-D detectors were $F_{sz} \approx F_{ys} \approx 7$, and $F_{sy} \approx 3$. For a 2-D detector, the stripes of the silicon wafers are along the axis perpendicular to the measurement plane. Thus, the CDF vertex detector with its stripes along the z axis corresponds to F_{sy}.

While our simulation demonstrates the superiority of a 3-D vertex detector it does not yet prove that even this is adequate for a 'difficult' mode like $B \to \pi^+\pi^-$.

Our Monte Carlo simulation is consistent with the experience of the E-687 group. When reconstructing the three-body charm decay $D \to K\pi\pi$, they find a figure of merit of 300 for

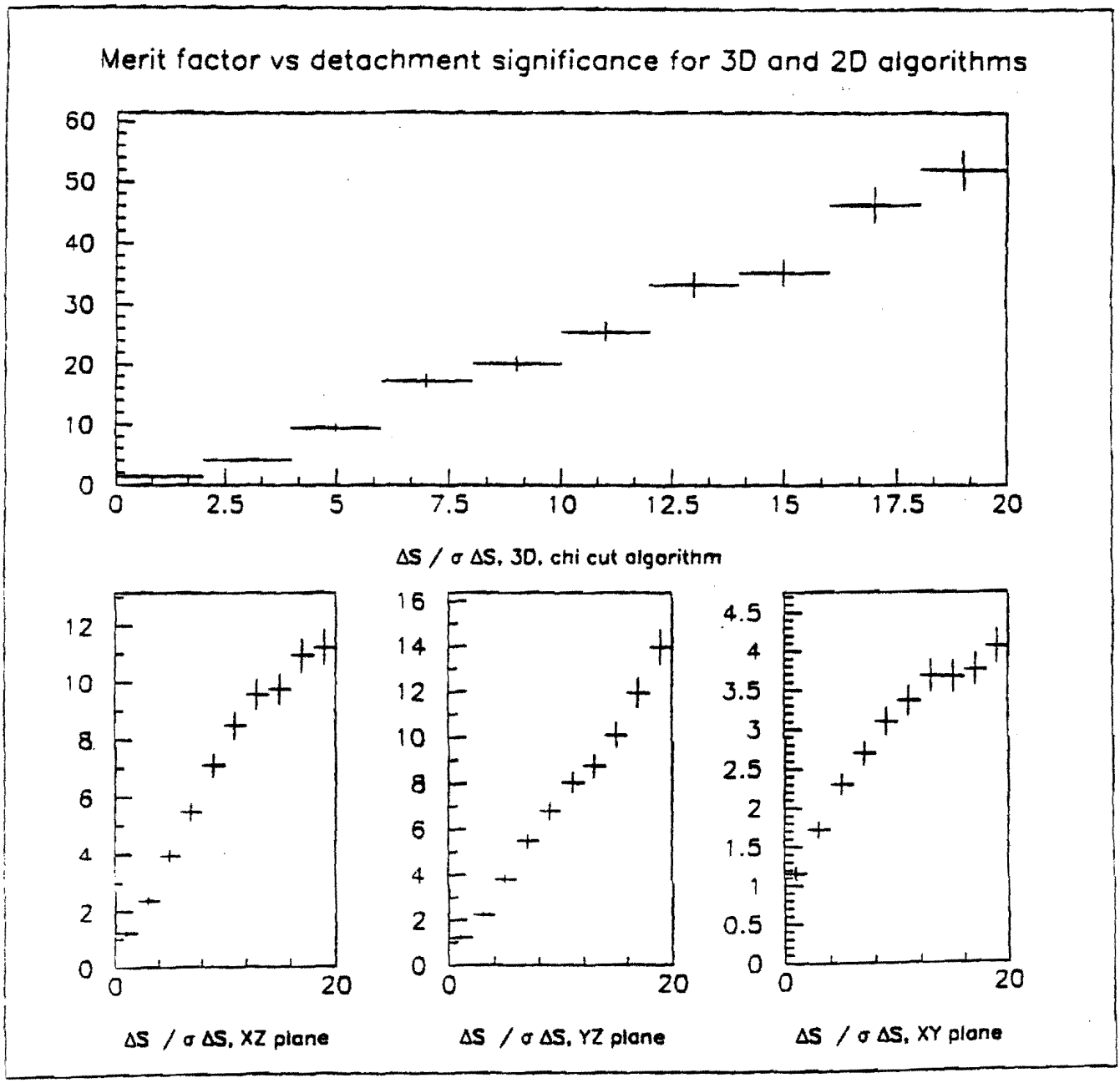

Figure 1: Figures of merit for 3-D (top) and 2-D (bottom) vertex detectors. The figure of merit is the number of correctly identified $B \to \pi^+\pi^-$ vertices divided by the number of false two-track secondary vertices in simulated events each containing a $B \to \pi\pi$ decay. S is the distance between the primary and secondary vertices.

a cut of $S/\sigma_S = 3.5$ using their 3-D vertex detector. The E-687 group has estimated that the figure of merit would be only ≈ 30 if a 2-D vertex detector had been used.

In an experiment that emphasizes study of $B \rightarrow J/\psi X$, the vertex detector would be less critical in identifying such decays as in identifying tracks belonging to the second, tagging B in the event. In general the decay products of the latter will include neutrals and the reconstruction will be partial. We must reliably isolate the charged decay products of the second B from the primary vertex to tag it as a particle or antiparticle. For this a simulated figure of merit of only a few, as for measurement in the x-y plane, is clearly untenable.

4 Vertex Detector R&D

A 3-D vertex detector with large solid-angle coverage has been argued in the previous section to be essential for an ambitious B-physics program at the Tevatron. The critical design features of such a detector are the mechanical alignment, which must be stable to a few microns over a meter, and the cooling, removing about two kilowatts of power from inside the detector.

The BCD is the only group undertaking R&D in these areas at Fermilab. Over the last two years we have constructed and tested a full-scale mechanical/thermal model of the silicon-vertex-detector support structure.[3, 4, 5, 6] In addition, studies were made of the properties of glues, of tensile strengths of pyrex joints, and of cable prototypes. Work on the development of a new VLSI silicon-detector readout chip, and on evaluations of silicon detectors in test beams has been described elsewhere.[7, 8, 9] Here we discuss progress since the last PAC meeting and present new requests in light of this progress.

An opportunity has arisen that will allow us to expand and improve our mechanical R&D program substantially. We are very fortunate to have begun the process of transferring a surplus ANORAD Coordinate Measurement Machine (CMM) from MIT to Fermilab. Though not yet in hand, we are optimistic this machine will be available for use by the BCD within the next two months. The CMM is being purchased by the Fermilab Physics Department for only a few thousand dollars, compared to its original price of about $100k. The machine will be located in Lab 7, and the Fermilab Physics Department is making a strong effort to supply the technician to operate it. We have outlined in Ref. [6] how such a machine could be modified for precision assembly of a 3-D silicon vertex detector.

The CMM will play a central role in our next generation of vertex detector R&D. The mechanical studies fall into four major categories:

1. The study of single silicon-detector wafers can be divided into four subcategories.

   (a) First the study of adhesives, though well underway, is not yet complete. The glues used to adhere the readout chips to the wafers must be shown to be insensitive to both neutron and gamma radiation.

   (b) Second, it is not known whether the glues will react chemically with the surface of either single- or double-sided detectors or AC-coupled detectors, the latter having more extensive surface dopings. We have proposed tests that monitor the pulse-height spectrum from a radioactive source before and after the glues are presented to the detector surfaces.

(c) The third area of concern is the large amount of local heating from the BVX readout-amplifier chips[7] that are glued directly to the silicon-detector wafer. A measure of the noise performance of the BVX *in situ* is very important.

(d) Finally, the **readout-cable design** will be tested by attaching prototype cables to the wafers and studying the effect of heat flow on the mechanical rigidity. Cable termination on the silicon wafer is yet to be developed. Funds needed for substrate and termination-plate samples and contract bonding total $8k.

2. The study of **multi-wafer assemblies**, called modules, requires an assembly procedure with associated fixtures. This work would not be done with the CMM. The purpose of assembling a module is to study the breakage properties of the silicon during assembly and in routine handling of a module.

   (a) The **assembly fixtures** have been designed but not yet built. The fixtures need to be tested and new ones made if the first pass indicates the results are not adequate. Funds of $15k are required for this.

   (b) We have on hand most of the raw materials needed to construct two modules of custom-cut 'junk' silicon using ultraviolet-cured glue and small glass prisms to provide mechanical bridges between wafers. The procedures are detailed in Ref. [6], and we could build such a module in two months. The quoted cost by industry of cutting the glass prisms isbetween $10k and $15k dollars. We have decided to make prototype prisms ourselves and at a cost of $6k.

   (c) After the module is constructed, we would perform stress tests on the wafers and joints, tests of creep *vs.* temperature and radiation dosage. It is also important to determine with what accuracy we can measure the placement of the individual wafers. An **inspection pedestal** has been designed for this purpose but not yet built. Funds needed for the inspection pedestal are $3k.

   (d) We hope to be able to disassemble the module with a solvent. This would be very useful in an operating system since it would facilitate repairs to the detector. We are exploring the use of various adhesives that can later be dissolved, but have yet to test the full procedure.

   (e) Finally, a major issue is the cable routing from inner layers to outer layers. Cables are sources of electrical pickup, multiple coulomb scattering, and impedance to cooling-air flow. The importance of a careful cable-plant design cannot be overemphasized. In our present design we have openings at various locations in the module. We have tested cabling methods using paper cables on a plastic model, but no real cable test on a silicon module has been performed.

3. The assembly studied in item 2 will be by hand, and so has limited accuracy and would not be suitable for a large vertex detector. The ANORAD Coordinate Measurement Machine allows us to address assembly techniques at the accuracy needed for the final vertex detector. We must first upgrade the CMM with features relevant to assembling precision silicon structures: A video camera (+ monitor and video printer), a vacuum-based robotic attachment for prism/wafer placement, and a PC with control software.

Funds of $64k are needed for this. We estimate that an initial 3-D silicon assembly could be completed within six months. People to perform this work have already been identified.

4. During the last two years we performed tests on a 3-meter model of the silicon-vertex-detector support tube ('gutter').[3, 4, 5] The gutter doubles as the mechanical support for a silicon detector that is long (*i.e.*, detects particles in the forward rapidity range as well as central) and is the conduit to which cooling is applied. This mechanical model has already provided many results and continuing this work is very important. An upgrade of the full-scale test station is necessary for more precise results from thermal and vibrational measurements. A new location for the tests that includes an environmentally controlled room has been found at the lab. An engineering physicist is needed who can spend 50% time on this project. In addition, we estimate that $30k is needed to purchase position sensors that provide accuracies down to a micron, a new blower for improved cooling, and a better liquid-cooling assembly.

In summary, the mechanical tests are as critical to the success of a next-generation vertex detector as the readout chips are to this generation of detectors. We emphasize that progress in all four categories are needed in the next year before a full system design can be attempted. The acquisition of the CMM and its full exploitation is critical for the success of this program. We seek funds of $126k and an engineering physicist 50% time are needed to make major progress in the next 9 months, as summarized in Table 2.

Table 2: Funding request for continued R&D on a 3-D silicon vertex detector. We also seek a half-time engineering physicist to work on this project.

1. Readout-cable prototypes	$8k
2. Multi-wafer assembly fixtures (non-robotic)	$15k
3. Glass prisms	$6k
4. Inspection pedestal	$3k
5. Multi-wafer assembly fixtures (robotic)	$64k
6. Upgrade of full-scale test station	$30k
7. **Total**	**$126k**

5 The Need for Kaon Identification

There are two important reasons for Kaon identification in a B-physics experiment:

1. The most effective tag as to the particle/antiparticle character of a neutral B is via the sign of the Kaon from a $b \to c \to s$ cascade decay of the second B in the event. This is needed for studies of CP violation as well as for B-$\bar{B}$ mixing.

2. The majority of all-charged decays of B and D mesons include one or more Kaons.

Of these, the first reason is the critical one. Without Kaon identification there is very little prospect of accumulating a large enough sample of tagged B decays at the Tevatron to study CP violation.

When reconstructing an all-charged decay of a B or D meson, mass constraints may provide sufficient ability to identify Kaons in software without a hardware device for that purpose.

These issues are discussed in greater detail in the following two subsections.

5.1 Efficiency of Lepton and Kaon Tags

[This subsection appeared as Sec. 7.5 of Ref. [1], but we repeat it here to give it further emphasis.]

In this section we argue that a Kaon tag (which requires Kaon identification) would be about five times as effective as combined electron and muon tags.

We propose to determine the particle/antiparticle character of a fully reconstructed B meson via a tag on the second B in the event. The tag would be based on the sign of the lepton in a partial reconstruction of the decays $B \to l^{\pm}X$, or on the sign of the Kaon in $B \to K^{\pm}Y$. The lepton tag would be available for at most 20% of the events (due to the semileptonic branching fraction). Kaons occur in almost 100% of all B decays via the cascade $b \to c \to s$. Charged Kaons occur is about 65% of all B decays, taking into account Kaons arising from the decay of virtual W bosons associated with the quark-flavor transitions.

For all tags there is some probability of mistagging from a wrong-sign lepton or Kaon due to secondary and tertiary decays. If the probability is p that a wrong-sign tag is made, then the statistical power of a sample of N tagged events is reduced to that of $N(1-2p)$ perfectly tagged events. We will find below that mistagging is more probable for the lepton than the Kaon tag, if one integrates over the entire transverse-momentum spectrum of the leptons and Kaons.

Since we only have to worry about the tagging quality when we have a fully reconstructed B, we can have confidence that any other secondary vertex in the event is that of the second B, even if the latter is only partially reconstructed. Hence we only examine the decays of the second B to estimate the mistagging probability p. For this we have generated a sample of 10^5 B-$\bar{B}$ pairs at TEV I using ISAJET, and let them decay according to a representative sample of hadronic and semileptonic modes following Bjorken.[10]

The P_t spectra of right-sign leptons (from the primary decay $b \to W^- \to l^-\nu$) and of wrong-sign leptons (from the secondary decay $b \to c \to W^+ \to l^+\bar{\nu}$, *etc.*) are shown in Fig. 2. There are actually about 1.5 times as many wrong-sign leptons as right sign, although the

wrong-sign leptons have markedly lower P_t . The P_t spectrum of right-sign Kaons (from $b \rightarrow c \rightarrow s$ with the s-quark appearing in a Kaon) is shown in Fig. 3, and is essentially identical to that of wrong-sign Kaons (from $b \rightarrow W^- \rightarrow \bar{c} \rightarrow \bar{s}$, or $b \rightarrow c \rightarrow W^+ \rightarrow \bar{s}$, *etc.*). However, right-sign Kaons outnumber wrong-sign Kaons by 6 to 1 (according to the model branching fractions of Ref. [10]).

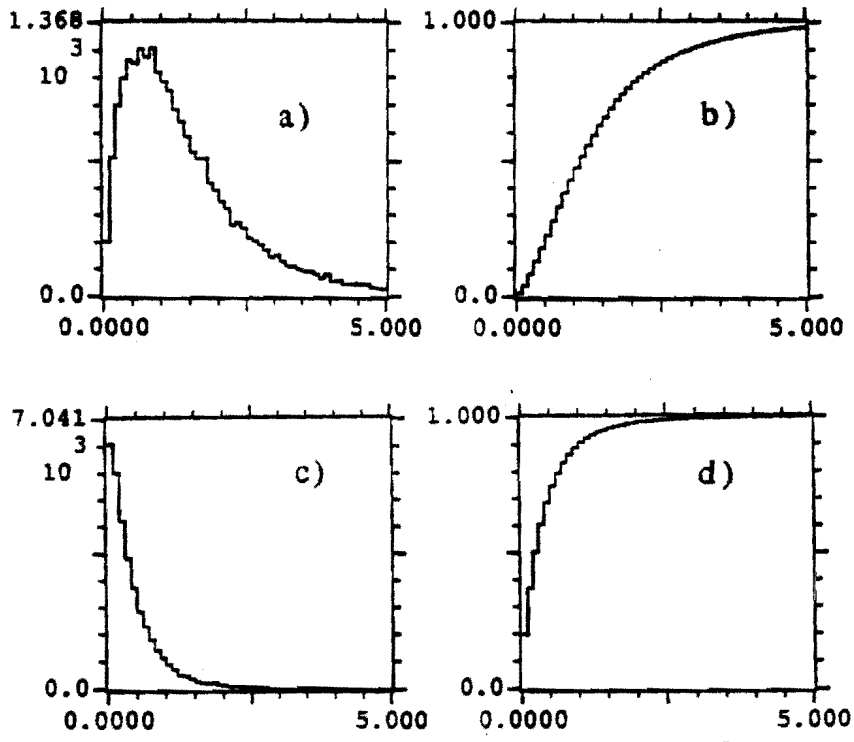

Figure 2: a) The P_t spectrum for single leptons from $B \rightarrow l^{\pm}X$. b) The integral spectrum of a). c) The P_t spectrum for leptons from $B \rightarrow DX$ with $D \rightarrow l^{\pm}Y$. d) The integral spectrum of c).

In using the leptons (or Kaons) to determine the particle/antiparticle character of the second B we simply look at the sign of the highest-P_t lepton (or Kaon). Only in a small fraction of the decays are there two leptons (or two Kaons) and we have made no attempt to devise a more sophisticated algorithm for this small subset.

Figure 4 shows the fraction of all leptons (or Kaons) at a given P_t that have the wrong sign. While at no P_t are wrong-sign Kaons a problem, for $P_t < 500$ MeV/c the wrong-sign leptons dominate the right-sign. That is, the lepton tag is worthless at $P_t = 500$ MeV/c. For P_t less than this we can change our definition of 'right' and 'wrong' and obtain some useful tags.

The effectiveness of the tags is presented another way in Fig. 5. The quantity $N\,|1-2p|$, the effective number of useful events, is plotted as a function of P_t in the left-hand plots.

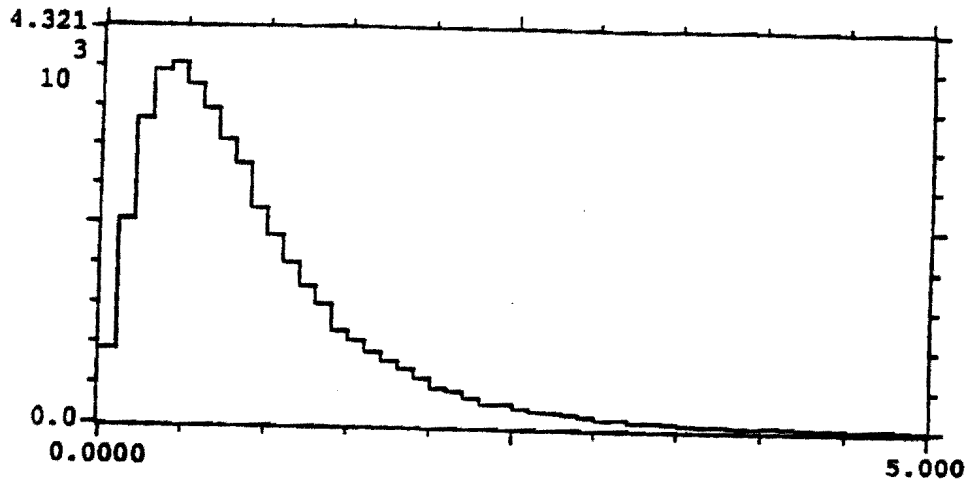

Figure 3: The transverse-momentum spectrum of right-sign Kaons from B-meson decay.

The right-hand plots show the integral

$$\int_{P_t}^{\infty} dN\,|1-2p|\,.$$

The integrals have been normalized to the total number of B's, and so represent the efficiency of a tag as a function of the minimum-P_t cut.

The Kaon tag will be about 10 times as useful as a lepton tag, or 5 times as useful as the combination of electron and muon tags.

The efficiency of the lepton tags increases only slightly as the P_t cut is lowered below 1 GeV/c, due to the abundance of low-P_t wrong-sign leptons. A way around this is to use a combined lepton and Kaon tag, requiring both a right-sign lepton and Kaon. Row three of Fig. 5 shows how for very low P_t this tag becomes more efficient than a lepton tag alone, although at high P_t it is only 1/2 as efficient. The combined lepton and Kaon tag is superior from the point of view of immunity to backgrounds we have not considered here.

5.2 Kaon Identification Via Mass Constraints

In this section we show that if the B-decay products have been successfully isolated from the rest of the event (by a vertex detector) then all-charged modes can be reconstructed correctly with good probability without hardware particle identification. However, misidentifications of decays with neutrals, and confusions between the B_d and B_s are shown to be so severe that particle identification is warranted. Of course, there is extensive experience in the community that particle identification is vital when background tracks are present in the sample.

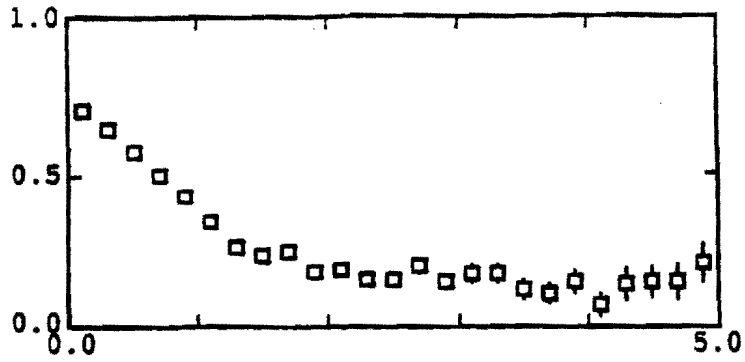

wrong sign e fraction vs PT

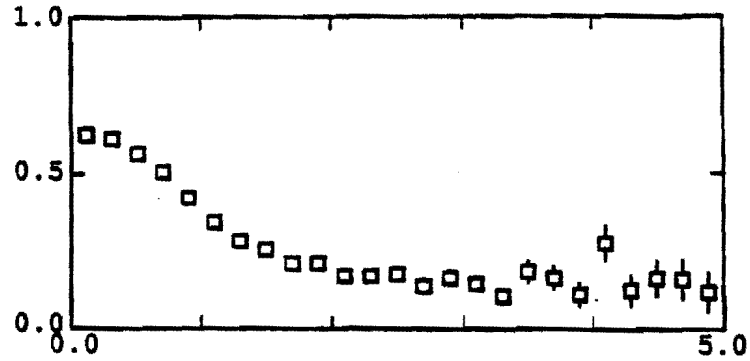

wrong sign mu fraction vs PT

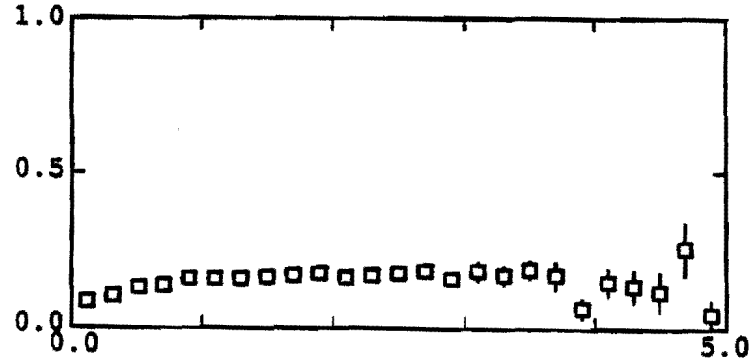

wrong sign K fraction vs PT

Figure 4: The fraction of leptons (or Kaons) that have the wrong sign as a function of P_t .

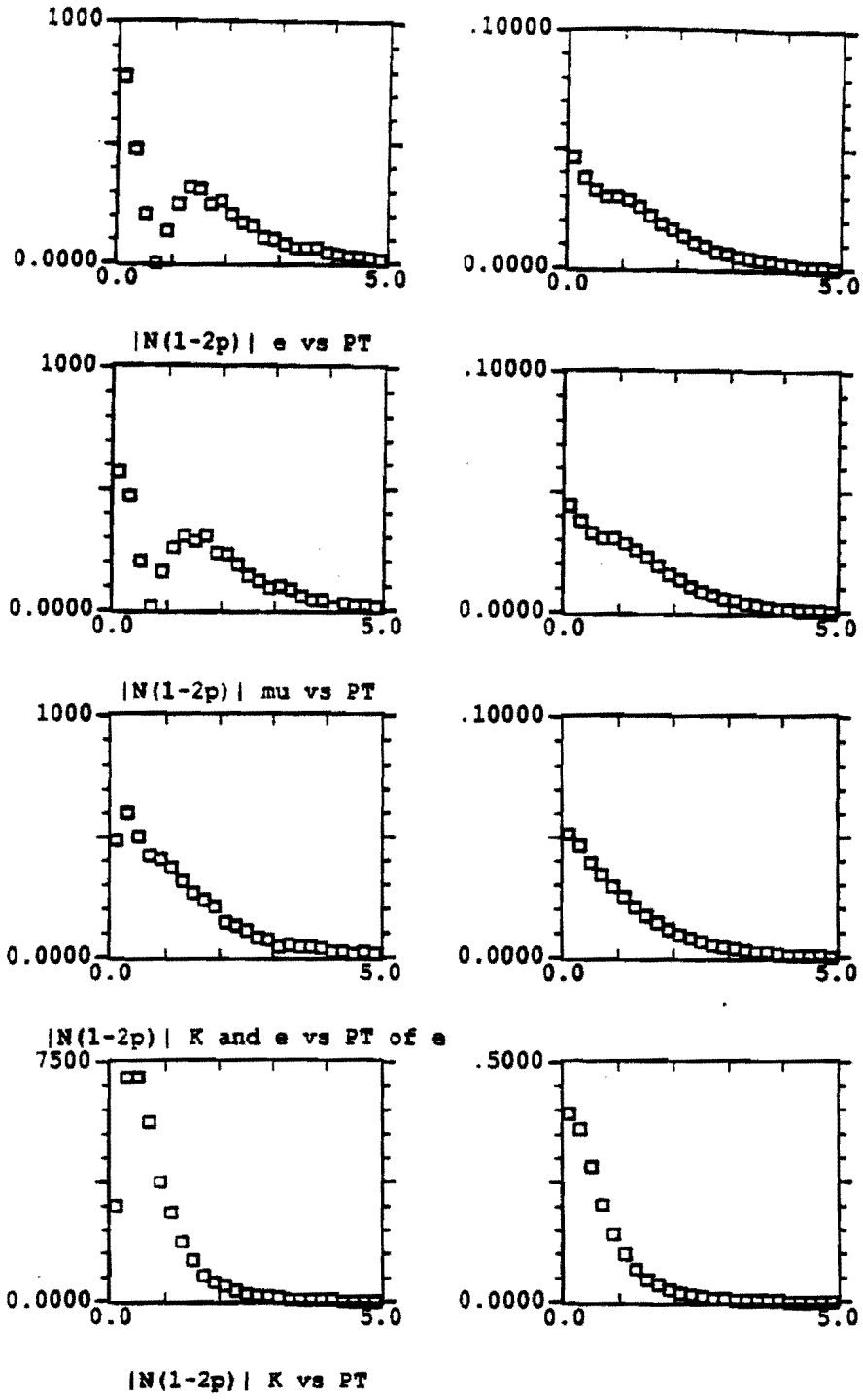

Figure 5: Differential and Integral tagging efficiencies of four types of tags as a function of transverse momentum. Left hand plots: the number $N|1-2p|$ of useful tagged events; right-hand plots: the total efficiency of the tag as a function of the minimum-transverse-momentum requirement. The four tags are, from top to bottom, electron, muon, combined electron and Kaon, and Kaon.

For our study we used the sample of 10^5 B-$\bar{B}$ pairs generated by ISAJET as described in the previous subsection. We suppose that the accuracy of the momentum measurement of the charged tracks is

$$\frac{\sigma_P}{P} = \sqrt{(0.004)^2 + (0.0015P_t)^2}.$$

This is a good approximation to the resolution currently achieved in CDF, and reproduces their mass resolution of 17 MeV/c^2 for $J/\psi \rightarrow \mu^+\mu^-$ decays with $P_t > 2$ GeV/c for the muons, and $P_t > 4$ Gev/c for the J/ψ.

We begin with the charged meson B_u. Among the sample of 10^5 B decays were 133 examples of $B_u \rightarrow$ all-charged tracks. In the absence of hadron identification we supposed that each track could be either a pion or a Kaon. For an n-body decay there are then 2^n different hypotheses as to the identity of the tracks. For each of these we calculated the invariant mass, using track momenta smeared according to the above prescription.

- The hypothesis with reconstructed mass closest to the known mass of the B_u was taken as the 'correct' one.

In 76% of the cases this analysis actually provided the proper particle identification. Some details are given in Table 3. At this stage we ignore the possibility that the decay includes separated vertices due to cascade D- or K-meson decays.

Table 3: The numbers of $B_u \rightarrow$ all-charged decays for which the correct particle identification was obtained by examining which hypothesis yielded the best invariant mass. Also shown are the numbers of correct identifications when the 'plausibility' cut, described in the text, is applied as well.

n_{track}	Correct ID Via		Total
	Best Mass	Plausibility Cut	Events
3	3	1	4
5	12	2	21
7	25	11	38
9	33	18	38
11	23	14	27
13	5	4	5
all	101	50	133

The results of Table 3 are very encouraging, but they were obtained with the knowledge that the set of tracks to be studied was the proper one. In practice we will not have this knowledge. For example, most B decays contains neutrals that cannot be associated with the charged tracks by the vertex detector. Most likely we will have to consider the neutrals as missing. The remaining charged tracks that fit to a secondary vertex are then

(incorrectly) presented as candidates for an all-charged decay of the B. With the correct particle identification of these tracks, their combined invariant mass would be less than the B mass by at least M_π and the event could be rejected. However, without particle identification, hypotheses in which pions are called Kaons lead to larger invariant masses and might by accident coincide with the B mass.

In an attempt to reject track sets with missing neutrals we make an additional requirement:

- The hypothesis with invariant mass closest to the B mass is considered valid only if the mass difference is less than two standard deviations.

From the known form of the momentum resolution the error on the invariant mass of a given track set can be estimated for this. With momentum resolution as given above the B-mass resolution is rather good, varying from 17 MeV/c^2 for 3-track decays to only 7 MeV/c^2 for 13-track decays.

However, even using our revised prescription a large number of B_u decays with missing neutrals were claimed to be correctly identified all-charged decays. The numbers of events are summarized in Table 4. In particular we see that events with large numbers of charged tracks are readily misidentified.

Table 4: The numbers of B_u decays with missing neutrals for which an hypothesis as to the identity of the charged tracks led to an all-charged invariant mass within $\pm 2\sigma$ of the B mass. These events would then be incorrectly identified. Also shown are the numbers of decays with missing neutrals that pass the 'plausibility' cut.

n_{track} (charged)	'Correct' ID Via 2-σ Cut	Plausibility Cut	Total Events
3	4	1	2982
5	268	114	5512
7	1448	338	5560
9	2786	161	3497
11	1252	9	1266
13	235	3	237
all	5993	626	19054

On examining the decays with missing neutrals that were mistakenly identified as all-charged decays, we noticed that if an event is misidentified there are often many different ways of doing this all with invariant-mass hypothesis close to the true B mass. On the other hand, in the true all-charged decays typically only the correct particle identification led to a mass close to the B mass. Accordingly we have applied an additional criterion for particle identification:

- When N different hypotheses as to the identity of the charged tracks all lead to invariant masses within $\pm 2\sigma$ of the B mass, we define the 'plausibility' of the identification as $1/N$. Only decays with plausibility $> 90\%$ are considered to be identified.

The use of the 'plausibility' cut significantly reduces the number of events with missing neutrals that are mistakenly identified as all-charged decays, as also summarized in Table 4. The effect of applying the plausibility cut to the true all-charged decays is shown in Table 3, where we see that 38% of the all-charged events survive the plausibility cut. Unfortunately, because there are so many more decays with neutrals than all-charged tracks, the number of misidentified decays that pass our cuts is still larger by an order of magnitude than the number of correctly identified all-charged decays.

Thus far we have not taken advantage of the possibility that some of the B-decay products arise from the tertiary decay of a long-lived D or K meson. With a vertex detector that correctly associates these tracks with a separated vertex, additional constraints will be available. Here we estimate the maximum advantage that might be obtained from tertiary vertices by examining the decays $B_u \to D^0+$ all-charged tracks.

We suppose that the D^0 is correctly identified in a separate study, and all that remains is to identify the charged tracks associated with the B-decay vertex. Again we examine the invariant masses of the various particle-ID hypotheses and apply the plausibility cut, with results as shown in Table 5. The tertiary vertex can indeed be very helpful; in contrast to the results of Table 3, we now correctly identify 94% of the B_u decays. Of course, one must factor in the probability that the tertiary vertex is correctly analyzed.

Table 5: The numbers of $B_u \to D^0+$ all-charged decays for which the correct particle identification was obtained by examining which hypothesis yielded the best invariant mass. Here the D^0 has been assumed to have been correctly identified via its decay products which form a separated tertiary vertex.

n_{track} (charged)	Correct ID Via 2-σ Cut	Plausibility Cut	Total Events
2	25	18	25
4	22	20	23
6	35	35	35
8	11	11	12
10	2	2	3
all	95	86	98

We must also consider those events in which a D^0 is successfully reconstructed at a tertiary vertex, but the tracks from secondary B vertex include neutrals. According to Ref. [10] the situation here is relatively favorable in that a substantial fraction of the decays $B_u \to D^0 X$ have X as all-charged. The results of our simulation are shown in Table 6, where

we infer that the observation of a tertiary D vertex could raise the signal-to-noise to 2 : 3. However, we would still prefer a signal-to-noise much larger than one.

Table 6: The numbers of $B_u \rightarrow D^0 + X$ decays where X includes missing neutrals for which the charged tracks were incorrectly identified as reconstructing to the B mass. The D^0 has been assumed to have been correctly identified via its decay products which form a separated tertiary vertex.

n_{track} (charged)	'Correct' ID Via 2-σ Cut	Plausibility Cut	Total Events
2	24	17	298
4	33	29	261
6	79	64	236
8	50	24	75
10	8	4	9
all	194	138	879

We now turn to the neutral mesons, B_d and B_s. These have masses that differ by only a small amount (the value is not presently known, but was taken as 200 MeV/c^2 in this study). If we have a set of tracks whose total charge is zero associated with a secondary vertex, then we must compare our hypotheses as to the particle ID's with both the B_d and the B_s. We might well have a B_d mistakenly identified as a B_s, or *vice versa*. A measure of the probability of this is given in Tables 7 and 8.

With two mass hypotheses to be considered for each neutral decay, there are typically so many ways of satisfying one or the other hypothesis that our 'plausibility' cut is of little use. The problem of B_d's being misidentified as B_s's is particularly severe as there will be many more all-charged decays of the B_d than of the B_s.

We have attempted to derive an advantage from the existence of tertiary decays in another manner. The B-decay products may include daughter mesons such as D, J/ψ, ϕ, K_S... that decay in turn. This time we do not suppose that the daughters have separated tertiary vertices, but that their decay products are intermixed with those directly from the B decay. However, we examine subsets of the B-decay tracks for those that reconstruct to the mass of one of the possible daughter mesons. This search is more fruitful if we restrict ourselves to hypotheses for the decay products of the daughters that lead to a B mass when combined with the rest of the tracks from the B decay. Tables 9 and 10 list the fraction of all-charged B_d decays that are thus correctly reconstructed in this manner, and the numbers of misidentified decays when there are missing neutrals. With this approach we only achieve a signal-to-noise of 1 : 4.

While our present study does not exhaust the possibilities of analyses of B decays without explicit particle identification, it indicates that the signal quality will not be high. In view

Table 7: The numbers of $B_d \rightarrow$ all-charged decays for which the correct particle identification was obtained by examining which hypothesis yielded the best invariant mass. Also listed are the numbers of decays for which the 'best' particle-ID hypothesis fitted to the B_s mass.

n_{track}	Correct ID as B_d	Wrong ID as B_s	Total Events
4	169	33	222
6	48	44	105
8	35	40	87
10	23	17	43
12	8	6	15
all	283	140	472

Table 8: The numbers of $B_s \rightarrow$ all-charged decays for which the correct particle identification was obtained by examining which hypothesis yielded the best invariant mass. Also listed are the numbers of decays for which the 'best' particle-ID hypothesis fitted to the B_d mass. The 'plausibility' cut has been applied.

n_{track}	Correct ID as B_s	Wrong ID as B_d	Total Events
4	8	2	11
6	19	2	25
8	17	2	23
10	2	2	4
12	4	2	7
all	50	9	70

of this it appears wise to provide for Kaon identification in the hardware.

Table 9: The numbers of $B_d \rightarrow$ all-charged decays for which the correct particle identification was obtained by simultaneous fits for the B mass and the mass of a daughter meson. No use is made of a possible tertiary vertex. The column labelled '2-σ Cut' includes all decays for which the correct particle identification leads to B and daughter masses both within 2σ of the true value, whether or not this identification was the 'best.'

$n_{\text{daughters}}$	Correct ID Via		Total
	2-σ Cut	Plausibility Cut	Events
2	47	32	47
3	153	112	181
4	162	132	189
5	47	32	65
6	28	12	47
7	18	12	41
8	9	4	29
9	12	9	21
10	6	1	17
11	5	4	6
12	2	0	3
13	2	1	2
all	491	351	648

Table 10: The numbers of $B_d \to X$ decays for which X includes missing neutrals and an incorrect particle identification was obtained by a simultaneous fit for both the B mass and the mass of a daughter meson.

n_{track} (charged)	'Correct' ID Via 2-σ Cut	Plausibility Cut	Total Events
2	3	3	2014
3	14	10	1257
4	196	86	9383
5	366	177	2553
6	2034	563	9565
7	1006	272	2421
8	3248	319	5583
9	791	53	1005
10	850	29	976
11	182	4	186
12	113	0	116
13	19	0	21
all	8822	1516	35080

6 Comments on CP-Violation Physics

In this section we make a number of brief comments to supplement the lengthier discussions of the physics of CP violation we have given elsewhere.[1, 11]

6.1 The Four Classes of CP Violation of Neutral B Mesons

CP violation can be very prominent in the B-meson system because the relevant CP-violating phases in the CKM matrix occur in first order. This is in contrast to the K-meson system where CP-violating phases arise in the relevant matrix elements only in higher order.

In the neutral B-meson system there are four classes of CP violation, as readily seen in the Wolfenstein representation of the CKM matrix. For this we need only note the location of the matrix elements that have imaginary parts (to first order):

$$V_{CKM} = \begin{pmatrix} V_{ud} & V_{us} & V_{ub} \\ V_{cd} & V_{cs} & V_{cb} \\ V_{td} & V_{ts} & V_{tb} \end{pmatrix} \approx \begin{pmatrix} \mathrm{Re} & \mathrm{Re} & \mathrm{Im} \\ \mathrm{Re} & \mathrm{Re} & \mathrm{Re} \\ \mathrm{Im} & \mathrm{Re} & \mathrm{Re} \end{pmatrix}.$$

The phase of V_{td} enters in B_d (but not B_s) mixing due to top-quark exchange in the box diagram.

The phase of V_{ub} enters in $b \to u$ (but not $b \to c$) decays.

Hence there are 4 classes of CP violation in decays of neutral B's, as listed in Table 11.

Table 11: The four classes of CP violation in the neutral B-meson system.[12]

Class	Parent	Quark Transition	Example	CP-Violating Phase
1	B_d	$b \to c$	$B_d \to J/\psi K_S$	$\varphi_1 = \varphi(V_{td})$
2	B_d	$b \to u$	$B_d \to \pi^+\pi^-$	$\varphi_2 = \varphi(V_{td}) + \varphi(V_{ub})$
3	B_s	$b \to u$	$B_s \to \rho K_S$	$\varphi_3 = \varphi(V_{ub})$
4	B_s	$b \to c$	$B_s \to J/\psi\phi$	$\varphi_4 = 0$

For decays of neutral B's to CP eigenstates f, the observable effect is the decay asymmetry

$$A(t) = \frac{\Gamma(B \to f) - \Gamma(\bar{B} \to f)}{\Gamma(B \to f) + \Gamma(\bar{B} \to f)} = \sin 2\varphi_i \sin xt,$$

where φ_i is the relevant phase of the CKM matrix element listed above, $x = \Delta M/\Gamma$ is the mixing parameter, and t is the proper time of the decay.

As there are three classes of nonzero asymmetries, we can make three measurements of the two CKM phases, and hence overconstrain the Standard Model.

This insight is also commonly expressed via the unitarity triangle. But it is important to note that the Standard Model predicts a null effect in a fourth class of decays, which are quite accessible at the Tevatron.

6.2 The Einstein-Rosen-Podolsky Effect

If the B^0-$\bar{B}^0$ pair is produced in a C(odd) or C(even) combination, this quantum-mechanical correlation in maintained until both B's decay, even though they may be spatially separated, and they decay at different times. The complexity of such correlations was first noticed by Einstein, Rosen, and Podolsky[13] in a famous paper in which they argued that this indicates that quantum mechanics is an incomplete theory. However, no one seriously doubts that the EPR effect is real.

The application of the EPR effect to the neutral B-meson system was first noted by Carter and Sanda.[14] Suppose that one B meson (B_1) decays to a CP eigenstate f at time t_1, and that the second B meson (B_2) decays at time t_2 to a state $g \neq \bar{g}$ (such as $B \to l^{\pm}\nu X$) that allows us to determine whether it was a B or $\bar{B}$ at time t_2. Then the combined decay asymmetry

$$A(t_1,t_2) = \frac{\Gamma(B_1 \to f)\Gamma(\bar{B}_2 \to \bar{g}) - \Gamma(B_1 \to f)\Gamma(B_2 \to g)}{\Gamma(B_1 \to f)\Gamma(\bar{B}_2 \to \bar{g}) + \Gamma(B_1 \to f)\Gamma(B_2 \to g)} = \sin 2\varphi \sin(x_1 t_1 \mp x_2 t_2),$$

where the minus sign holds for C(odd) states: $|B_1\bar{B}_2\rangle - |\bar{B}_1 B_2\rangle$.

If we don't observe the decay times, the integrated asymmetry is

$$A = \frac{x_1 \mp x_2}{(1+x_1^2)(1+x_2^2)} \sin 2\varphi,$$

which vanishes for C(odd) states in which $B_1 = B_2$ (*i.e.*, $B_d\bar{B}_d$ or $B_s\bar{B}_s$).

For B_d^0-$\bar{B}_d^0$ produced at the $\Upsilon(4S)$ at an e^+e^- collider, we have only C(odd) states, and hence there will be no signal for CP violation unless one can observe the time evolution. This is the well-known justification for the construction of an asymmetric e^+e^- collider, which would be a costly consequence of the EPR effect.

6.3 Dilutions Due to Mixing

We continue the theme of the previous subsection by considering the case of a hadron collider (at c.m. energies far above B-production threshold). Here, B^0-$\bar{B}^0$ pairs are produced as incoherent sums of C(odd) and C(even) states. Then we see from the above that the combined decay asymmetry averages to

$$A(t_1,t_2) = \sin 2\varphi \sin x_1 t_1 \sin x_2 t_2,$$

and the integrated asymmetry averages to

$$A = \frac{x_1}{1+x_1^2}\frac{1}{1+x_2^2} \sin 2\varphi.$$

That is, the effects of the time dependences of the decays of the first and second B's factorize, and the result is the same as if we had not concerned ourselves with the EPR effect at all.

However, this analysis emphasizes another important point: the 'dilutions' due to mixing if one makes time-integrated measurements. This refers to the factors $x_1/(1+x_1^2)$ and

$1/(1+x_2^2)$ that multiply $\sin 2\varphi$ in the asymmetry. They arise because of the uncertainty that a neutral B meson has the same particle/antiparticle character at production and decay.

When $x_1 \lesssim 1$, as for the B_d, there are several lifetimes per period of oscillation, so even a time-resolved study of the decay is little different from a time-integrated study. Hence the measurable asymmetry of B_d decays will always be subject to a factor $\approx x_d/(1+x_d^2) \approx 0.5$, using the current experimental value that $x_d = 0.7 \pm 0.1$

For B_s decays where $x_s \gg 1$ we have shown in Sec. 3.3.2 of Ref. [1] that the appropriate dilution factor (for meson 1) is $2/\pi$, assuming a time-resolved analysis.

In addition, there is a second dilution factor, $1/(1+x_2^2)$, due to mixing of the second, tagging B. The second dilution factor differs from the first because the final state $g \neq \bar{g}$ for the second B meson, while the final state $f = \bar{f}$ for the first meson. The second dilution factor was deduced from a different argument in Sec. 3.2.2 of Ref. [1].

At a hadron collider the second B can be a B_u, a B_d, or a B_s. The B_u does not mix ($x_u = 0$), so has a dilution factor we can call 1, the B_d has a dilution factor $\approx 2/3$, while the B_s has a dilution factor ≈ 0 if $x_s \gg 1$ as expected. Supposing the three flavors of B mesons are produced in the ratios $B_u : B_d : B_s = 0.375 : 0.375 : 0.25$, the overall dilution factor for the second meson would be 0.63. Allowing for the possibility of misidentifying whether the second B is a particle or antiparticle, we take the second dilution factor to be ≈ 0.5. (It is convenient to remember both the first and second dilution factors as 0.5, but the detailed reasoning differs considerably.)

B_s mesons are essentially useless for tagging unless they can be identified and the decay time measured. But the second, tagging B will likely be only partially reconstructed, which will not permit an evasion of the dilution due to mixing.

The second dilution due to mixing could be avoided by restricting the tag to B_u. However, only 35-40% of the second B's will be B_u, so unless these can be definitely identified as such with greater than 60% efficiency there is no advantage over tagging without flavor identification of the second B.

We summarize this section by noting that the smallest value of $\sin 2\varphi$ in a CP-violating asymmetry that can be resolved to three standard deviations with N events is not $3/\sqrt{N}$ but rather

$$\sin 2\varphi_{\min,3\sigma} \approx \frac{3 \cdot 2 \cdot 2}{\sqrt{N}} = \frac{12}{\sqrt{N}}$$

at a hadron collider. The two factors of 2 are the dilutions due to mixing of the first and second B's. At an asymmetric e^+e^- collider the corresponding sensitivity would be $9/\sqrt{N}$.

6.4 The Superweak Model

The superweak model is often used as a vehicle for discussions of alternatives to the Standard Model of CP violation. The comments below are based on conversations with B. Winstein and L. Wolfenstein.[18]

The superweak model is that CP-violating effects are due to a new interaction that manifests itself only in the mixing of a neutral meson and its antiparticle. The effect is small, but different for each type of neutral meson. In the superweak model there are only two classes of CP violation in the neutral B mesons, one for B_d, and another for B_s. This

contrasts with the four classes discussed above in the Standard Model. Thus the observation that either

1. $\sin 2\varphi_1 \neq \sin 2\varphi_2$, or that
2. $\sin 2\varphi_3 \neq \sin 2\varphi_4$

would contradict the superweak model. In the Standard Model it is possible that $\sin 2\varphi_1 = \sin 2\varphi_2$, but it is extremely unlikely that both equalities would hold simultaneously.

A third confrontation between the superweak and Standard Models is possible with B mesons:

3. The Standard Model suggests that there will be small but nonzero CP-violating asymmetries in the decay rates of B^+ and B^- mesons, while the superweak model predicts a null effect.

7 Concluding Remarks

We conclude with a few remarks and a reiteration of the goal of the μBCD.

1. B physics should be pursued as a **program** of study at Fermilab and not simply a subtopic of a high-P_t collider detector.
2. A B-physics experiment that seeks to study CP violation must include the following three technologies: a 3-D large-solid-angle silicon vertex detector, Kaon identification, and a high-rate data-acquisition system.
3. The BCD Collaboration has made substantial progress in all these areas with very limited resources.
4. We encourage the PAC and Fermilab to expand and improve upon the start of BCD towards a collider B-physics experiment at Fermilab by forming an in-house group dedicated to this research.
5. The μBCD concept, an R&D program followed by physics studies, will focus interested parties on B physics in the next 5 years.
6. The experience gained from developing the stated technologies and the observation of B_s mixing is the best way for Fermilab to compete with e^+e^- proposals for a full B-physics program late in this decade.

8 References

[1] BCD Collaboration, *Proposal for a B-Physics Experiment at TEV I: The μBCD*, submitted to Fermilab (Oct. 8, 1990).

[2] P. Lebrun, *A Bottom Collider Vertex Detector Design, Monte-Carlo Simulation and Analysis Package*, FNAL-TM-1682 (Oct. 1, 1990).

[3] H. Mulderink, N. Michels, and H. Jöstlein, *Mechanical and Thermal behavior of a Prototype Support Structure for a Large Silicon Vertex Detector (BCD)*, Fermilab TM-1616 (August 23, 1989).

[4] H. Jöstlein and J. Miller, *Heat Resistance and Air Pressure Drop in a Model of the BCD Silicon Vertex Detector*, BCD Internal Note RP-211 (Jan. 9, 1990).

[5] H. Jöstlein and H. Mulderink, *Continued Studies of the Mechanical and Thermal behavior of a Prototype Support Structure for a Large Silicon Vertex Detector (BCD)*, Fermilab TM-1685 (Oct. 1990).

[6] C. Lindenmeyer, *Proposed Method of Assembly for the BCD Silicon Strip Vertex Detector Modules*, Fermilab TM-1627 (Oct. 16, 1989).

[7] R. Yarema, *BVX Workshop Summary*, BCD-RP-207 (Nov. 28, 1989).

[8] H. Attias *et al.*, *Beam Tests of Silicon Microstrip Detectors with VLSI Readout*, to appear in the Proceedings of the IEEE Detector Conference (Crystal City, Oct. 1990).

[9] P. Skubic *et al.*, *Vertex Detector Technology for the SSC*, to appear in the Proceedings of the SSC Detector Symposium (Ft. Worth, Oct. 1990).

[10] J.D. Bjorken, *Estimates of Decay branching Ratios for Hadrons Containing Charm and Bottom Quarks*, (1986), unpublished.

[11] BCD Collaboration, *Bottom Collider Detector Expression of Interest*, submitted to the SSC (May 25, 1990).

[12] P. Krawczyk, D. London, R.D. Peccei, and H. Steger, *Predictions of the CKM Model for CP Asymmetries in B Decay*, Nucl. Phys. **B307**, 19 (1988).

[13] A. Einstein, B. Podolsky, and N. Rosen, *Can Quantum-Mechanical Description of Physical Reality be Considered Complete?*, Phys. Rev. **47**, 777 (1935).

[14] A.B. Carter and A.I. Sanda, *CP Nonconservation in Cascade Decays of B Mesons*, Phys. Rev. Lett. **45**, 952 (1980); *CP Violation in B-Meson Decays*, Phys. Rev. D **23**, 1567 (1981). For algebraic details, see also I.I. Bigi and A.I. Sanda, *Notes on the Observability of CP Violations in B Decays*, Nucl. Phys. **B193**, 85 (1981).

[15] See also J. Liu and L. Wolfenstein, *Superweak Contribution to B^0-$\bar{B}^0$ Mixing*, Phys. Lett. **197B**, 536 (1987).